USE OF AN OPTIMISATION METHOD IN BUILDING MACRO MODELS FOR SMALL STRUCTURES IN AIRFRAMES

Ran Xia

Doctor of Philosophy

Department of Electronics
University of York
September 2013

Abstract

Motivated by the demands of determining aircraft electromagnetic compatibility (EMC) performance using computational means, this thesis investigates a method of building small structures into Finite-Difference Time-Domain (FDTD) meshes larger than the structure size. The proposed modelling method is to build the characteristics of the small structure into the FDTD mesh; these are determined using an optimisation method on the fields penetrating the structure, which are obtained by detailed simulations or measurements.

Electric and magnetic polarisabilities are used to characterise the apertures. These polarisabilities are fitted by an optimiser, and a genetic algorithm (GA) is used as the optimisation method in this research program. The equivalent dipole moment to replace the aperture in the FDTD model is calculated from the polarisabilities obtained by the GA. This equivalent model shows good results in terms of both field intensity and phase. When applied on a single square aperture problem, the equivalent model shows field amplitude within 2 dB and phase within 10 degrees from that simulated using an FDTD detailed simulation.

A measurement system including field probes, a 3-D scanning frame, and the absorber box is built to provide validation and source data for the modelling work. A small dipole with a differential amplifier is used to measure the electric field. The measurement accuracy could be improved by further development of the measurement methods, such as encountering diffraction and noise.

A number of tests using both fine-grid simulated and measured field shown the model can produce good results in both fine- and coarse-grid mesh models, in both magnitude and phase.

Table of Contents

Table of Contents i
Table of Figures iv
Acknowledgements x
Declaration xi
List of Publications xi
Chapter 1. Introduction ..... - 1 -
1.1. Project Background ..... - 1 -
1.2. Hypothesis ..... - 3 -
1.3. Project aims ..... - 4 -
1.4. Related Work and Background ..... - 5 -
1.4.1. Macro models of small structures ..... - 5 -
1.4.2. Modelling radiating structures using equivalent source ..... - 5 -
1.5. Principles and Methods Involved ..... - 7 -
1.5.1. Representation of small apertures using dipole moments characterised by polarisabilities ..... - 7 -
1.5.2. The Genetic Algorithm (GA) ..... - 9 -
1.5.3. The Finite-Difference Time-Domain (FDTD) method ..... - 9 -
1.5.4. Surface Equivalence Theorem ..... - 13 -
1.6. Summary ..... - 14 -
Chapter 2. Using optimisation to find a dipole model of a small structure ..... - 15 -
2.1. Introduction ..... - 15 -
2.2. Setup of the MATLAB GA to find the dipole model ..... - 17 -
2.3. Tests and Discussions ..... - 19 -
2.3.1. Validation test using analytically generated field ..... - 19 -
2.3.2. Validation test using measurement data ..... - 22 -
2.3.3. Discussion on GA performance with changing operators ..... - 24 -
2.4. Summary ..... - 28 -
Chapter 3. Modifications to the FDTD update process to implement the equivalent aperture model ..... - 29 -
3.1. The Finite-Difference Time-Domain Method ..... - 29 -
3.2. Modelling macroscopic structures in FDTD meshes ..... - 30 -
3.3. Algorithm introduction ..... - 31 -
3.4. Plane wave excitation in Vulture ..... - 32 -

3.5. Algorithm implementation and validation ..... - 34 -
3.6. Transformation from fine-grid model to coarse-grid model ..... - 38 -
3.6.1. Phase correction method ..... - 41 -
3.6.2. Coordinate change due to mesh size variation ..... - 44 -
3.7. Utilising the dipole model with the frequency-dependent DIGIFILT module….. ..... - 45 -
3.8. Summary ..... - 52 -
Chapter 4. Measurement Devices Development ..... - 53 -
4.1. The absorber box ..... - 53 -
4.2. Near-field probes ..... - 54 -
4.2.1. Small dipole design ..... - 54 -
4.2.2. Small loop design ..... - 61 -
4.3. The 3-D scanner ..... - 64 -
4.4. Measurement results ..... - 65 -
4.5. Summary ..... - 70 -
Chapter 5. Model test cases and limitations ..... - 72 -
5.1. Model application on measured structures ..... - 72 -
5.1.1. Model application on planar scanned near-field above the slot array…. ..... - 72 -
5.1.2. Model application on radiated far-field from slot array in coarse FDTD grid ..... - 74 -
5.2. Model tests on more complex structures ..... - 79 -
5.2.1. Single aperture spanned across two coarse-grid meshes ..... - 79 -
5.2.2. Two small apertures in one coarse-grid mesh ..... - 85 -
5.2.3. A more realistic joint ..... - 91 -
5.3. Model limitations ..... - 97 -
5.3.1. Numerical Dispersion in FDTD ..... - 97 -
5.3.2. Error introduced by non-perfect PML boundaries ..... - 98 -
5.3.3. Frequency-domain limitations ..... - 100 -
5.4. Summary ..... - 102 -
Chapter 6. Conclusions ..... - 103 -
6.1. Optimisation method ..... - 103 -
6.2. Measurement system ..... - 104 -
6.3. FDTD modelling results ..... - 105 -
6.4. Further work ..... - 106 -

Appendix I. Transform analytic expression of radiated field from electric dipole moment from e^{ikr} phasor notation to e^{-jkr} notation ..... - 108 -

Appendix II. Transform analytic expression of radiated field from magnetic dipole moment from from e^{ikr} phasor notation to e^{-jkr} notation ..... - 114 -

Appendix III. Equivalent circuit of an electric dipole using frequency independent lumped elements ..... - 120 -

Appendix IV. MATLAB GA Settings ..... - 123 -

Appendix V. Image theory and approximation of a single source equivalent to the sum of actual and virtual sources..... - 125 -

Appendix VI. List of symbols ..... - 128 -

Appendix VII.List of abbreviations..... - 129 -

References…. ..... - 130 -

Table of Figures

Figure 1.1 Current injection measurement set up, drawn based on, from [1] ..... - 2 -

Figure 1.2 Wing section of a Boeing 737, gaps between skin panels are visible, photographed by Ran Xia ..... - 3 -

Figure 1.3 Representation of penetrating fields by dipole moments reproduced from [16] where E is the incident electric field and P_e is the equivalent electric dipole replacing the aperture..... - 7 -

Figure 1.4 Field components stored for an FDTD mesh, reproduced from [24]..... - 10 -

Figure 1.5 FDTD discretisation of a curved wave front..... - 11 -

Figure 1.6 12×12 mm square aperture in an FDTD model with different mesh sizes to test mesh size convergence ..... - 12 -

Figure 1.7 Frequency domain results of the 12×12mm aperture with different mesh sizes..... - 12 -

Figure 1.8 Surface Equivalence Theorem reproduced from [29]..... - 13 -

Figure 2.1 Geometry of GA test with two electric dipoles separated by 15cm, and an observation plane 30cm from the plane in which the dipoles are placed..... - 20 -

Figure 2.2 Fitness of GA results; the initial value is close to the final result..... - 20 -

Figure 2.3 Radiated electric field at 2GHz from GA fitted dipole moment and theoretically calculated dipole moment ..... - 21 -

Figure 2.4 Radiated electric field at 2GHz from GA fitted dipole moment and theoretically calculated dipole moment ..... - 21 -

Figure 2.5 a) Slot array b) Equivalent magnetic dipoles distribution of the slot array…… ..... - 22 -

Figure 2.6 Side view of the absorber box [43] ..... - 22 -

Figure 2.7 *x*-axis cut of electric field produced by GA and measurement ..... - 23 -

Figure 2.8 y-axis cut of electric field produced by GA and measurement..... - 24 -

Figure 2.9 GA fitness graph of fitting slot array with 6 dipole moments (left) and 30 dipole moments (right)..... - 25 -

Figure 2.10 Result of GA fitting equivalent dipole moment source with increased dipole density..... - 25 -

Figure 2.11 Test of performance of GA with different cost functions..... - 27 -

Figure 3.1 Field structure of an FDTD mesh, reproduced from [24] ..... - 30 -

Figure 3.2 The FDTD aperture model (left), and the aperture replaced by the equivalent source and PEC (right) ..... - 31 -

Figure 3.3 The TFSF method for plane wave support..... - 33 -

Figure 3.4 Reflected plane wave from a PEC sheet without (left) and with (right) the additional plane wave excitation support ..... - 33 -

Figure 3.5 Electric field measured behind a small aperture illuminated by a plane wave - 34 -

Figure 3.6 Aperture simulated in an FDTD model to obtain the penetrated field to be used by the GA..... - 35 -

Figure 3.7 FDTD equivalent model of the aperture, with the aperture replaced by a magnetic dipole moment ..... - 36 -

Figure 3.8 Frequency domain result of aperture equivalent magnetic dipole model - 37 -

Figure 3.9 Spatial domain result of aperture equivalent magnetic dipole model at 3GHz.. ..... - 37 -

Figure 3.10 Coarse-grid simulation of the equivalent aperture model ..... - 38 -

Figure 3.11 Frequency response of fine-grid and coarse grid FDTD simulations and analytic expression ..... - 39 -

Figure 3.12 Frequency domain phase response of fine-grid and coarse-grid FDTD simulations ..... - 39 -

Figure 3.13 Field distribution of fine- and coarse-grid models at 3GHz along z-centre line at 3GHz ..... - 40 -

Figure 3.14 Field distribution of fine- and coarse-grid models at 3GHz along y-centre line at 3GHz ..... - 40 -

Figure 3.15 Phase calibration models in fine-grid (upper) and coarse-grid (lower) . - 42 -

Figure 3.16 Frequency domain phase at reference points ..... - 43 -

Figure 3.17 Calibrated phases of coarse grid and fine-grid models ..... - 43 -

Figure 3.18 Locations of coarse- and fine-grid mesh field components ..... - 44 -

Figure 3.19 Definition of impedance matrix, wave modes and direction of incidence….. ..... - 46 -

Figure 3.20 Fine-grid FDTD model of a 1.5-by1.5 mm square aperture ..... - 49 -

Figure 3.21 Frequency domain response of small aperture by simulation and analytic calculations ..... - 49 -

Figure 3.22 DIGIFILT single aperture simulation output with *r* = 1.97e11 and varying *p* ..... - 51 -

Figure 3.23 DIGIFILT single aperture simulation output with *p* = 1.97e11 and varying *r* ..... - 51 -

Figure 4.1(a) Cross-sectional view of the absorber box, (b) top view of the abosorber box, (c) absorber box with half of the absorber removed, showing the antenna buried in the absorber..... - 54 -

Figure 4.2 Dipole antenna design, photo taken by Ran Xia [48] ..... - 55 -

Figure 4.3 Anechoic chamber set up for testing the dipole antenna ..... - 56 -

Figure 4.4 Phase balance test result of the dipole antenna ..... - 56 -

Figure 4.5 Cross-polar rejection test result of the dipole antenna ..... - 57 -

Figure 4.6 Equivalent circuit of a dipole antenna, reproduced from [49] ..... - 58 -

Figure 4.7 Circuit layout of the electric field probe ..... - 59 -

Figure 4.8 Measured and theoretical AF of the dipole antenna ..... - 60 -

Figure 4.9 Frequency vs Gain characteristics of ADL5562 for 200 Ω differential load. Maximum gain =15.5dB, medium gain = 12dB and Minimum gain = 6dB [50] ..... ……- 60 -

Figure 4.10 Front (left) and back (right) design of the loop antenna ..... - 61 -

Figure 4.11 Loop under test in the anechoic chamber..... - 62 -

Figure 4.12 Phase balance test result of the loop antenna ..... - 62 -

Figure 4.13 Cross-polar rejection test result of the loop antenna ..... - 63 -

Figure 4.14 Measured antenna factor of the loop..... - 63 -

Figure 4.15 Top view of the scanning frame (top-left), scanning frame connected to VNA (top-right) and dipole antenna in measurement driven by the scanning frame (bottom)..... - 65 -

Figure 4.16 Measurement area of the planar measurement above the slot array ..... - 66 -

Figure 4.17 Measured *y*- polarised electric field 17mm above the slot array at 3GHz ..... …..- 66 -

Figure 4.18 Geometry of the slot samples..... - 67 -

Figure 4.19 Measurement results of the centre lines of the samples ..... - 68 -

Figure 4.20 TLM simulation geometry of the slot samples ..... - 69 -

Figure 4.21 Measured and simulated electric field penetrating the slots relative to the excitation fields ..... - 69 -

Figure 5.1 Slot array geometry (left) and dipole moment distribution for the GA search (right) ..... - 73 -

Figure 5.2 FDTD model with equivalent magnetic dipoles to simulate the slot array…… ..... - 73 -

Figure 5.3 GA search result and GA result applied to FDTD equivalent model at 2GHz.. ..... - 74 -

Figure 5.4 Geometries of the FDTD fine-grid (left) and coarse grid (right) models with equivalent dipoles built in ..... - 75 -

Figure 5.5 Field distribution of fine- and coarse-grid equivalent model of the slot array along *z*- centre line at 1 GHz ..... - 75 -

Figure 5.6 Field distribution of fine- and coarse-grid equivalent model of the slot array along *y*- centre line at 1 GHz ..... - 76 -

Figure 5.7 Phase of electric field produced by fine- and coarse-grid equivalent model of the slot array along *z*- centre line at 1 GHz ..... - 76 -

Figure 5.8 Phase of electric field produced by fine- and coarse-grid equivalent model of the slot array along *y*- centre line at 1 GHz ..... - 77 -

Figure 5.9 Electric field intensity in the frequency domain, produced by fine-grid and coarse-grid equivalent models of the slot array ..... - 78 -

Figure 5.10 Electric field phase in the frequency domain, produced by fine-grid and coarse-grid equivalent models of the slot array ..... - 78 -

Figure 5.11 Mesh distribution on testing the model with aperture across two coarse meshes ..... - 79 -

Figure 5.12 Near-field distribution of the aperture simulated by FDTD, calculated using equivalent dipole moment fitted by GA, and simulated with the equivalent dipole moment in FDTD ..... - 80 -

Figure 5.13 *y*-centre line electric field distribution of fine- and coarse-grid models at 2GHz ..... - 81 -

Figure 5.14 *z*-centre line electric field distribution of fine- and coarse-models at 2GHz… ..... - 82 -

Figure 5.15 Electric field vs frequency at centre point of output plane ..... - 82 -

Figure 5.16 *z*-centre line phase distribution of the electric field at 2GHz..... - 83 -

Figure 5.17 *y*-centre line phase distribution of the electric field at 2GHz..... - 84 -

Figure 5.18 Electric field phase vs frequency at centre point of output plane ..... - 84 -

Figure 5.19 Mesh distribution on testing the model with two apertures located in one coarse mesh ..... - 85 -

Figure 5.20 Near-field distribution of the two square apertures simulated by the FDTD method, calculated using equivalent dipole moment fitted by the GA, and simulated with the equivalent dipole moment in the FDTD method ..... - 86 -

Figure 5.21 *y*-centre line electric field distribution of fine- and coarse-models at 1GHz ....- 87 -

Figure 5.22 *z*-centre line electric field distribution of fine- and coarse-models at 1GHz ..... …- 88 -

Figure 5.23 Electric field vs frequency at centre point of output plane ..... - 88 -

Figure 5.24 *y*-centre line phase distribution of the electric field at 1GHz..... - 89 -

Figure 5.25 *z*-centre line phase distribution of the electric field at 1GHz..... - 90 -

Figure 5.26 Electric field phase vs frequency at centre point of output plane ..... - 90 -

Figure 5.27 Geometry of a complex slot ..... - 91 -

Figure 5.28 3-D plot of the penetrated field 45mm from the structure at 2GHz..... - 92 -

Figure 5.29 Radiated field of the GA fitted dipoles in both analytic calculation and FDTD equivalent model, compared to that of the FDTD aperture simulation .. - 93 -

Figure 5.30 Frequency domain result of the equivalent dipole in 0.5mm and 1mm mesh, taken at the centre point of the observation plane ..... - 94 -

Figure 5.31 *z*-centre line far-field distribution of fine- and coarse-mesh models at 2GHz ..... - 94 -

Figure 5.32 *y*-centre line far-field distribution of fine- and coarse-mesh models at 2GHz ..... - 95 -

Figure 5.33 Frequency domain phase results of fine- and coarse-grid simulation.... - 96 -

Figure 5.34 *z*-centre line far-field phase distribution of fine- and coarse-mesh models at 2GHz ..... - 96 -

Figure 5.35 *y*-centre line far-field phase distribution of fine- and coarse-mesh models at 2GHz ..... - 97 -

Figure 5.36 Single aperture model for observation of phase of the penetrated field…….. ..... - 98 -

Figure 5.37 Phase of field penetrating the square aperture and radiated by equivalent dipole moment ..... - 99 -

Figure 5.38 Effect on the phase of increasing the electrical distance between the aperture and the measurement surface ..... - 99 -

Figure 5.39 Frequency domain responses of aperture simulated in FDTD model and represented by an equivalent dipole ..... - 101 -

Figure 5.40 Comparison of frequency-domain results of the GA fitted dipole moments from measured field above the slot array on 1mm and 25mm grid models..... - 102 -

Figure I.1 Frequency response of the elementary dipole ..... - 112 -

Figure I.2 Results of radiated field from an elementary dipole at 2GHz ..... - 112 -

Figure I.3 Results of radiated field from an elementary dipole at 2GHz ..... - 113 -

Figure II.1 Frequency response of the elementary magnetic dipole..... - 117 -

Figure II.2 Comparison of radiated field from 0 to 0.5m at 1GHz ..... - 117 -

Figure II.3 Comparison of radiated field from 0 to 0.5m at 2GHz ..... - 118 -

Figure II.4Comparison of radiated field from 0 to 0.5m at 10GHz ..... - 118 -

Figure III.1 Equivalent circuit of an electrically small dipole, reproduced from [2]…….. ..... - 120 -

Figure V.1 Image theory, the reflected wave at the observation points can be treated as coming from a virtual source which is an image of the actual source ..... - 125 -

Figure V.2 Positions of dipoles in the Image Theory verification test..... - 126 -

Figure V.3 Frequency domain results of the verification test of Image Theory approximation ..... - 126 -

Acknowledgements

I would like to thank Dr John Dawson and Dr Ian Flintoft for the help, discussions and advice that they gave throughout the supervision of the project. In addition, the hard work of the Technical Supporting Service (TSS) in the department in fabricating probes, and building and maintaining the scanning frame is very much appreciated.

This work is part-funded by the EU 7th Framework project HIRF-SE. By taking part of this project and working with the Applied Electromagnetics Group in the Electronics Department, I have gained valuable research experiences and skills. I'm very grateful to what this project has offered me.

Also, thanks go to my close friends who supported and encouraged me during the project, including Dr Gregory Melia, Mr Zixin Chen, Dr Yaoan Wu, Dr Yi Qu, Ms Chang Sun and Ms Lin Miao.

Finally, this project could not be done without my family, who have always supported me in any way they possibly can.

Declaration

To the best knowledge of the author, all the work presented in this thesis claimed as original is so. Any research that is not original is clearly stated and referenced, which includes Figure 1.1, Figure 1.3, Figure 1.4, and Figure 3.1. In addition, the FDTD simulation tool 'Vulture', the TLM simulation tool 'Hawk', the absorber box, the field probes and the 3-D scanning frame are developed by the Physical Layer Research Group in the department.

List of Publications

- Xia, R. Dawson, J. Flintoft, I. Marvin, A. Porter, S. & Marschke, I. *Building electromagnetic macro models for small structures on aircraft: Characterising and modelling joints, seams, and apertures*, EMC Europe 2011 York, 2011, 575-580

- Xia, R. Dawson, J. Flintoft, I. Marvin, A. & Porter, S. *Use of a Genetic Algorithm in modelling small structures in airframes: Characterising and modelling joints, seams, and apertures*, Electromagnetic Compatibility (EMC EUROPE), 2012 International Symposium on, 2012, 1-5

- Flintoft, I.D. Dawson, J. F. Xia, R. Porter, S.J. & Marvin, A.C. *Simulation of materials and joints in FDTD using digital filter macro-models.* EuroEM 2012. 2012.

Chapter 1. Introduction

This thesis introduces a novel modelling method to build macro-models of small structures in airframes into numerical EM solvers. This research of modelling small structures such as panel gaps and small holes is part of the EU HIRF-SE project. The proposed method is to obtain an equivalent source, which is formed by an array of dipole moments, from a measured or simulated field by using an optimisation method. The model is built for full-scale aircraft simulation where the mesh size used is much larger than the size of the small structure; therefore the model is a macro model, or sub-cellular model. In this chapter, the HIRF-SE project is firstly described with its background and objectives, and then the modelling work of this thesis is introduced, followed by the descriptions of methods and principles involved. The second chapter introduces the optimisation method used to search for the parameters of the equivalent models of the small structures. A genetic algorithm (GA) is chosen as the optimisation method for this application; the parameters of the GA are derived using some simplified analytic expressions of calculating radiated fields from dipoles. The tuning of those GA parameters is then discussed. Chapter 3 describes the implementation of the equivalent model into an FDTD simulation package. The FDTD code 'Vulture' is developed by the Physical Layer Research Group of the Electronics Department at the University of York. Results of some simple models are then presented as validation tests. Chapter 4 describes the hardware development, including specialist field probes and a 3-D scanning frame built for planar field scans. Chapter 5 presents results of the integration of the model components introduced in the first four chapters, along with discussion of the model applications and limitations by comparing results produced by the equivalent model and direct aperture simulation from a number of test cases. The last chapter gives a conclusion and discusses further development of the model in the future.

1.1. Project Background

An aircraft is required to be certified for electromagnetic compatibility (EMC) before entering service. Due to the ever-increasing number of electronic instruments installed in aircraft, and the ever-increasing complexity of the surrounding EM environment, EMC is now a safety-critical issue for aircraft and the aircraft EMC environment is strictly controlled. The area of concern for aircraft EMC has grown gradually from low-power interference between items of on-board equipment to the effect of the external High-Intensity Radiated Field (HIRF) environment on the aircraft and the list

of aspects that are covered by EMC testing standards has become wider with time. Carter [1][2] describes this trend and gives examples of aircraft EMC testing methods. For example, in bulk current injection (BCI), a high level current is injected directly into the aircraft skin to simulate a lightning strike, while the induced current in the on board equipment is monitored. Later, tests in mode-stirred chambers were introduced, as illuminations from broadband antennas in anechoic environments could no longer meet the 6800V/m field amplitudes required by the standards. A mode-stirred chamber is a test chamber with highly reflective walls and stirrers. In such a test environment, equal energy arrives at the test object from all directions and polarisabilities. Mode-stirred chambers are often used for the measurement of objects' EM absorption characteristics [3][4].

A weakness of both the current injection and the chamber testing methods is that they require both a complex test set-up and a test chamber of aircraft size, as shown in Figure 1.1. Furthermore, these tests are carried out on prototype aircraft, after structural design has been completed. In the case of test failure, any remediation is expensive in terms of both time and money. In addition, the complex structure of an aircraft makes it difficult to carry out measurement of some parts in the airframe.

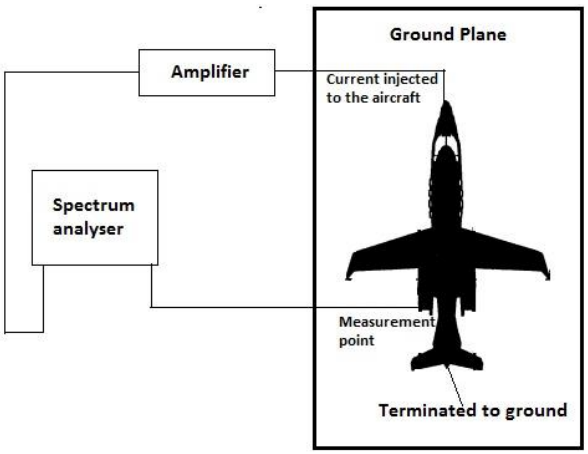

Figure 1.1 Current injection measurement set up, drawn based on, from [1]

For the above reasons, there is an increasing demand to predict aircraft EMC performance by computational means at the design stage. There has been some work in this field, including the certification of the FAR25 aircraft against electromagnetic interference (EMI) using both measurement and simulation data; and the certification of the C27 aircraft against lightning strike [5].

The HIRF-SE project [6] is an EU Framework 7 project that aims to provide an electromagnetic modelling framework for aircraft EMC prediction for design and

certification. The work described by this thesis forms part of the HIRF-SE project, which is building macro-models for small structures of the aircraft, such as mechanical joints and small holes. These structures exist throughout the airframe, such as compartment doors, equipment ventilation holes and panel joints as shown in Figure 1.2. All of these structures could provide potential paths for unwanted EM radiation to reach and interfere with on-board electronic instruments.

Figure 1.2 Wing section of a Boeing 737, gaps between skin panels are visible, photographed by Ran Xia

A panel joint on an aircraft may be bounded on one or both sides by composite materials which have conductivities that are not as easily modelled as those of metals. In addition, a joint may have a complex structure with flanges, fasteners and fillers, and the geometry and electrical connectivity of a joint is not always well defined at high frequencies. Normally, to model a structure accurately using the Finite Difference Time Domain (FDTD) method requires a number of mesh elements across the structure's smallest details. Such a detailed model cannot be directly incorporated into a full-scale aircraft simulation without excessive computational requirements. Because the sizes of these small structures are in the order of millimetres or even smaller, full-wave modelling of an aircraft using a mesh size would be prohibitively computationally expensive due to the large amount of memory required. On the other hand, full-scale simulations of aircraft use a mesh size in the order of centimetres. In contrast, to the size of the structures to be modelled in this project, which is in the scale of millimetres, the models built in a mesh that is much larger than the object being simulated; such a model is called a macro model, or sub-cellular model.

1.2. Hypothesis

Equivalent sources can be used to build sub-cellular models in FDTD simulations, which reconstruct the field penetrating the small gaps illuminated by EM fields. Properly designed and tuned optimisation methods are capable of finding these

equivalent sources accurately and efficiently. The model built with this method can produce frequency and spatial domain results more accurately than direct FDTD simulation with a mesh size much larger than the structure being modelled.

The hypothesis is tested by applying the new modelling method on some simple structures such as a small square aperture. The optimisation method is expected to find an equivalent source to represent such simple structures within minutes. The radiated fields reproduced by the obtained sources are expected to be within 2 dB difference compared to that simulated directly in a detailed FDTD model.

1.3. Project aims

Here we aim to use the measured or predicted coupling response of a complex slot or joint, with fasteners and other detailed structures, to define a macro-model based on frequency-dependent boundary conditions.

As stated in the hypothesis, the proposed model, built to be used as part of a coarse-grid simulation, will be able to offer improved spatial and frequency field details. The proposed method is to use an optimisation method, applied on data from a fine-grid simulation and/or the field from measurements taken near the joint, to determine an equivalent array of electric and magnetic dipole moments that reproduces the penetrating field.

For simplicity, sometimes a joint is modelled as an infinitely long slot with uniform width. However, the widths of real structures on airframes will not be of a uniform width, and some complex structures, such as flanges and fasteners may exist. These features may result in complex radiation patterns that are difficult to represent using a macro model. In addition, the joint in the macro model may not be a symmetrical problem: the joint might not lie in the centre line of the coarse mesh, or it might be terminated in the middle of the mesh. The magnitudes of the dipole moments that represent the radiating slots are approximated as constants across the frequencies when the apertures are electrically small. Whether frequency-dependent characteristics are needed to improve the upper frequency that the model is valid is going to be investigated.

There have been models developed that are related to the aim of this research program, as will be shown in the next section, such as the Holland-Gilbert model for sub-cellular modelling in FDTD meshes [7] and the shielding effectiveness modelling of a slot by representing the slot with equivalent sources. The novel contribution of this

modelling work is to reproduce the absolute radiated field strength from the aperture by using equivalent sources, rather than modelling the shielding effectiveness.

1.4. Related Work and Background

1.4.1. Macro models of small structures

A joint can be considered as an array of slots separated by conducting fasteners. The sub-cellular slot model in the FDTD method has been investigated using various methods. The Gilbert-Holland model, [7][8] approximates the infinite narrow slot as an equivalent capacitance. The slot is modelled by varying the permittivity and permeability of the mesh in the FDTD update equation. It is widely used and considered to be robust and accurate. This model is capable of reasonable accuracy with a slot of width one-fifteenth of the FDTD mesh size. Taflove et al [9] have extended the equivalent capacitance approach so it can model the slot when the field is resonating due to the slot thickness and air breakdown of high-power microwave radiation. Riley and Turner [9] report that the averaging factor in the Gilbert-Holland model causes errors as the width of the aperture decreases. They introduce a method that uses a hybrid Method of Moments (MoM) and FDTD algorithm. By adapting 'half width' transient integral equations to the FDTD update equations, this method has demonstrated better accuracy than the Gilbert-Holland model.

The Gilbert-Holland model is a well-developed modelling method for modelling small apertures in the FDTD method. It uses a line integral to obtain the equivalent capacitance, where the measured field at the required locations is sometimes unavailable in the application of this research program due to the complexity of the airframe. Alternatively, using an optimisation method can obtain the equivalent source from fields measured on an arbitrary surface, providing the measurement covers most of the area that the field intensity is concentrated. In addition, computational cost is expected to be lower if an optimiser is used properly, compared to that of deriving the equivalent sources analytically.

1.4.2. Modelling radiating structures using equivalent source

There has been extensive research on the modelling of complex structures using equivalent sources. This method has the advantage of modelling the structure without knowing the detailed geometry. It thus saves time spent on drawing the detailed structure in CAD, along with computational effort in computing the source details.

Meanwhile, with proper optimisation of the equivalent sources, it can achieve good accuracy.

In most publications, arrays of infinitesimal electric and magnetic dipoles or current distributions are used as the equivalent sources, since the dipole is one of the simplest radiating sources and its current distribution can be solved efficiently using the Fourier Transform. One application close to the objective of this thesis is using equivalent sources to characterise printed circuit boards (PCBs). Petre [12] demonstrates modelling of a PCB using an equivalent current distribution using a near-field scan. The near-field and far-field can then be solved using field transformation. The measurement needs to be taken outside the reactive near-field region to avoid the rapid variation of the field to maintain the accuracy of the field transformation. Laurin [13] improved the formation of the equivalent sources so that reactive near-field scanning can be used for this application. In addition, it is demonstrated this method can be used for characterising complex structures such as an array of patch antennas. This field transformation technique requires accurate measurement, as noise in the measured data may corrupt the transformation. Therefore, diffraction, interference and disturbance from the outside environment and the measurement system need to be considered and removed as much as possible.

Tong [14][15] demonstrates a near-field scanning system includes data processing and equivalent source characterisation, in which a PCB is characterised as an array of magnetic dipoles. Instead of using a Fourier Transform to analytically calculate the current distribution, a genetic algorithm is used to obtain the dipole moment. Then, the radiated fields from the equivalent dipole array are then solved using MoM; good agreement is achieved on measurement carried out on planes parallel and normal to the antenna.

In the PCB modelling method presented above, the far-fields are calculated using field-transformation or equivalent surface current distribution. These methods require accurate near-field measurements. The scanning system described by Tong [14][15] includes near-field probe correction and noise-reduction method. The modelling method proposed in this thesis does not require the near-field measured as accurately as is required for those PCB modelling work, but still produces results of equivalent accuracy. Furthermore, the radiated fields from the equivalent dipoles are calculated using simple formulations instead of by solving the equivalent current distributions. In other words, the modelling method makes less stringent requirements on the

measurement accuracy and computational load, but still can achieve accurate results compared to the existing modelling methods.

1.5. Principles and Methods Involved

1.5.1. Representation of small apertures using dipole moments characterised by polarisabilities

A dipole is one of the simplest radiating sources in electromagnetics. It is an omni-directional radiating source that can be characterised as a current flowing on a thin wire. The dipole moment, in this research program, is used to approximate the radiating structure as a number of infinitely small electric and magnetic dipoles [16].

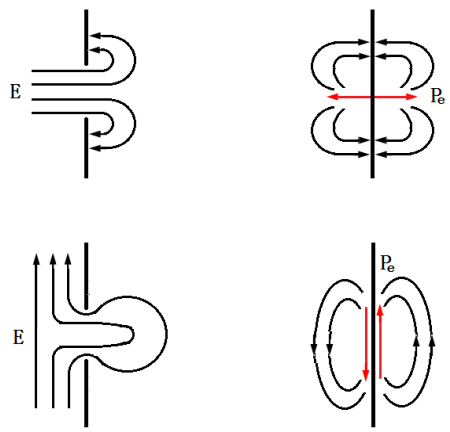

Figure 1.3 Representation of penetrating fields by dipole moments reproduced from [16] where *E* is the incident electric field and P_e is the equivalent electric dipole replacing the aperture

Figure 1.3 shows the approximation of an electric field penetrating a small aperture to that radiated by an electric dipole, where the radiated field from a dipole in free space can be calculated using the expressions [17]:

For electric dipole moments:

$$\boldsymbol{E} = \frac{1}{4\pi\varepsilon_0}\left\{k^2(\hat{\mathbf{r}}\times\mathbf{p})\times\hat{\mathbf{r}}\frac{e^{-jkr}}{r} + \left[3\hat{\mathbf{r}}(\hat{\mathbf{r}}\cdot\mathbf{p})-\mathbf{p}\right]\left(\frac{1}{r^3}+\frac{jk}{r^2}\right)e^{-jkr}\right\} \qquad \textbf{(1.1)}$$

$$\boldsymbol{H} = \frac{ck^2}{4\pi}\left((\hat{\mathbf{r}}\times\mathbf{p})\right)\frac{e^{-jkr}}{r}\left(1+\frac{1}{jkr}\right) \qquad \textbf{(1.2)}$$

For magnetic dipole moments:

$$\boldsymbol{H} = \frac{1}{4\pi}\left\{k^2(\hat{\mathbf{r}}\times\mathbf{m})\times\hat{\mathbf{r}}\frac{e^{-jkr}}{r} + \left[3\hat{\mathbf{r}}(\hat{\mathbf{r}}\cdot\mathbf{m})-\mathbf{m}\right]\left(\frac{1}{r^3}+\frac{jk}{r^2}\right)e^{-jkr}\right\} \qquad \textbf{(1.3)}$$

$$\boldsymbol{E} = \frac{-\eta_0}{4\pi} k^2 \left((\hat{\mathbf{r}} \times \mathbf{m}) \right) \frac{e^{-jkr}}{r} \left(1 + \frac{1}{jkr} \right) \quad \textbf{(1.4)}$$

Where $\boldsymbol{p}$ is the electric dipole moment vector, $\boldsymbol{m}$ is the magnetic dipole moment vector, k is the wave number, r is the distance between the dipole moment and the observation point, $\hat{\boldsymbol{r}}$ is the unit vector of the vector point from the dipole moment to the observation point, η_0 is the impedance of free space, c is the speed of light, $\boldsymbol{E}$ is the radiated electric field and $\boldsymbol{H}$ is the radiated magnetic field.

The dipole moment is represented by the size of the dipole and the equivalent electric or magnetic current flowing on the dipole:

$$\boldsymbol{p} = \frac{\boldsymbol{I_e \Delta l}}{\boldsymbol{j\omega}} \quad \textbf{(1.5)}$$

$$\boldsymbol{m} = \frac{\boldsymbol{I_m \Delta l}}{\boldsymbol{j\omega}} \quad \textbf{(1.6)}$$

Where $\boldsymbol{I_e}$ and $\boldsymbol{I_m}$ stand for electric and magnetic current vectors respectively, Δl is the size of the dipole, ω is the angular frequency of the current and μ_0 is the permittivity of free space. In this particular problem of fields penetrating small apertures, the calculation of equivalent currents flowing on the aperture surface is not trivial. Alternatively, the equivalent dipole moment can be characterised using the incident field to the aperture and the aperture polarisability, which represents the amount of field transmitted through the aperture [18].

$$\boldsymbol{p} = \boldsymbol{E_{sc}} \boldsymbol{\alpha_e} \quad \textbf{(1.7)}$$

$$\boldsymbol{m} = \boldsymbol{H_{sc}} \boldsymbol{\alpha_m} \quad \textbf{(1.8)}$$

Where $\boldsymbol{E_{sc}}$ and $\boldsymbol{H_{sc}}$ are short-circuited electric and magnetic fields, which are defined by [18] as the fields measured at the position of the aperture when it is closed. Since the incident field is reflected by the short-circuited aperture, the short-circuited field is twice the intensity of the incident field illuminating the aperture. α_e and α_m are electric and magnetic polarisabilities. Polarisability is a function of aperture shape, size and orientation relative to the incident wave. Measurements of the polarisabilities of some small apertures are carried out by [19], which support the approximation that the polarisability of an aperture is independent of frequency, providing the aperture is small compared to the wavelength of the incoming field. This approximation simplifies the modelling of electrically small apertures, and is employed throughout this research program. On the other hand, analytic expressions of polarisabilities of apertures with different shapes and orientations are given by McDonald [20][21][22]. They provide means of calculating the apertures' polariabilities analytically. In addition, these expressions analytically proved the approximation which [19] supported experimentally.

In summary, an electrically small aperture can be replaced by electric and magnetic dipole moments. As stated, a dipole is a simple radiation source. It is also simple to implement a dipole into computational models. Therefore replacing radiating apertures by dipole moments are chosen as the modelling method in this research program.

1.5.2. The Genetic Algorithm (GA)

First introduced by John Holland in the 1970s, the GA is an optimising method that uses the natural law of evolution, 'survival of the fittest', to find the best answer to a problem. By analogy to biological evolution, a 'population' is initially generated randomly within pre-defined search bounds, then a number of genetic operations are performed on the population to generate the next generation. This process is repeated until a stop criterion is met. The GA is widely used as an optimisation method. It is well known for its efficiency in converging towards the bottom of the error landscape, the robustness for not being trapped in local minima. The GA is also easy to use since it works on a cost function, rather than the analytic derivation of the problem. This simplifies the modelling process as the details of the structure can be left unknown. In addition, solving only the cost function lowers the computational requirement, compared to solving the complex problem analytically. Details of the development, application and set-up of the GA in this research program are discussed in Chapter 2.

1.5.3. The Finite-Difference Time-Domain (FDTD) method

1.5.3.1. FDTD method for electromagnetic simulations

Originally proposed by Yee [23], the FDTD method has been widely used in numerical computational electromagnetics. It is the simulation method employed by this research program to provide computational field results for modelling and validations. In the FDTD method, the time domain is discretised into time steps, and the fields are calculated and updated at each time step. In the spatial domain, the FDTD method requires the problem space to be divided into small meshes as single units of the field updating process. The algorithm then effectively solves Maxwell's Equations and updates the field components in each mesh after every time step.

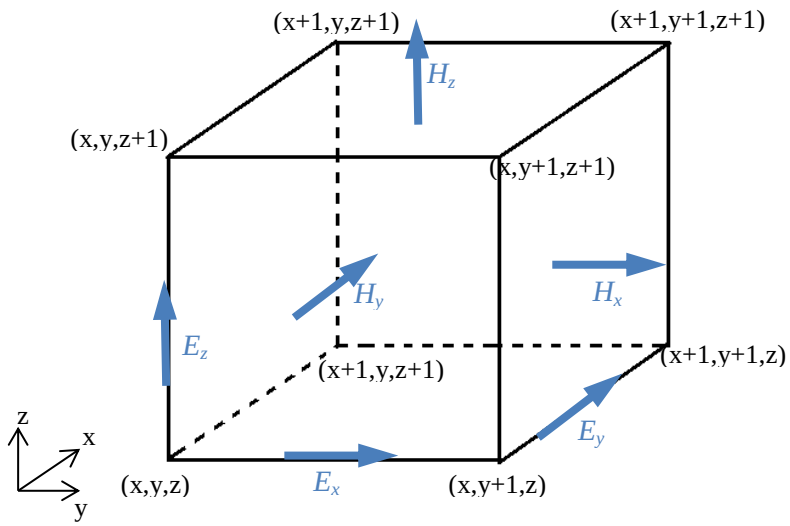

Figure 1.4 Field components stored for an FDTD mesh, reproduced from [24]

As shown in Figure 1.4, 6 field components are stored in each mesh [25], where *x*, *y* and *z* give the location of the mesh along the axes in terms of mesh number, ***E*** is the electric field and ***H*** is the magnetic field. To clarify the definitions, a 'mesh' is defined as a single block in the problem space. As seen in Figure 1.4, it defines the spatial locations that the fields are calculated. The FDTD 'grid' is defined as the problem space that is formed by a number of 'meshes'. The rest of the thesis will employ the same definitions above. For example, 'a fine mesh' means a mesh with a small mesh size, 'fine-grid' means the problem space is discretised with fine meshes.

The discretisation of the problem space causes a potential problem called 'numerical dispersion', which is introduced in detail in the next section. Due to numerical dispersion, an FDTD mesh should not be larger than 1/10 of the shortest wavelength in the simulation. At the same time, the meshes should be distributed with enough spatial resolution across the structure in the model. Both conditions must be satisfied when choosing mesh size [26][27]. Moreover, since the FDTD method works in the time domain, a Fourier transform is required before the results are processed in the frequency domain. The finer the frequency resolution required, the more time steps will be required to run the model until it converges.

1.5.3.2. Numerical dispersion in the FDTD method

There is a common source of error in the FDTD algorithm known as 'numerical dispersion'. As it is named, this dispersion effect does not exist in the physical world, but is induced by the discretisation of space and time in the FDTD method. The discretisation in the time domain results in a variation of the group velocity of the propagating wave in FDTD, which can be overcome by increasing the number of

sampling points across the wavelength being simulated. For example, it has been mentioned before that it is generally recognised that a mesh size no larger than 1/10 of the wavelength is required in order to produce results at a certain frequency and the accuracy increases by reducing the mesh size. On the other hand, Figure 1.5 shows that, due to the spatial discretisation, the FDTD grid cannot follow a curved wave front accurately without a very fine grid for the model. The numerical dispersion can be reduced but not eliminated; therefore it always has to be accounted as an error source in FDTD simulations. [28]

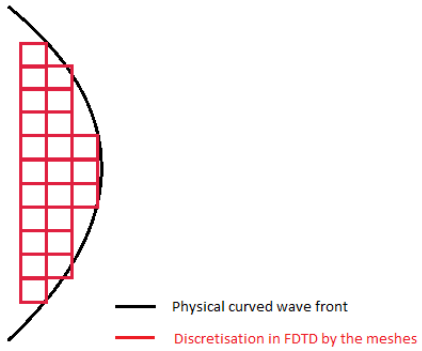

Figure 1.5 FDTD discretisation of a curved wave front

Secondly, as mentioned in Section 1.5.3, to accurately simulate a structure in an FDTD model, a number of meshes are required across the structure, and the accuracy increases with the number of meshes. A simple model of a square aperture can be used to illustrate this effect. A 12 × 12 mm square aperture is simulated in FDTD models using different mesh sizes. The frequency domain result is observed at a point 60 mm from the aperture plane. The simulation geometry and results are shown in Figure 1.6 and Figure 1.7.

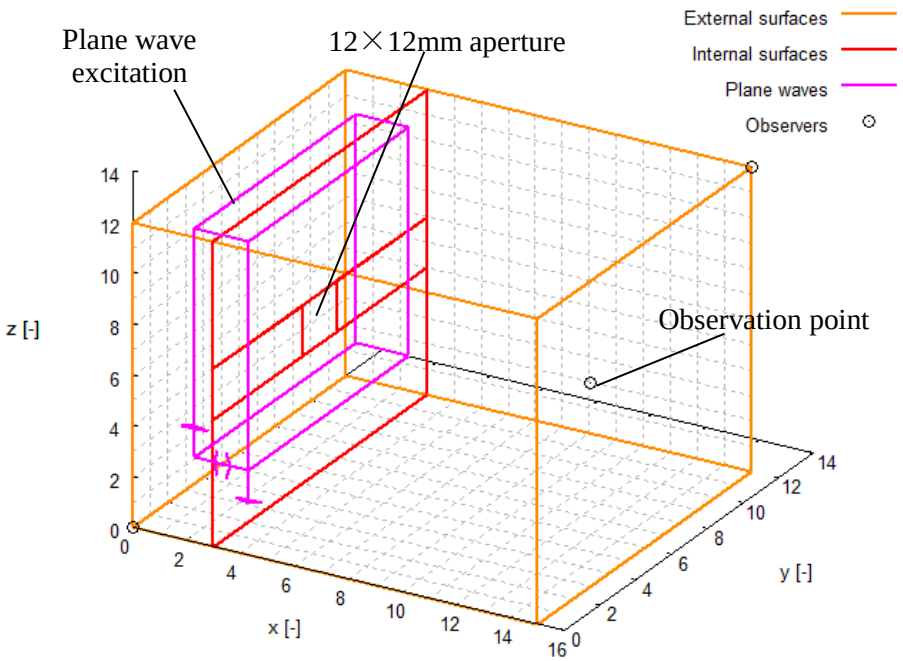

Figure 1.6 12×12 mm square aperture in an FDTD model with different mesh sizes to test mesh size convergence

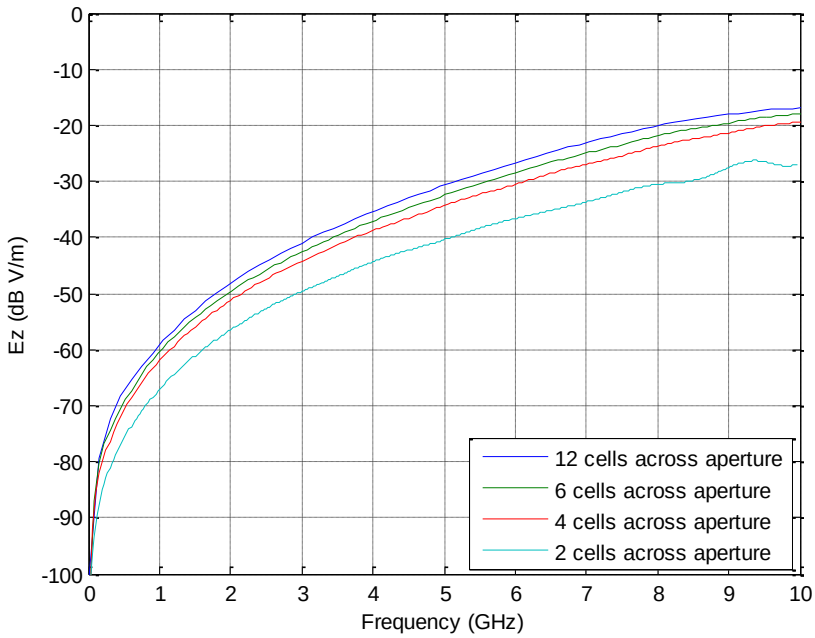

Figure 1.7 Frequency domain results of the 12×12mm aperture with different mesh sizes

It is clearly seen that as the number of meshes across the aperture increases, the results converge towards that with the highest mesh density across the aperture. The error caused by insufficient FDTD meshes across the structure can be as large as 10dB V/m. Care needs to be taken when building FDTD models to make sure the mesh size satisfies the smallest details of the structures being modelled.

1.5.4. Surface Equivalence Theorem

Huygens's principle states that "each point on a primary wave-front can be considered to be a new source of a secondary spherical wave and that a secondary wave-front can be constructed as the envelope of these secondary spherical waves." [29] The Surface Equivalence Theorem, which was introduced by Schelkunoff, is a more rigorous extension of Huygens's Principle, and is based on the uniqueness theorem. [29] In simple words, by using the surface equivalence theorem, a radiating source or structure in the problem is replaced by currents flowing on an imaginary surface, which radiates in the same way as the actual source.

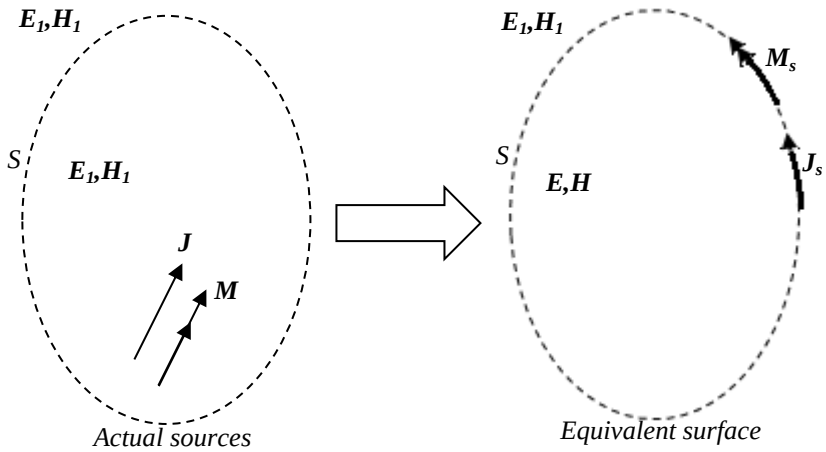

Figure 1.8 Surface Equivalence Theorem reproduced from [29]

As shown in Figure 1.8, the left part shows the field radiated by the actual source. $\boldsymbol{J}$ and $\boldsymbol{M}$ are the electric and magnetic currents of the radiating source, $\boldsymbol{E_1}$ and $\boldsymbol{H_1}$ are the radiated fields from the actual sources and S is the surface over which the equivalent source will be calculated. On the right hand side of Figure 1.8, the actual radiating source is replaced by the surface currents $\boldsymbol{J_s}$ and $\boldsymbol{M_s}$ flowing on S. The equivalent source still radiates the same fields as $\boldsymbol{E_1}$ and $\boldsymbol{H_1}$ outside of S, while that inside S is $\boldsymbol{E}$ and $\boldsymbol{H}$, which are different from $\boldsymbol{E_1}$ and $\boldsymbol{H_1}$. First, a closed surface is chosen to enclose the original source. Then a current density is to be placed on the closed surface in order to produce the same radiated field outside the equivalent surface as was produced by the original source. Since the original source no longer exists, according to the uniqueness theorem, the radiated field is uniquely defined by the tangential electromagnetic field over the surface. There are four situations that can be considered, subject to the problem being treated.

1. $\boldsymbol{J_s}$ and $\boldsymbol{M_s}$ over S, assuming the $\boldsymbol{E}$ and $\boldsymbol{H}$ fields enclosed by S are not zero

2. $\boldsymbol{J_s}$ and $\boldsymbol{M_s}$ over S, assuming the $\boldsymbol{E}$ and $\boldsymbol{H}$ fields enclosed by S are zero

3. $\boldsymbol{M_s}$ over S only, assuming a perfect electric conductor is enclosed by S ($\boldsymbol{J_s}$=0)

4. $\boldsymbol{J_s}$ over S only, assuming a perfect magnetic conductor is enclosed by S ($\boldsymbol{M_s}$=0)

The choice of the equivalent surface is important as in order to make the problem solvable, it is important to make the current densities on the surface known, or those current densities can be approximated. In addition, only the currents flowing on the surface are required for the equivalent source. In other words, the transverse components are sufficient in obtaining the equivalent source. Therefore the nomal components are not needed [29].

According to the equivalent surface theory, the field produced at one point in space can be derived by integrating the field produced by each element on the discrete surface. The model in our case is built in FDTD grids, where the simulation space is discretised by the FDTD meshes. In other words, if the equivalent sources to represent the small structures are built with infinitesimal dipoles, the array theory can be applied here and the radiated field is an integration of the fields radiated by each of the dipoles.

1.6. Summary

This research program aims to build FDTD macro models of electrically small structures in airframes. The proposed modelling method is to obtain equivalent sources of the apertures by optimisation means. A GA is selected as the optimisation algorithm and the equivalent sources fitted by the GA are formed by arrays of dipole moments. The configuration of the GA, implementation of the equivalent dipole moments and development of a measurement system for planar field scanning are described in the following chapters.

Chapter 2. Using optimisation to find a dipole model of a small structure

2.1. Introduction

This chapter describes the method of determining the equivalent sources that represent the electrically small apertures. As introduced in Chapter 1, the equivalent sources are formed by a number of dipole moments. These equivalent sources are obtained by the means of optimisation, and in our case a GA is employed as the optimisation method. First, an overview of the GA is given by describing its principle and discussing a number of modifications. Next, the setup of the GA for searching the equivalent dipole moments in our model is shown. The GA is then tested using both measured and analytically derived electric fields emitted by radiating structures. The test result is then presented, followed by the discussion of some attempts to improve the GA's performance.

The GA is a method of optimisation that uses evolutionary principles. By adopting the law of natural evolution, 'survival of the fittest', it searches for an optimum solution to a problem in a given domain. The GA starts the search by creating an initial population, with parameters chosen at random, within the search boundaries. The algorithm then evaluates the individuals in the population and performs genetic operations on the population to produce the next generation. The three main operations of a GA are selection, cross-over and mutation. Selection is to keep the individuals of best fitness to create the next generation. Cross-over is to exchange design variables between individuals selected for the next generation, and mutation is to generate individuals with new design variables by introducing random changes. The individuals are evaluated using their 'fitness'. In this research program, 'fitness' is defined as the output of the cost function with the individual as the input. All the cost functions are defined to have 0 as the optimum output. This process is repeated until a stop criterion is reached. Usually a GA is stopped when the new generation does not improve the fitness or a maximum number of generations is reached [30].

The GA is widely employed in many areas as it is considered to be an effective optimisation tool and simple to use. It improves the fitness of the population by evaluating a cost function, which is sometimes faster than solving the complex problem analytically. Therefore, the required computational effort is reduced. Rather than

optimising a single candidate answer, the GA searches for the optimal solution by working on a population of candidate answers simultaneously. The diversity given by multiple candidates increases the probability of reaching the global optimum. The exchange of high fitness variables between individuals accelerates the optimisation process. It is chosen as the optimisation algorithm for this research program for its simplicity and convergence efficiency. However, there are a few drawbacks associated with this algorithm, which are discussed below.

Although less computational effort is required compared to analytically solving a complex problem, the searching process of the GA may be time-consuming. In other words, the GA is considered to be efficient in finding the area where the answer exists but it is difficult for the GA to find the exact solution. Usually, the slope of the cost landscape becomes shallower as the GA approaches the bottom; hence the guidance of the cost function becomes weaker. To improve the performance of the optimisation, the GA is sometimes modified to have variable operating factors, or is hybridised with other algorithms, such as the steepest descent method [31].

There are several kinds of modifications to the standard GA operators. Some random factors in the GA operations become guided after these modifications, and the convergence towards the answer is accelerated. Crevecoeur et al [32] present a two-level GA which uses two models at different stages of the computation. At the beginning a coarse grid model, which is faster to run, is used to initially allow the GA to converge to the region where the answer exists. Then a finer grid model, which is slower to run but better in terms of accuracy, replaces the coarse grid model to improve the accuracy further. This modification improves the accuracy of the result with the cost of added complexity due to the need for a mapping algorithm between the coarse- and fine-grids. Instead of using different models, Chen et al [33] describe a method of variable mutation rate, which is relatively easier to implement than the method introduced in [32]. The mutation rate is higher at the beginning of the search to give the population higher diversity, and then decreases as the GA runs to avoid destroying good genes in chromosomes. On the other hand, Dupré [34] suggests a variable mutation rate assigned to each of the individuals, where the individuals that fit better have lower mutation rates. The aim of this method is the same as [33]: to maintain the diversity, while protecting the individuals of high fitness. A method of varying another operator, which is the search boundary, is introduced by Li et al [35]. In this method, the search boundary is dynamically adjusted using the fitness of the cost function.

In this research program, a GA is employed to search for an array of dipole moments, which are then used to model a complex structure. The modelling of an EM field penetrating electrically small apertures has been researched extensively. A number of papers refer to Bethe [36], which gives analytic derivations of EM field penetration for electrically small apertures of a number of shapes, though Pekeris [37] has shown these to have limitations under some circumstances. A typical small aperture in an airframe is a gap between panels, which can be treated as a long slot. Fante [38] derives radiated fields of an infinitely long slot with some approximations. The analytic derivation varies with the shape, dimensions and orientation of the structure. On the other hand, Pozar [16] shows the penetrated fields of an electrically small aperture can be approximated by the radiation from small electric and magnetic dipoles. Miller [39] and Rao, Wilson and Glison [40] show by using the equivalent surface theory, the complex radiating structure can be replaced by a number of sources that produce the same radiating field. Such a method gives more flexibility, since the shapes and dimensions of the apertures vary significantly in an airframe. Moreover, the FDTD mesh used to implement the model may also vary in size. Therefore the equivalent source method is chosen for our modelling work, the equivalent source is constructed by an array of electric and magnetic dipole moments, which are fitted by using the GA.

2.2. Setup of the MATLAB GA to find the dipole model

As described, the modelling technique is based on representing radiating structures by an array of dipole moments, which is obtained by the GA. The MATLAB GA is used as it is simple to use and the related data processing is based on MATLAB as well. Most of the GA settings are kept as default, as it was found satisfactory performance was obtained by using the default settings. The details of the GA settings are described in Appendix IV.

Since the dipole moment is defined as the product of the aperture polarisability and the incident field (as shown in Equation 1.7 and Equation 1.8), the GA is not programmed to fit the polarisability directly as the incident field intensity is also an unknown factor. Too many unknowns will mislead the algorithm to find wrong answers. Instead, the current flowing on the equivalent dipole is fitted. The dipole moment can be written as a function of current as $p = \frac{I_e dl}{j\omega}$ for the electric dipole moment and $m = \frac{I_m dl}{j\omega}$ for the magnetic dipole moment. Where I_e and I_m are equivalent electric and magnetic currents respectively, dl is the size of the dipole and ω is the

angular frequency of the current. In these formulae, only the currents are unknowns. The dipole moments are then calculated using the fitted currents, which in turn are used to compute the aperture polarisability for the input to the FDTD model introduced in Chapter 3. The equivalent magnetic dipole for an aperture is dominated by the *x*- and *y*-components, hence in the fitting process, only *x*- and *y*- current components are searched. Each of the components is treated as a complex source, and real and imaginary components are searched separately. Therefore, there are 4 design variables for each of the magnetic dipole moments.

'Adaptive feasible' is set as the mutation function of this GA. The adaptive feasible mutation function randomly generates directions that are adaptive with respect to the last successful or unsuccessful generation. [41]

For a GA to operate efficiently, it is important to accurately estimate the search bounds. The search domain cannot be too big, as the result would be a time consuming search; while it must be big enough to avoid the answer falling outside of the search domain. Equations that analytically calculate the radiated field from a dipole are used here to set the search bounds. Taking the electric dipole moment as an example [42]:

$$E_\theta = j\frac{\eta_0 Idlk}{4\pi r}\left\{1-\frac{1}{k^2r^2}+\frac{1}{jkr}\right\}e^{-jkr}\sin\theta \qquad \textbf{(2.1)}$$

where the symbols have their usual meanings. Taking the magnitude of the complex terms, the expression can be reduced to

$$\left|E_\theta\right| \cong 30\frac{dlk}{r}\left\{\left|1-\frac{1}{k^2r^2}+\frac{1}{jkr}\right|\right\}I \qquad \textbf{(2.2)}$$

From the maximum measured electric field intensity, $E_{\theta\max}$, an upper bound of the dipole current I_{max} can be estimated as

$$I_{\max} = \frac{E_{\theta\max}}{30\frac{dlk}{r}\left\{\left|1-\frac{1}{k^2r^2}-j\frac{1}{kr}\right|\right\}}D \qquad \textbf{(2.3)}$$

To make sure the search domain contains the answer, the maximum electric field in the measurement, $E_{\theta max}$, is used here. Furthermore, a scaling factor D is used to expand the search bound in order to compensate the errors from the above estimation.

Apart from the estimation of the search bounds, the cost function also plays a crucial role in the operation of the GA. It must reflect the fitness of the design variables

and guide the GA towards the answer efficiently. The cost function, in this case, is simply the average difference between the field that the GA-fitted dipole produced and that of the measurement. For the *x*- field component, the cost function is:

$$C_x = \frac{1}{N_y N_x} \sum_{n_y=1}^{N_y} \sum_{n_x=1}^{N_x} \{ \left| E_{GA}^{y} - E_{mea}^{y} \right| \} \qquad \textbf{(2.4)}$$

Where N_x and N_y are the number of points along the *x*- and *y*- axes on the observation surface. E_{GA} and E_{mea} represent the radiated electric fields produced by the dipole moment from the GA and that (measured or) calculated. The total cost is then:

$$C = C_x + C_y \qquad \textbf{(2.5)}$$

According to equivalent surface theory, transvers field component is sufficient to predict an equivalent source. Therefore, the total cost is the sum of the transverse field components and the normal field component is excluded from the cost function. In Equation 2.5, the total cost is the sum of *x*- and *y*- polarised fields. Since in the validation tests in the next section, the *x*- and *y*- polarised fields are transverse fields and the *z*- polarised is normal field.

2.3. Tests and Discussions

2.3.1. Validation test using analytically generated field

Using the above set-up, the operation of the GA was tested using the radiated field from two electric dipoles that were calculated theoretically using Equation 2.1. The two magnetic dipoles were identically 3mm in size and placed 15cm apart. The excitation current on the dipoles was 7.96 μA at 2 GHz. The calculated field was fed to the GA, to see if the GA could find the dipole moments that reproduced the field accurately. 300 generations were run with a population size of 50. The cost function is as shown by Equations 2.4 and 2.5. It is simply the mean difference between the *x*- and *y*- polarised electric field radiated by the dipoles fitted by the GA and those calculated with 7.96 μA flowing on the dipoles. As discussed in Section 1.5.4, the equivalent source can be obtained by using only transverse field components.

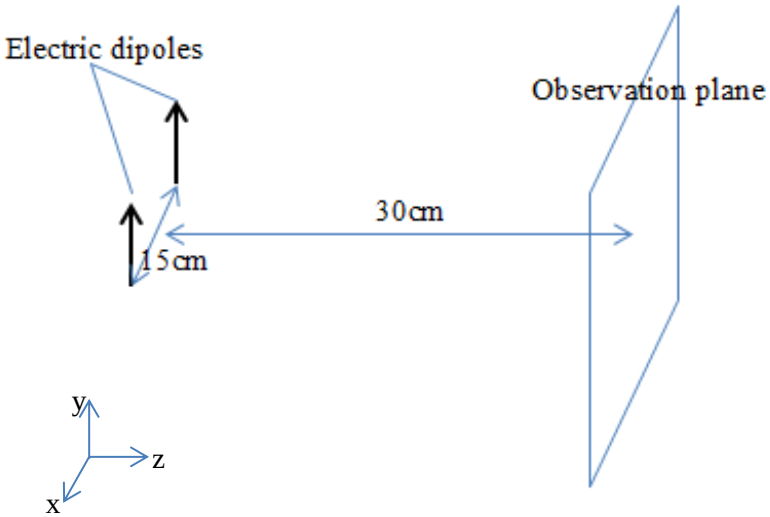

Figure 2.1 Geometry of GA test with two electric dipoles separated by 15cm, and an observation plane 30cm from the plane in which the dipoles are placed

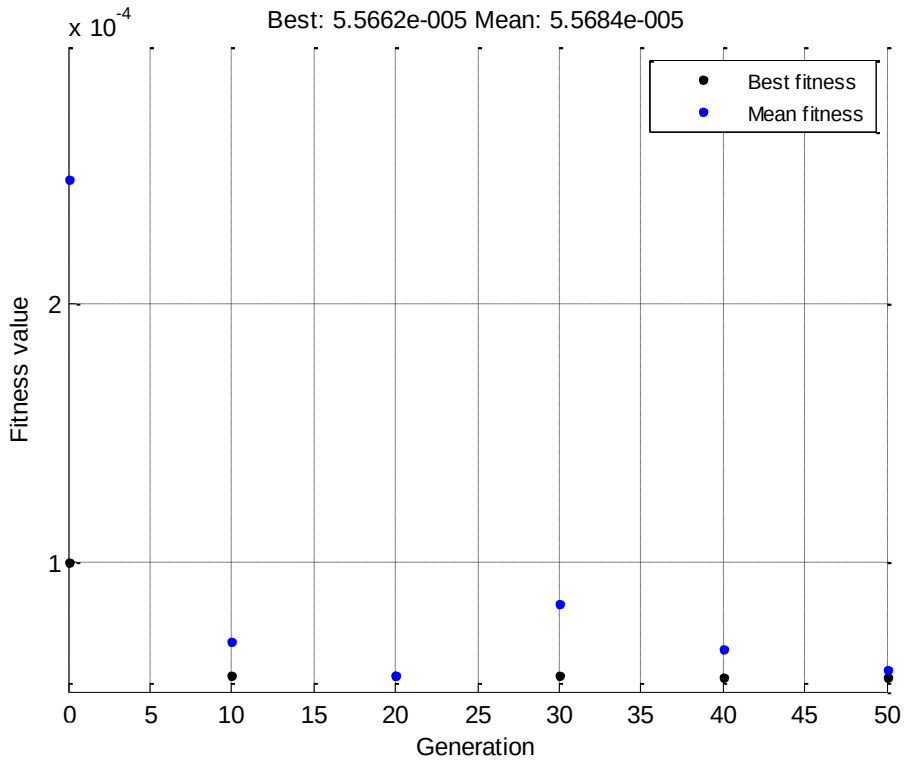

Figure 2.2 Fitness of GA results; the initial value is close to the final result

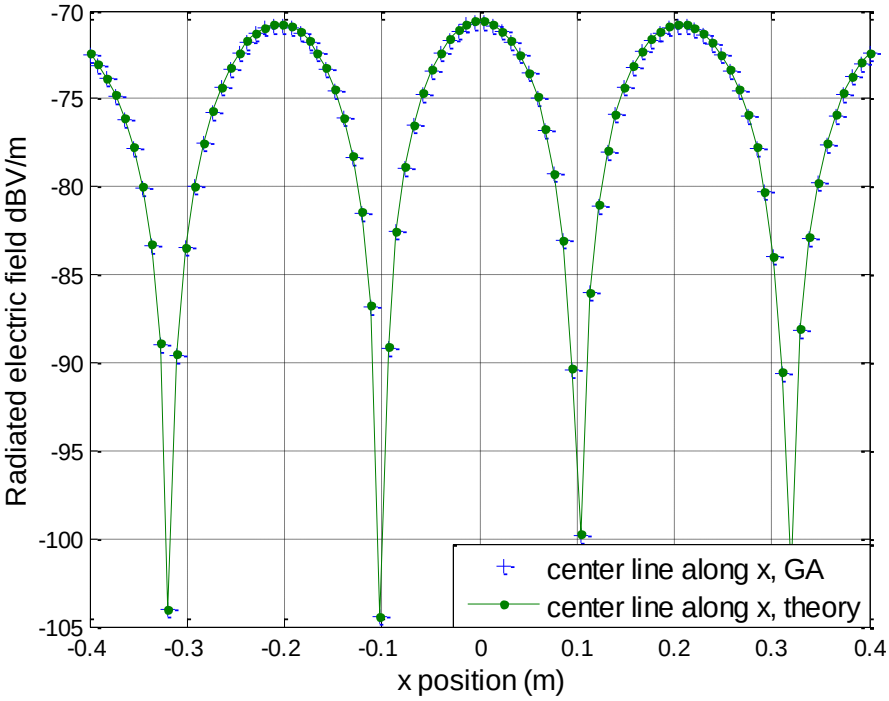

Figure 2.3 Radiated electric field at 2GHz from GA fitted dipole moment and theoretically calculated dipole moment

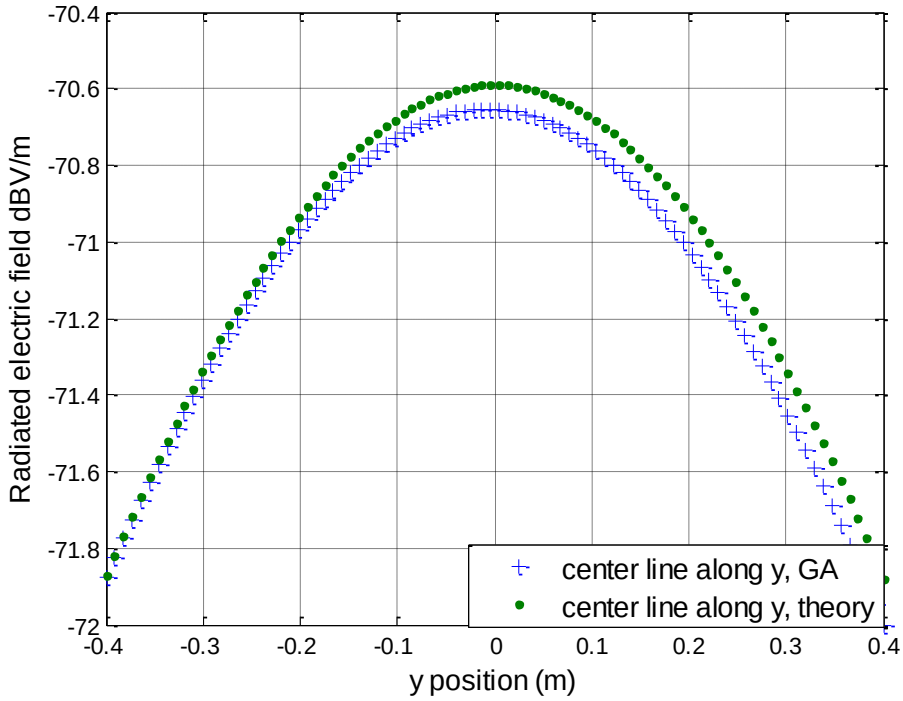

Figure 2.4 Radiated electric field at 2GHz from GA fitted dipole moment and theoretically calculated dipole moment

Figure 2.3 shows the fitness of the first 50 generations; the fitness value of the initial population, which is restricted within the search bound, is close to that of the 50th

generation. The slow convergence after 20 generations indicates the GA had approached the bottom of the fitness surface. Thus the search bound was estimated accurately and a fast convergence was achieved. It can be seen in Figure 2.3 and Figure 2.4 that with the set-up described above, the GA was capable to find the dipole moments in Figure 2.1 within 300 generations. The run time was approximately 1 minute. The GA is therefore considered to be accurate and efficient with the configuration described in this section, and this set-up is used for further verifications and applications.

2.3.2. Validation test using measurement data

Having verified that the GA was capable of finding the dipole moments using analytically generated fields, it was used to fit equivalent dipole moments, representing a real aperture array as shown in Figure 2.5. The slot array consists of six 2×1 cm slots separated by 5mm, cut into a 1.65mm thick aluminium sheet.

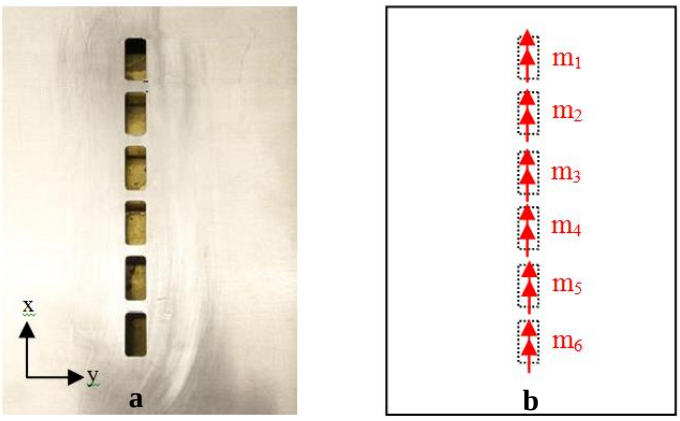

Figure 2.5 a) Slot array b) Equivalent magnetic dipoles distribution of the slot array

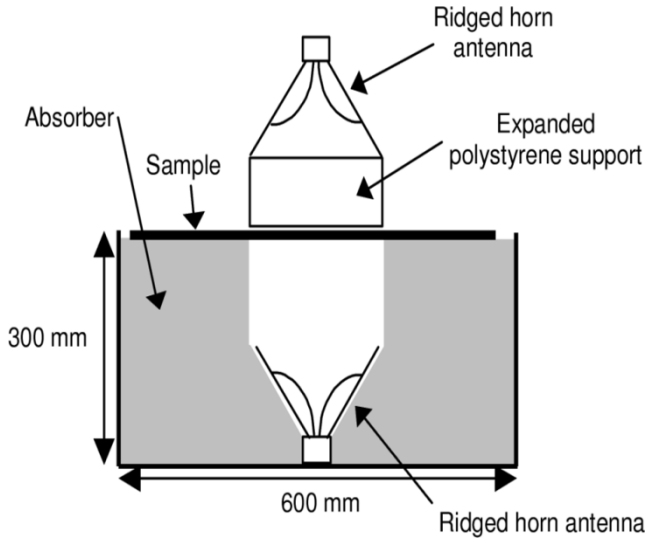

Figure 2.6 Side view of the absorber box [43]

The slot array was placed on the absorber box and illuminated using an EMCO3117 horn antenna. The Absorber box, as shown in Figure 2.6, is designed to provide free-space environment for the shielding effectiveness measurement of the material placed on top of the box. It creates the free-space environment by surrounding the illumination antenna by absorbers. The fields radiated by the antenna is absorbed upon reaching the absorber, and the fields in the hole cut into the absorber can be treated as propagating in free space. The absorber box saves measurement time and cost by allowing the measurements of material plates to be carried out in a smaller room; while such measurements in an anechoic chamber will need edge treatment of the material plates and complex setup [43]. The absorber box is described with more details in Chapter 4 with other measurement devices.

The incident electric field was y-polarised and measured 7mm above the plate. The measurement covered an 18 × 18 cm area to ensure the measurement surface complied most of the penetrated EM energy. Only the *y*- component of the electric field was measured, so each of the slots was assigned an *x*-polarised magnetic dipole moment only, instead of both *x*- and *y*- components in the previous test. The GA was then used to find the equivalent dipole moments that reproduced this electric field; it had the same setup as the verification test using the analytically generated field in Section 2.3.1.

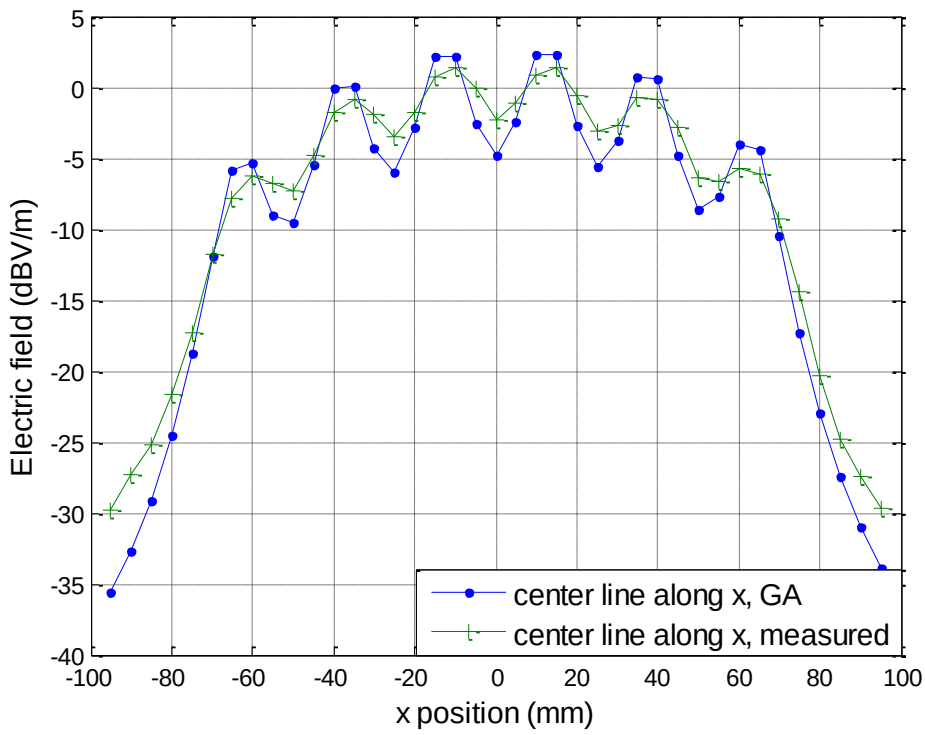

Figure 2.7 *x*-axis cut of electric field produced by GA and measurement

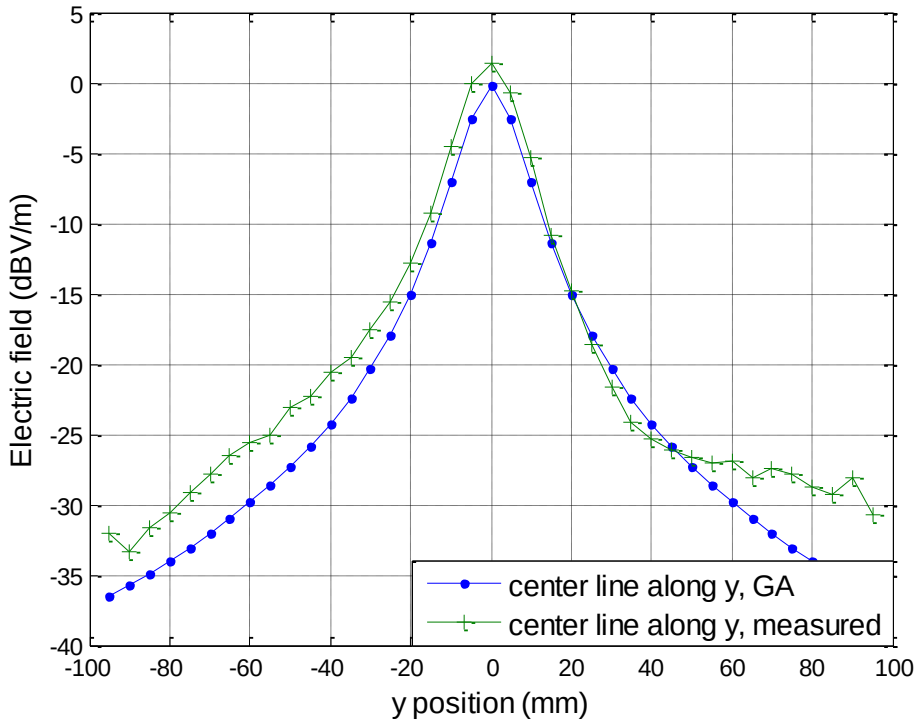

Figure 2.8 y-axis cut of electric field produced by GA and measurement

The radiated field from the GA-fitted dipole moments were simply the sum of each element; therefore no mutual coupling was accounted for. The finite size of the dipole used in the measurement had an averaging effect on the field across its length. Furthermore, the complex interactions between the field and the plate, such as the ringing effect at the edge and interference between the incident field and reflected field at the panel, made the wave front different from that which the GA fitted dipole moments reproduced. In summary, in 300 generations, the GA minimised the cost function so that the searched dipole moments could produce the radiated field close to the measurement. However, due to the unaccounted field interactions, the GA result did not perfectly match the measured field. The tuning of the GA to improve its performance is discussed in the following section.

2.3.3. Discussion on GA performance with changing operators

The goal of this research program is to find an equivalent source, which is not necessarily one dipole moment per aperture. Therefore, to improve the GA results, more dipole moments were assigned and the results were observed. It was considered that by increasing the dipole moment density, more spatial details could be reproduced.

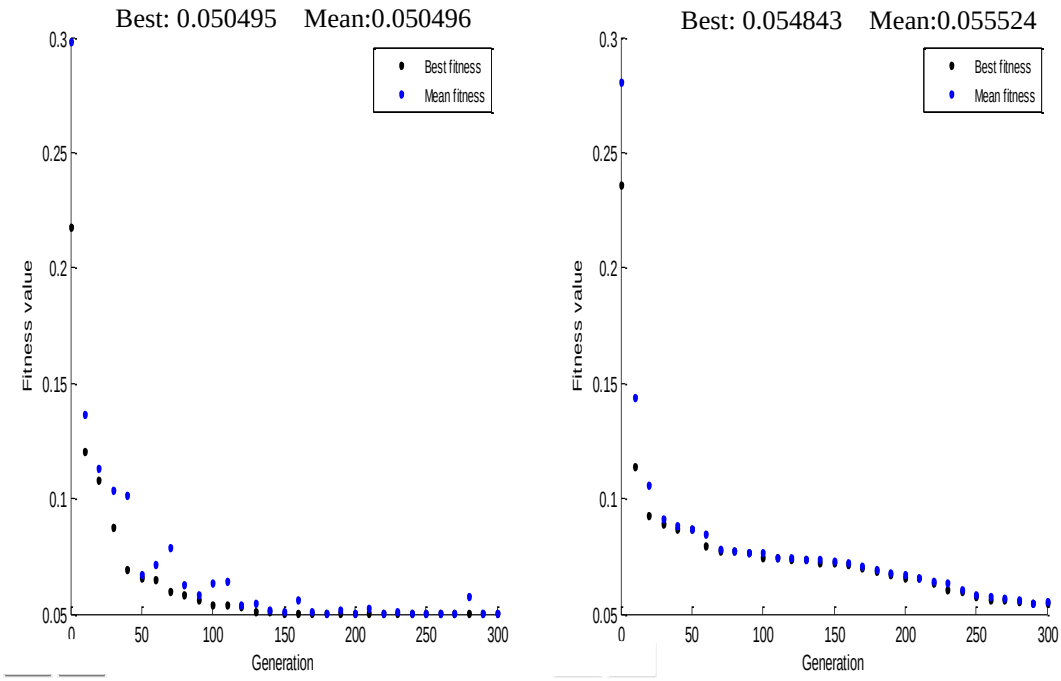

Figure 2.9 GA fitness graph of fitting slot array with 6 dipole moments (left) and 30 dipole moments (right)

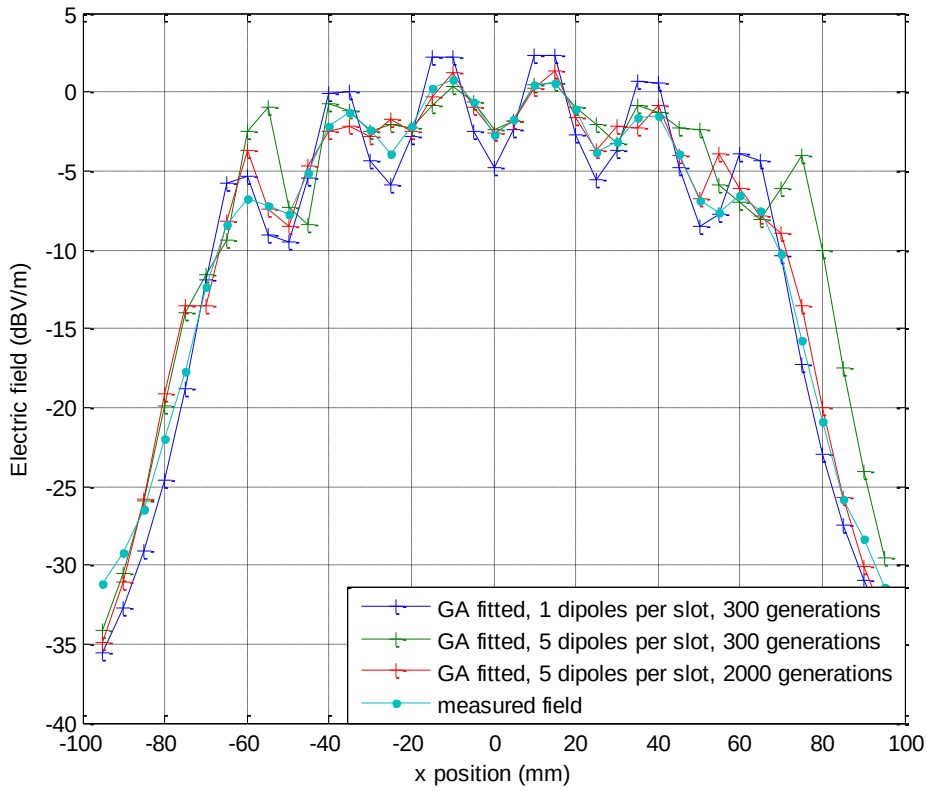

Figure 2.10 Result of GA fitting equivalent dipole moment source with increased dipole density

In Figure 2.10, the result of increasing the density of the dipole moments is shown. The number of dipole moments per aperture was increased from 1 to 5. Three dipole moments were used to represent the field across each of the slots, and 1 dipole moment on each edge of a slot to enhance the details at the edge. By observing Figure 2.10 it can be seen that after increasing the number of dipole moments, the reproduced field fitted more closely to the measurement, especially in the centre area where the field intensity was higher. At the sides where the field intensity started to decrease, the reproduced field from the GA-fitted dipole moment started to deviate from that of the measurement.

The increase of spatial dipole moment density results in an increase in the spatial resolution that the reproduced field needs to follow. It is considered that a GA search of 300 generations could not cope with such complexity. Figure 2.9 shows the fitness of the GA cost function as generation evolves. It is observed that when 30 dipole moments were used, the reduction of the fitness level was slower. Although both graphs achieve similar fitness levels after 300 generations, the GA fit with 30 dipole moments was expected to have a lower final fitness than that with 6 dipole moments. In other words it had not converged to its expected best result. Therefore, the number of generations run by the 30 dipole moment search was increased to 2000. It is obvious that some deviated points have been brought closer to the measurement result. However the price paid for this improvement is a significant increase in run time from about 3 minutes for the 300 generation run to 20 minutes. When building the model, careful consideration needs to be made for the compromise between accuracy and run time.

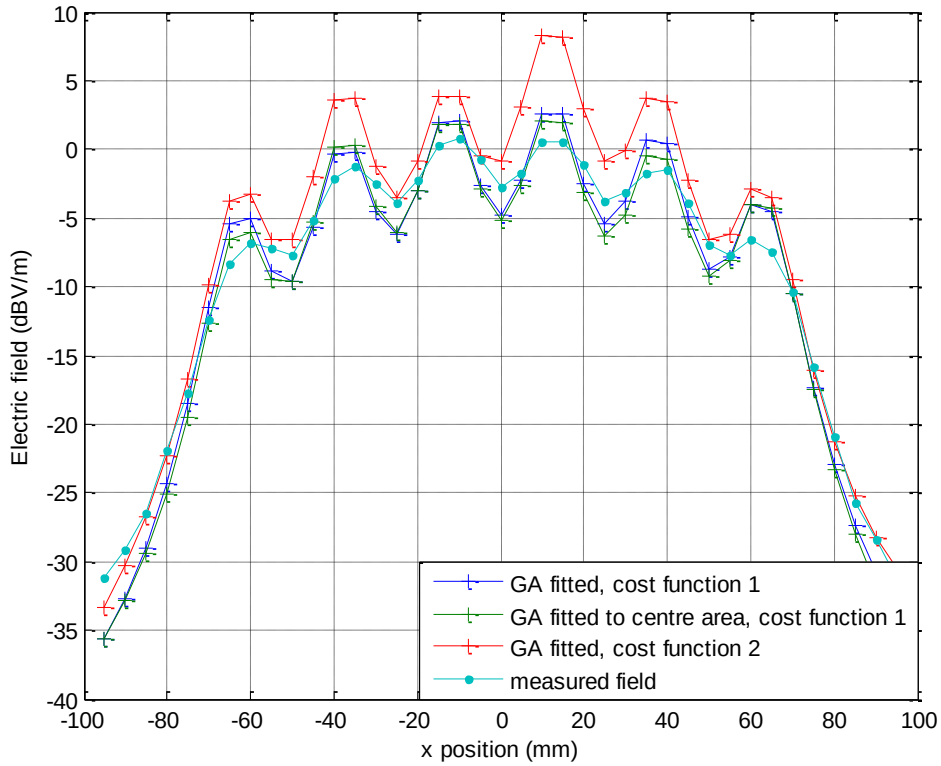

Figure 2.11 Test of performance of GA with different cost functions

As mentioned in Section 2.1, another way to improve GA performance is to choose an efficient cost function. Figure 2.11 shows results of the GA with different cost functions. Three tests were carried out with two cost functions.

$$C_x = \frac{1}{N_y N_x} \sum_{n_y=1}^{N_y} \sum_{n_x=1}^{N_x} \{ \left| E_{GA}^{y} - E_{mea}^{y} \right| \} \qquad \textit{Cost Function 1}$$

$$C_x = \frac{1}{N_y N_x} \sum_{n_y=1}^{N_y} \sum_{n_x=1}^{N_x} \{ \left| \left(\log_{10} \left| E_{GA}^{y} \right| - \log_{10} \left| E_{mea}^{y} \right| \right) \right| \} \qquad \textit{Cost Function 2}$$

Cost Function 1 is the one used in the previous tests, which is the mean error of the field magnitude in complex form across the measurement surface. *Cost Function 2* is the mean error of decibel values of the field. The decibel value magnifies the difference between small numbers; however this cost function does not contain phase information. An additional test on *Cost Function 1* was run with reduced measurement surface. The centre 14.5 × 18 cm area is taken from the 19.5 × 19.5 cm measurement plane. Since most of the energy is concentrated in this area, it was expected this attempt would reduce the computational load without seriously affecting the accuracy of the result. However this method can only be used when the field pattern radiated from the

structure is known. In addition, this method requires that the radiated field has an area where most of the energy is concentrated, so that ignoring the field with lower amplitude will not induce significant error. In the above GA fit, fields of 15 dBV/m lower than the maximum measured field intensity were ignored and the difference between the results that were fit using the measured field from all of the measurement points was 1 dB.

It is shown in Figure 2.11 that the phase information is important, as the magnitude-only *Cost Function 2* falls far from the results of the others. On the other hand, the computational load can be reduced by making the GA fit to the area where most of the energy concentrates, while the accuracy of the GA results is maintained.

2.4. Summary

This chapter has described the GA setup in MATLAB for fitting dipole moments as equivalent sources to reproduce the EM fields penetrating small apertures. The GA was set to fit the equivalent current flowing on the dipole moments. Both analytically generated and measured fields were used to test the implementation of the GA. The GA was capable of producing satisfactory results within 300 generations for a coarse spatial distribution of the dipole moments, applied on the measured field from an array of small slots. By increasing the density of equivalent sources, the radiated field could be reproduced more accurately. Such an increase in computational complexity requires a longer run time. The trade-off between model accuracy, sampling density and run time is discussed in Chapter 5.

Chapter 3. Modifications to the FDTD update process to implement the equivalent aperture model

This chapter describes the implementation of the macro model of small apertures into the FDTD simulation tool [44]. The FDTD simulation package Vulture was programmed by Dr Ian Flintoft from the Physical Layer Research Group at the University of York. The module of the macro model was added to Vulture by the Author. Firstly, the algorithm that adds the magnetic dipole moment into the FDTD grid is introduced, followed by the description of the modification of the normal FDTD update function so that the algorithm is implemented. Then the results of the validation tests are shown. Firstly, the model was tested in a fine-grid mesh which had the same mesh size as the aperture simulated. Then the algorithm was tested as a macro model, using a coarse-grid mesh with a mesh size larger than the aperture being modelled.

3.1. The Finite-Difference Time-Domain Method

The FDTD method for computational electromagnetics was introduced in Section 1.5.3. Recalling the field structure as shown in Figure 3.1, each mesh in an FDTD simulation stores six field components and updates them in each time step. The field updating process of the FDTD algorithm works in a leapfrog manner. As shown in Figure 3.1, though the field components are stored in the same mesh, they are spatially separated. The electric fields are calculated at the edges of the mesh, and the magnetic fields are located in the centre of the faces of the mesh. In the time domain, the updating of the electric fields and the magnetic fields are separated by half a time step. As can be seen in Equations 3.4 and 3.5 in Section 3.3, the electric field and magnetic field updating are separated by half of a mesh size in the spatial domain, and half of a time step in the time domain.

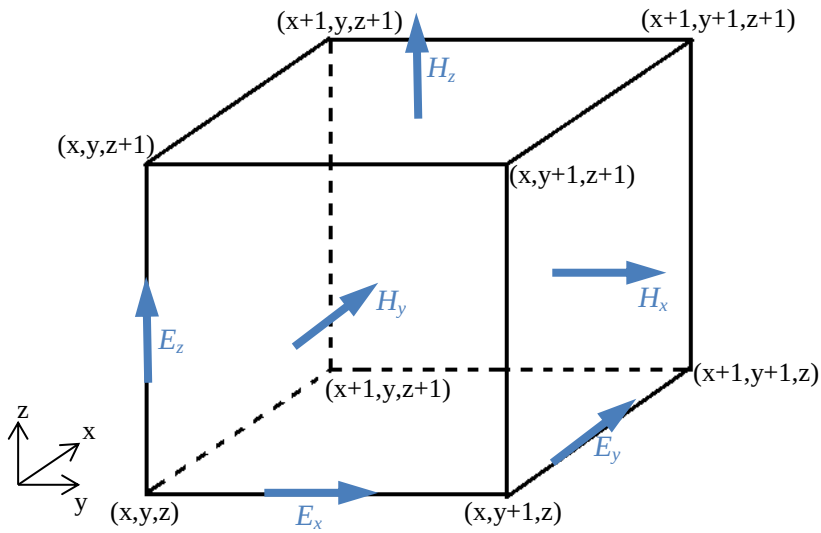

Figure 3.1 Field structure of an FDTD mesh, reproduced from [24]

When exciting a field in an FDTD mesh, there are 'soft' field sources and 'hard' field sources. A 'soft' field source in the FDTD method adds the source field to the existing field in the FDTD grid, while a hard source replaces the existing field in the grid by the source field.

3.2. Modelling macroscopic structures in FDTD meshes

Having discussed the methods involved in this modelling work and the optimisation method used to find the model parameters, we are ready to progress the modelling work to the building of macro models, using the described methods. It has been shown in Section 1.5 that electrically small apertures can be approximated as infinitesimal dipole moments. In our case, the sub-cellular models of small apertures are built as dipole moments in FDTD meshes, with the excitation amplitude searched by the GA. In the far-field region, in which the distance to the structure is comparable to the structure size, the reactive field components have sufficiently been reduced, and the model is expected to produce the same field as that radiated from the small structures. In addition, as the model is an equivalent source instead of a detailed reproduction of the original source, the distribution of the dipole moment may not be the same as that of the small structures. For example, an array of small radiating structures built in a large mesh may be able to be represented by a single equivalent dipole moment, when the mesh is large enough and the array can be approximated as a single point source.

3.3. Algorithm introduction

This model employs the method introduced by Martin [18][45], where the field produced by the effective magnetic dipole moment is characterised in terms of polarisability and magnetisation of the aperture. The magnetisation of the aperture, also called magnetic dipole moment density, is defined below in Equation 3.1:

$$\boldsymbol{m} = \int_V \boldsymbol{M} dV' = \boldsymbol{M}V \qquad \textbf{(3.1)}$$

And the magnetic flux density $\boldsymbol{B}$ in the corresponding FDTD mesh is:

$$\boldsymbol{B} = \boldsymbol{\mu_0}(\boldsymbol{H} + \boldsymbol{M}) \qquad \textbf{(3.2)}$$

Where $\boldsymbol{m}$ is the magnetic dipole moment, $\boldsymbol{M}$ is magnetisation, V is the volume of the FDTD mesh in which $\boldsymbol{M}$ is calculated and μ_0 is permeability of free space. Equation 3.2 shows that the effect of the magnetic dipole moment can be simulated by adding the magnetisation to the magnetic field of the mesh.

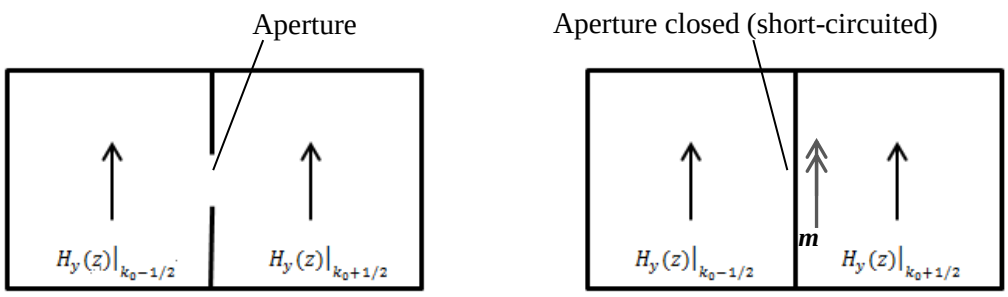

Figure 3.2 The FDTD aperture model (left), and the aperture replaced by the equivalent source and PEC (right)

Figure 3.2 is a 2-D illustration of the FDTD meshes before and after the equivalent dipole moment model is inserted. k_0 is the mesh that is being updated, $\boldsymbol{m}$ is the equivalent magnetic dipole moment. As shown in Figure 3.1, there is a half-mesh offset in the locations between the electric and magnetic fields stored in an FDTD mesh. k_0 in Figure 3.2 is referenced to the location of the electric field in the mesh being updated, so the magnetic field on the left side of the aperture is at k_0-1/2 mesh size, while on the right side of the aperture it is at k_0+1/2. Assume the incident magnetic field comes from the left of the grid, and the model is in the mesh on the right, located at k_0+1/2. The equivalent dipole moment is calculated using the short-circuited magnetic field $H_y|_{k_0-1/2}$ discussed in Section 1.5.1:

$$\mathbf{m} = \boldsymbol{\alpha_m} \boldsymbol{H_{sc}} \qquad \textbf{(3.3)}$$

The magnetisation at $k_0 + 1/2$ is then calculated using $H_y\big|_{k_0-1/2}$ as:

$$\boldsymbol{M_y(z)}\big|_{\boldsymbol{k_0+1/2}} = -\frac{\boldsymbol{m}}{\boldsymbol{V}} = -\frac{\boldsymbol{\alpha_m(z)}}{\boldsymbol{V}}\boldsymbol{H_{y\,sc}(z)}\big|_{\boldsymbol{k_0-1/2}} \qquad \textbf{(3.4)}$$

Where α_m is the magnetic polarisability of the aperture and $H_{y\ sc}$ is the short-circuited y-polarised magnetic field at the aperture, which is the magnetic field with the aperture closed. In FDTD, the magnetic field source is related to both the magnetisation of the last time step and the current time step as shown in Equation 3.5:

$$\boldsymbol{H_y(z)}\Big|_{\boldsymbol{k_0+\frac{1}{2}}}^{\boldsymbol{n+1}} = \boldsymbol{H_y(z)}\Big|_{\boldsymbol{k_0+\frac{1}{2}}}^{\boldsymbol{n}} - \boldsymbol{M_y(z)}\Big|_{\boldsymbol{k_0+\frac{1}{2}}}^{\boldsymbol{n+1}} + \boldsymbol{M_y(z)}\Big|_{\boldsymbol{k_0+\frac{1}{2}}}^{\boldsymbol{n}} - \frac{\boldsymbol{\Delta t}}{\boldsymbol{\mu_0}}(\boldsymbol{\nabla_{FDTD}} \times \boldsymbol{E})_{\boldsymbol{y}}^{\boldsymbol{n+1/2}} \qquad \textbf{(3.5)}$$

In Equation 3.5, *n* is the current time step and the $\frac{\Delta t}{\mu_0}(\nabla_{FDTD} \times E)_y^{n+1/2}$ term is the FDTD update function of the electric field. By inspecting Equation 3.5, it is effectively the original update equation with two $\boldsymbol{M_y}$ terms inserted. Therefore, the modification to the original FDTD magnetic field update function consists of two steps: 1) calculate the magnetisation at the current time step and 2) pass the magnetisation to the update of the next time step. The algorithm adds the effect of the aperture onto the field that the FDTD calculated without the aperture model. In other words, the radiating structure is built as a soft field source.

3.4. Plane wave excitation in Vulture

A plane wave excitation is used as the source to illuminate the apertures throughout this thesis. As mentioned in Huygens's Principle in Section 1.5.4, each point on the propagating wave front can be treated as an individual point source. The truncation of a wave front will therefore break the continuous line of point sources and lead to distortions as it propagates. This is the case when exciting the electric field across a plane in an FDTD volume surrounded by absorbing boundaries. The excited field is truncated at the absorbing boundaries and is no longer a plane wave after the execution of a few time steps. For that reason, plane wave excitation in the FDTD algorithm needs support to eliminate the effect induced by the truncated wave front at the absorbing boundaries.

The plane wave excitation in Vulture uses Huygens's sources (also called Total-Field Scattered-Field (TFSF) sources). This technique supports the plane wave by defining a bounding box inside the FDTD simulation volume. The simulation volume is

divided into two regions: Region 1 is inside the bounding box; in this region, the total field $\boldsymbol{E_{total}}$, is calculated as the combination of the incident field $\boldsymbol{E_{inc}}$ and scattered field $\boldsymbol{E_{scat}}$, where $\boldsymbol{E_{total} = E_{inc} + E_{scat}}$. In Region 2, only the scattered field is calculated, while the outer boundary of the FDTD volume is set to an absorbing boundary condition (ABC). In this way, the plane wave excited in Region 1 (inside the bounding box) is free to leak out into Region 2 without truncation at the boundary between Region 1 and Region 2 [46].

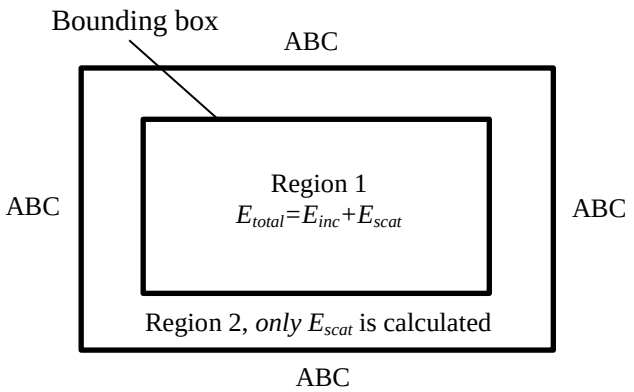

Figure 3.3 The TFSF method for plane wave support

In the application of this method, it was found that the reflected field from a PEC plate is distorted, as shown in Figure 3.4. This is due to Region 1 supporting only the incident wave, leaving the reflected field leaking out into Region 2. Reflection at the Region 2 border is generated due to the truncation of the reflected wave. This reflected wave, though not as strong as the incident wave, can still affect the accuracy of the results, as shown in Figure 3.5.

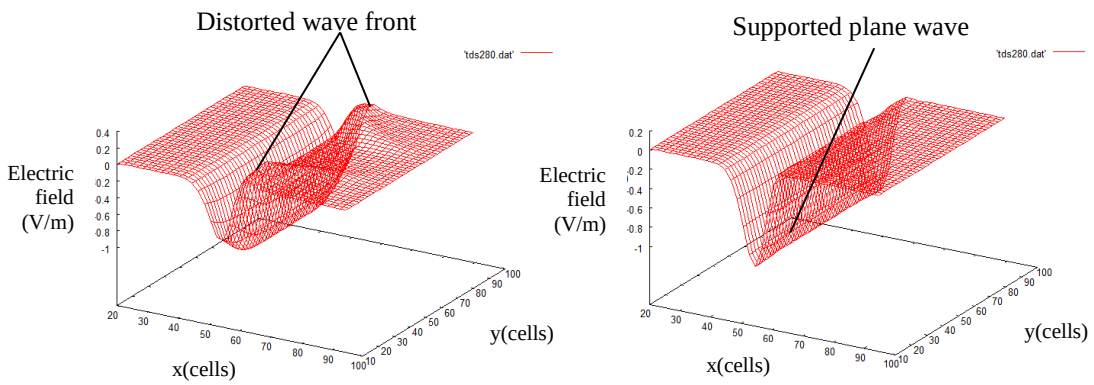

Figure 3.4 Reflected plane wave from a PEC sheet without (left) and with (right) the additional plane wave excitation support

As shown in Figure 3.5, the maximum error induced by the distortion is about 2 dB. This error is small in magnitude, but as shown in Chapter 2 and also in the following

chapters, the errors of the GA fits are comparable to this magnitude. For the purpose of diagnostics and verification of the GA fits, it is important to remove this distortion.

A simple fix of this distortion is to add the plane wave support for the reflected wave, by adding another bounding box. The additional bounding box should support the wave of the same polarisation and at the same incident angle as the incident wave, but propagate in the opposite direction. It should also start at the place and time where the incident wave hits the object. The results are shown in Figures 3.4 and 3.5, where the distortion in the reflected wave in the spatial domain, and the ripples in the frequency domain field transmitted through a small aperture, are eliminated.

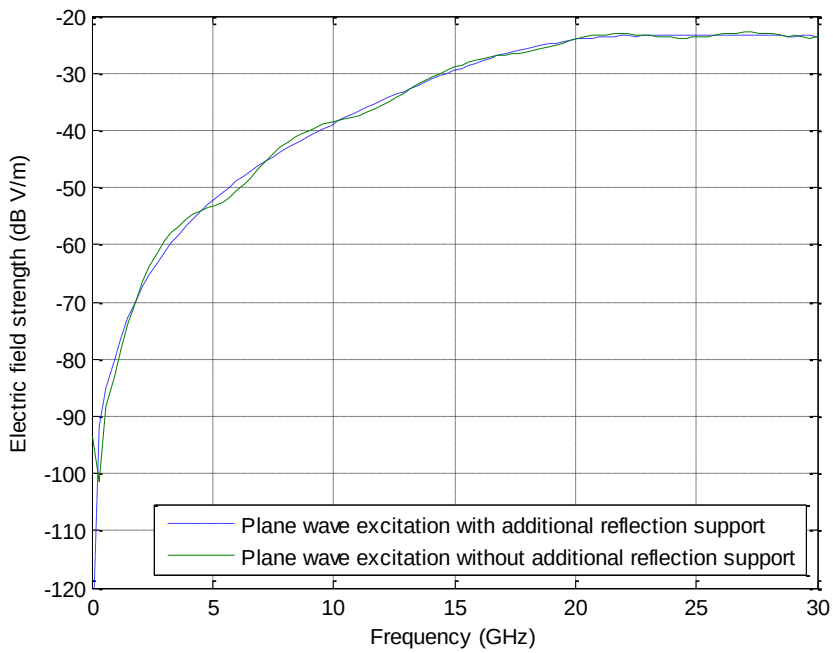

Figure 3.5 Electric field measured behind a small aperture illuminated by a plane wave

3.5. Algorithm implementation and validation

The algorithm described in Section 3.3 was implemented into the FDTD simulation package. The equivalent magnetic dipole moment was implemented and an additional input file was needed for the FDTD code to read the aperture information. The input file should contain the number, location and polarisability of each of the apertures. The model was then tested using the penetrated field of a square aperture in a fine-grid simulation by way of validation according to the following steps:

1) The aperture was built with PEC sheets in the FDTD simulation as shown in Figure 3.6, and the near-field was measured in a plane in this fine-grid model.

2) The GA, introduced in Chapter 2, was applied to fit the polarisability of the equivalent moment using the field obtained in Step 1. The fit was performed at 3GHz, at which the measurement was about 6 wavelengths from the aperture. At this distance, the measurement was electrically far from the aperture and was well out of its reactive near-field. The reactive near-field exists in the region up to one wavelength from a radiating structure. The field variation in the reactive near-field region is so rapid that accurate measurement is difficult to carry out. Therefore it is often avoided to measure fields in the reactive near-field region. The effect of the reactive near-field is discussed later in this chapter.

3) The aperture was then closed and replaced by the equivalent dipole moment as shown in Figure 3.2, where the polarisability was fitted by the GA.

The geometry of the validation test is shown in Figure 3.6. The aperture was 6×6 mm in size in a 1mm mesh size grid, and a measurement plane was placed 7 cm from the aperture plane with output points 4 mm apart. The excitation was a *z*- polarised electric field plane wave travelling down the *x*-axis. The boundaries of the simulation volume were absorption boundaries with 8 PML layers on all sides.

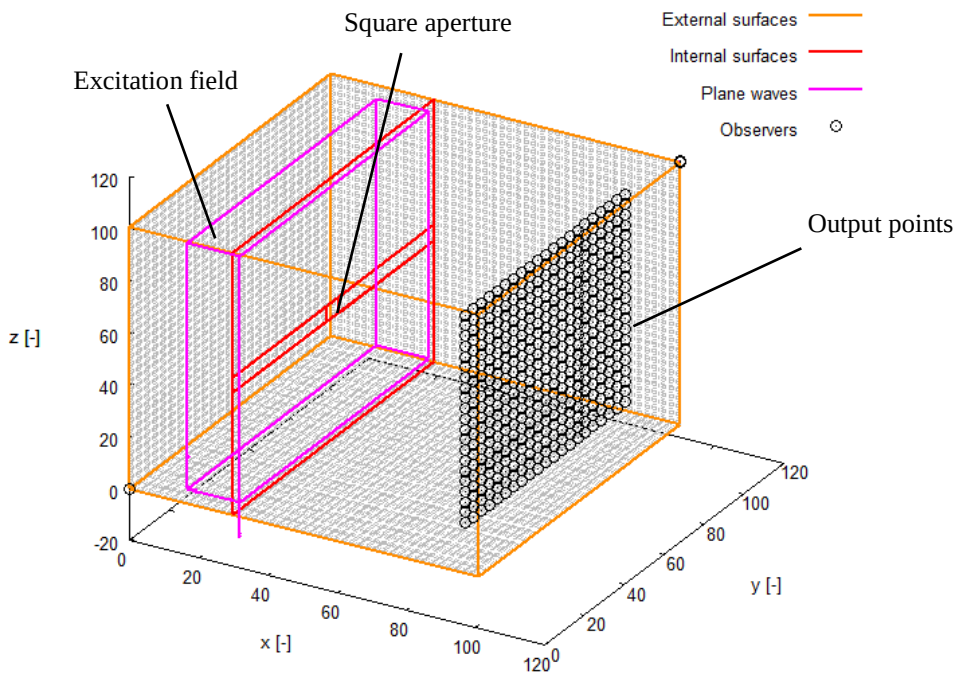

Figure 3.6 Aperture simulated in an FDTD model to obtain the penetrated field to be used by the GA

After applying the GA on the measured fields to find the equivalent dipole moment of the aperture, the aperture was closed with the equivalent model obtained from the

GA placed in front of the PEC. The rest of the model remained the same as shown in Figure 3.6.

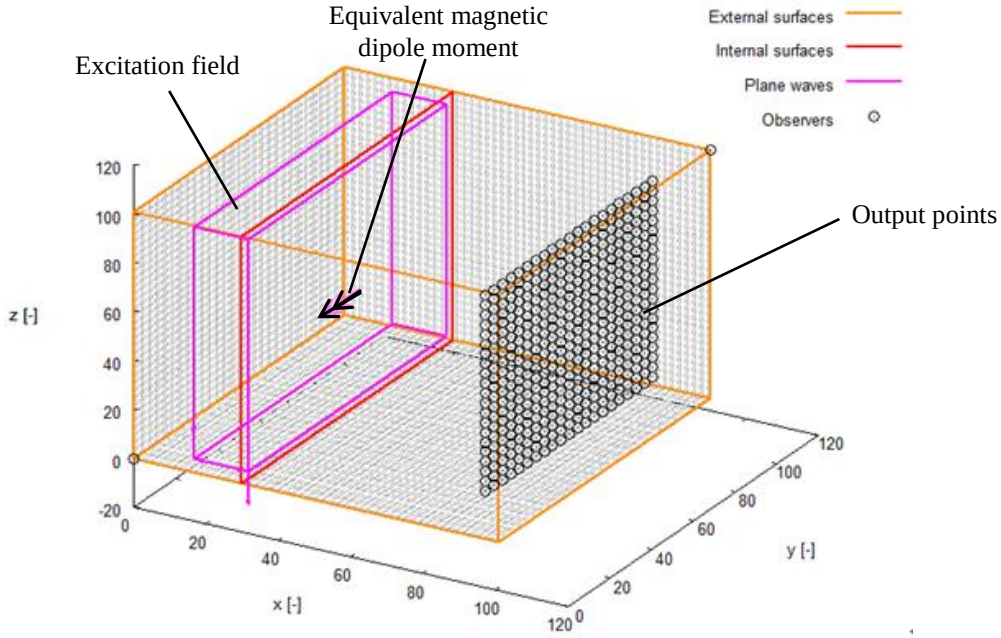

Figure 3.7 FDTD equivalent model of the aperture, with the aperture replaced by a magnetic dipole moment

The polarisability found by the GA was 4.94×10^{-8} m^3 while it was 5.17×10^{-8} m^3 calculated analytically using expression $\alpha_m = \frac{4a^3}{3\pi^{3/2}}$ [47]. Figure 3.8 and Figure 3.9 show the results of the aperture equivalent model in frequency and spatial domains respectively. The polarisability of the aperture is approximated as a constant at low frequencies when the aperture is small compared to the wavelength, therefore differences between equivalent model and the FDTD aperture simulation are expected as frequency increases. It can be seen at low frequencies that the equivalent magnetic dipole model was able to reproduce the aperture field with error of less than 2dB V/m. The two curves start to deviate as frequency increases. In general, the aperture is considered to be electrically large at the frequency where the largest dimension of the aperture is one quarter of the wavelength. In this case, the frequency is 12.5 GHz. This effect can be seen in Figure 3.8, where the results of the equivalent model start to deviate from that of the aperture simulation at about 9.5 GHz. The spatial distribution of the fields has the same shape along both *x*- and *y*- axes, with the error visible in the frequency domain results.

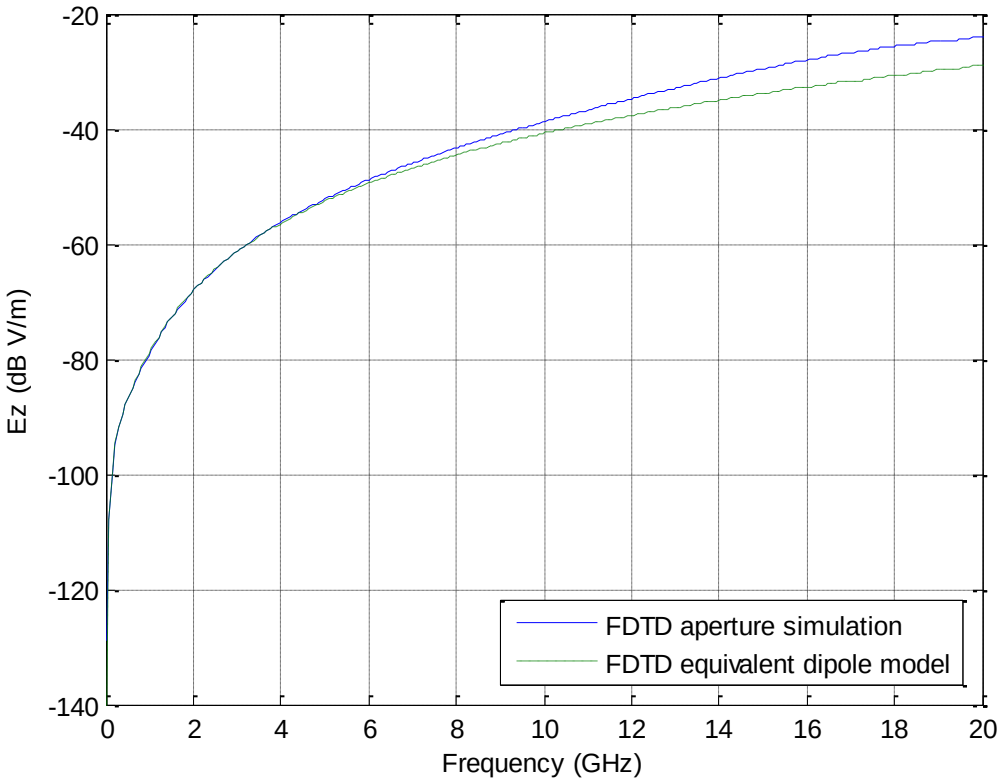

Figure 3.8 Frequency domain result of aperture equivalent magnetic dipole model

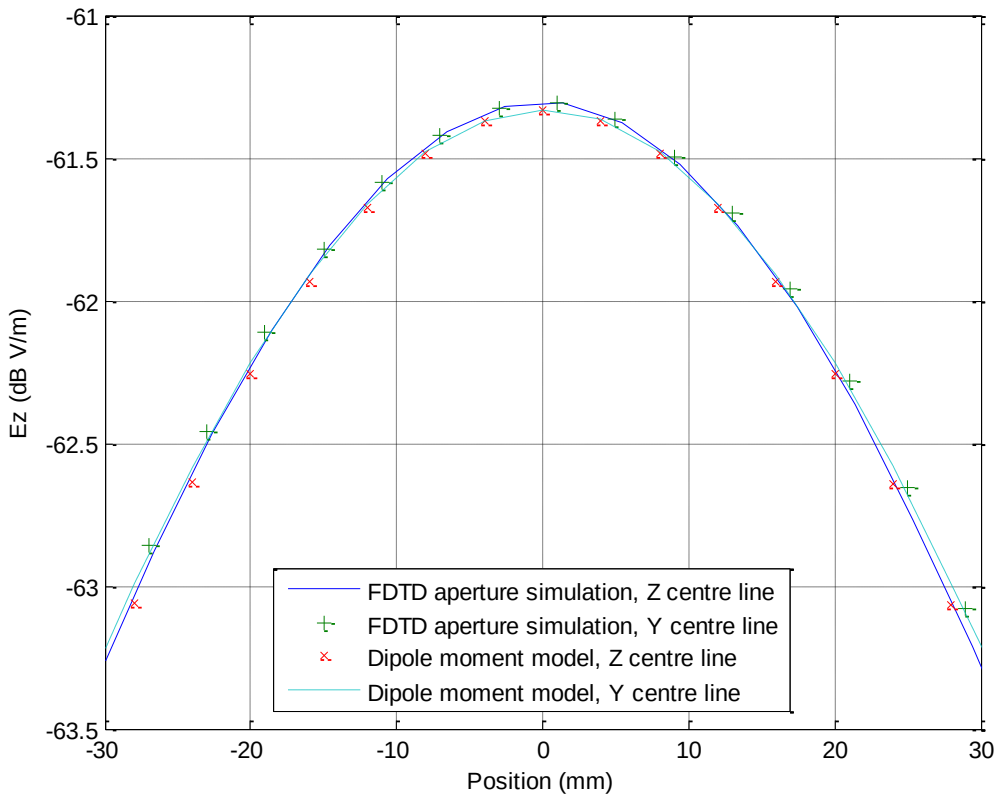

Figure 3.9 Spatial domain result of aperture equivalent magnetic dipole model at 3GHz

3.6. Transformation from fine-grid model to coarse-grid model

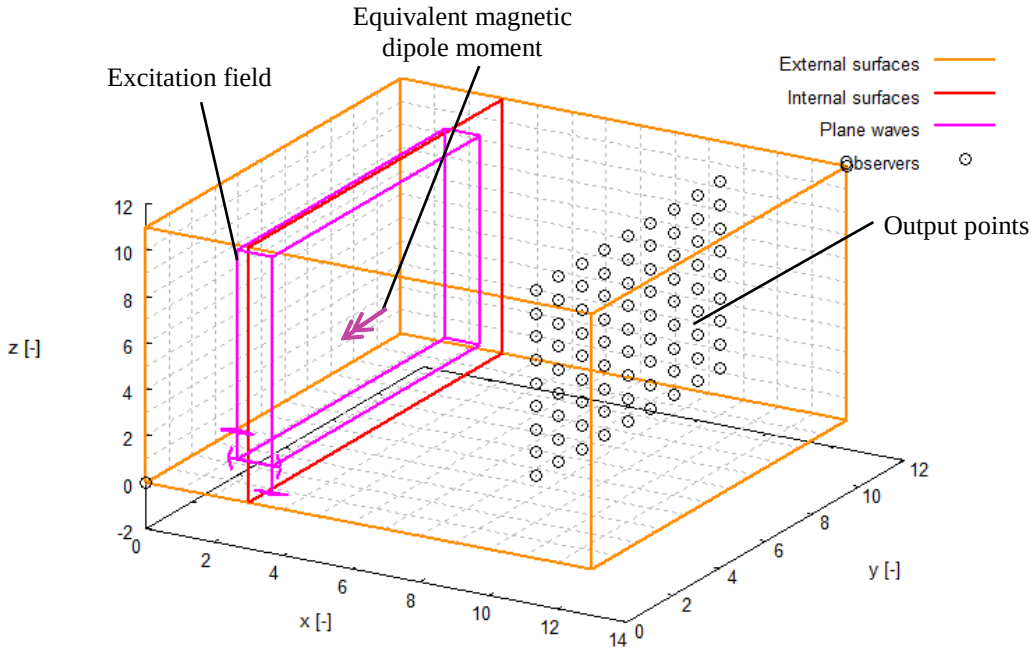

Figure 3.10 Coarse-grid simulation of the equivalent aperture model

Taking one step further from the fine-grid verification, the validation tests undertaken using a coarse-mesh grid, as described in this section, lead the modelling work into the area of sub-cellular modelling. In contrast to the fine-grid model, where the mesh size was 1mm and the aperture 6mm in size, the coarse mesh was 10mm in size in the model shown in Figure 3.10, bigger than that of the aperture. Also, the equivalent dipole model was placed at the same location as in the fine-grid simulation, with the distance between the aperture model and the output plane kept the same, at 60 mm. The spatial resolution of the output points was reduced from 4 mm to 10 mm as limited by the mesh size.

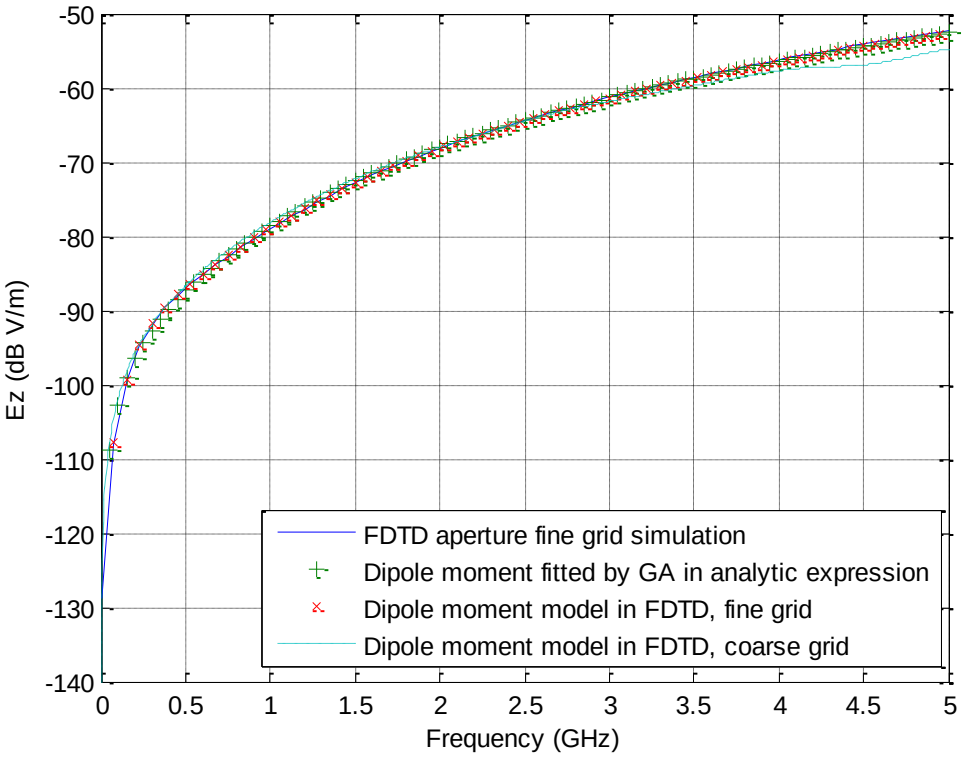

Figure 3.11 Frequency response of fine-grid and coarse grid FDTD simulations and analytic expression

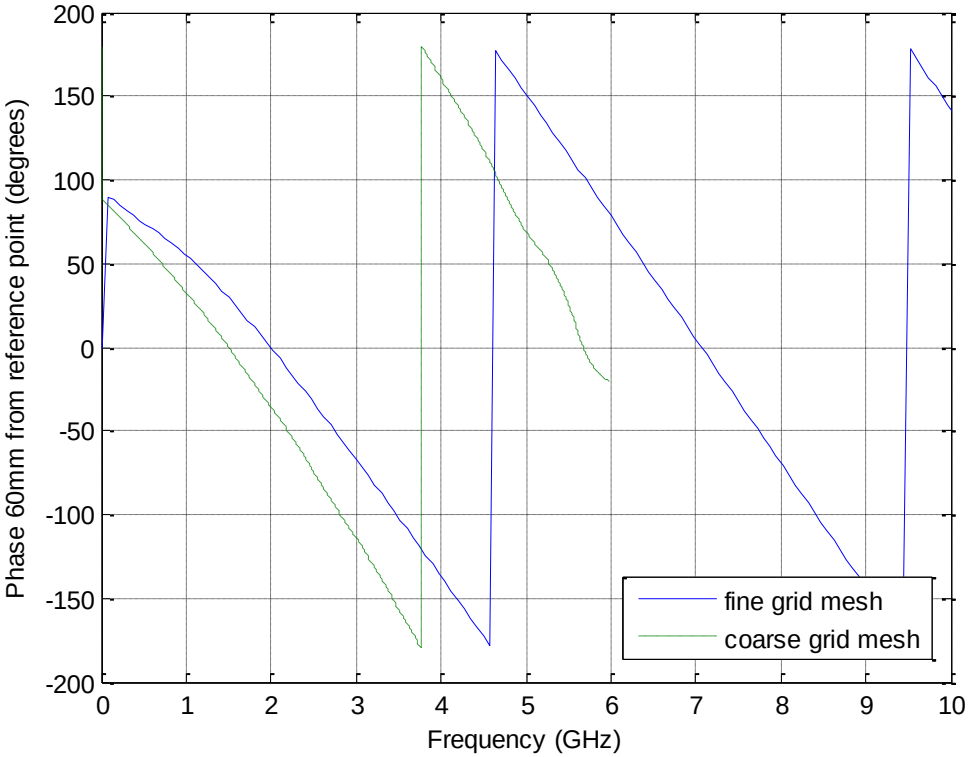

Figure 3.12 Frequency domain phase response of fine-grid and coarse-grid FDTD simulations

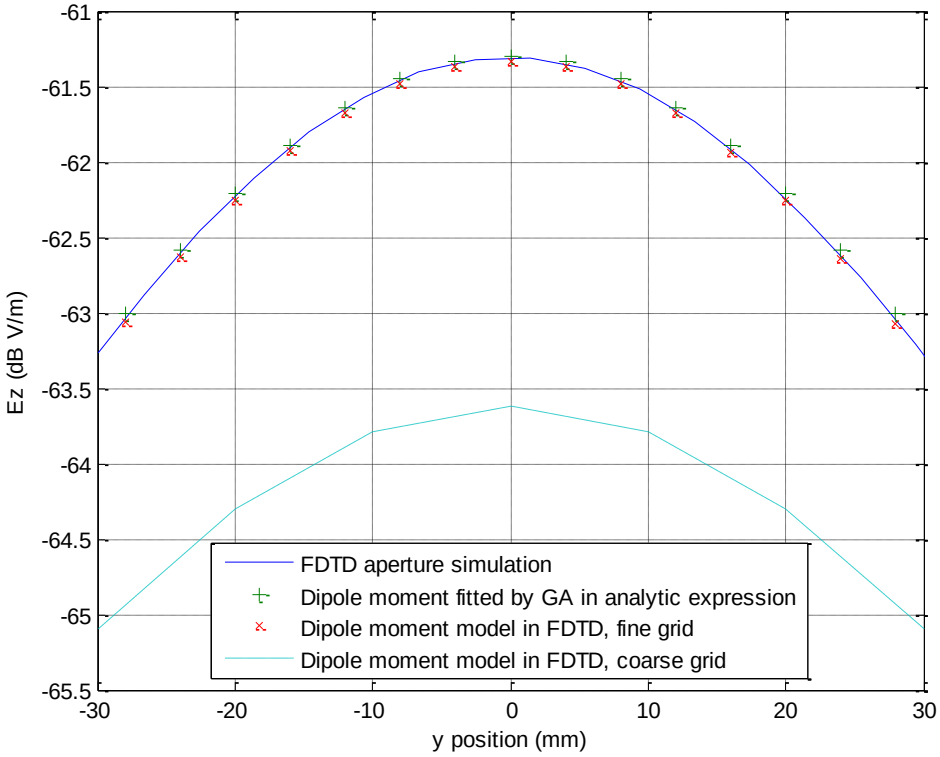

Figure 3.13 Field distribution of fine- and coarse-grid models at 3GHz along z-centre line at 3GHz

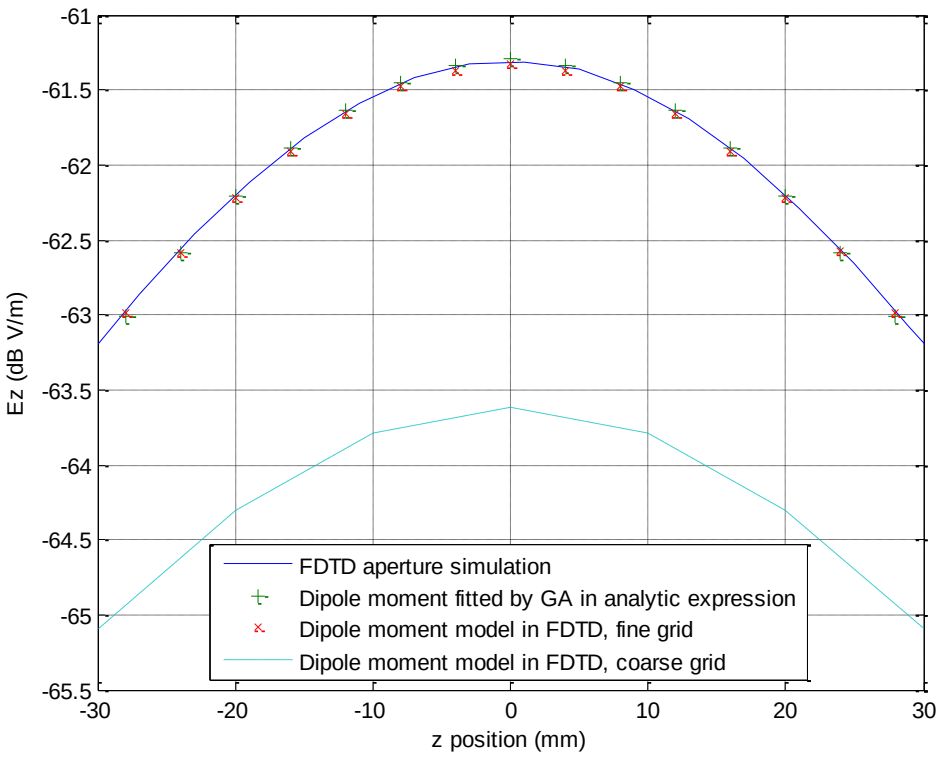

Figure 3.14 Field distribution of fine- and coarse-grid models at 3GHz along y-centre line at 3GHz

Figure 3.11 to Figure 3.14 show that the equivalent macro model in the coarse-grid model can produce the radiated field from the aperture within 2 dBV/m from the fine-grid simulations up to the frequency where the coarse FDTD mesh size is larger than $\lambda/10$ and the simulation loses accuracy. The difference in magnitude was caused by numerical dispersion, which will be discussed in Chapter 5. The result was satisfactory in magnitude; however, in Figure 3.12, the phases are significantly different. There were two sources that generated such a phase difference. Firstly, the algorithm contains an instantaneous field jump across the distance of a mesh size. The change of mesh size resulted in the difference over which the field jumped. In other words, the distances that the fields travelled are different between fine-grid and coarse-grid models. This difference of travelling distance has resulted in difference in phases at the output point. Secondly, the plane wave was excited one mesh away from the mesh specified in the input file, which again resulted in a field travelling distance variation when the mesh sizes varied. This difference exists regardless of whether the distance between the excitation and the equivalent dipole moment was fixed. Therefore, a phase calibration method was developed and this is described below, in order to compare the results of different validation models. Such a phase compensation process may have little influence in the application of the model in full aircraft simulation, since the excitation field comes from the mesh connected to the model instead of a fixed plane-wave excitation; however, this process is of great importance during the model development stage, as it allows us to verify whether the coarse-mesh model produces the correct phase result, and to see whether the time delay of the field matches the computation from the algorithm.

3.6.1. Phase correction method

In order to match the phases produced by the models with two different mesh sizes, a reference point is needed, where the phase information is calibrated. The reference point is chosen as the point where the equivalent dipole model is placed. The phase of the measured field is then subtracted by the phase measured at the reference point. In addition, the difference between the distances that the field jumped in the two models is the difference between mesh sizes. In the coarse mesh model the field travels a shorter distance to reach the same point than in the fine-mesh model. Therefore an additional time delay equivalent to the field travelling the distance of the mesh size difference is added to the phase extracted from the coarse mesh model. After such a phase compensation process, the two models are expected to produce the same phase at

the same distance from the equivalent dipole model. The phase calibration method can be described by Equation 3.6:

$$\emptyset_{cal} = \emptyset_{OP} - \emptyset_{ref} + \emptyset_{cell\ diff} \qquad (3.6)$$

Where $\emptyset_{cal}$ is the phase after calibration; $\emptyset_{OP}$ is the phase at the output point in the aperture model; $\emptyset_{ref}$ is the phase at the reference point and $\emptyset_{cell\ diff}$ is the phase shift induced by the difference in mesh size. After calibration, the phases of the two models are referenced to the same point, while the phase difference generated by the mesh size change is accounted for.

Figure 3.15 shows the fine-grid and coarse-grid models used for the phase calibration. The simulation volume is kept empty, and a plane wave is excited through a box with Huygen's surface support. The resulting phase is plotted against frequency.

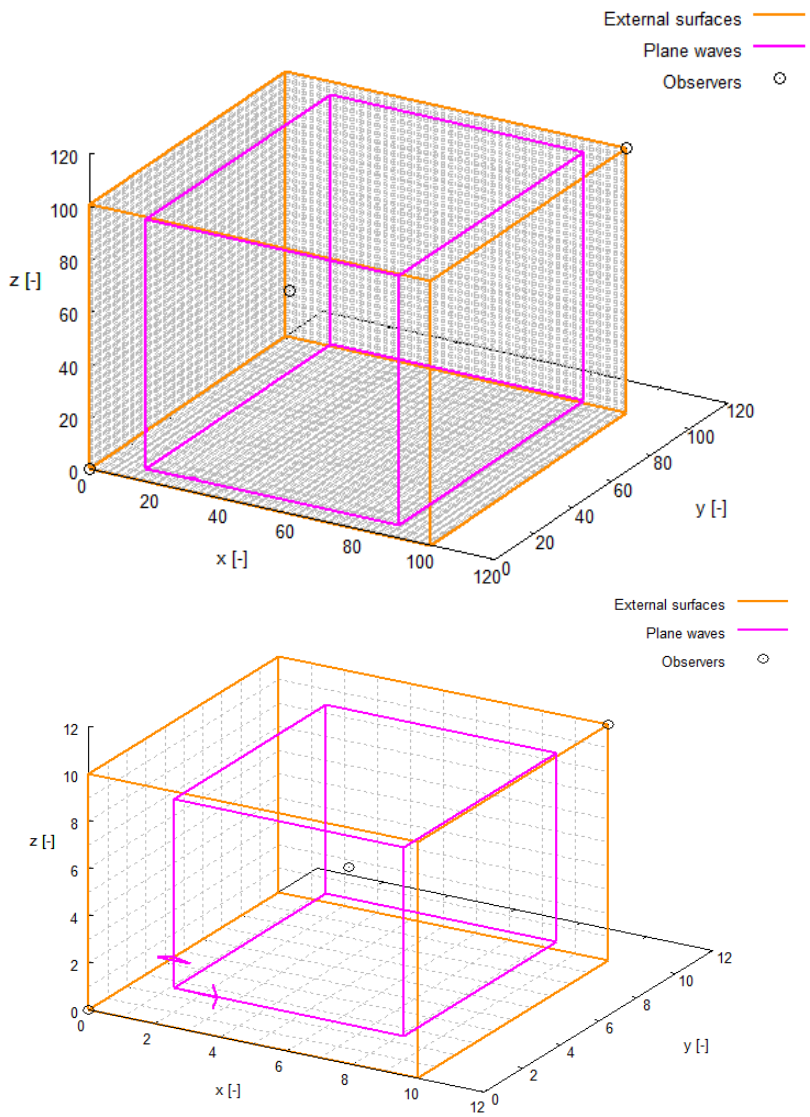

Figure 3.15 Phase calibration models in fine-grid (upper) and coarse-grid (lower)

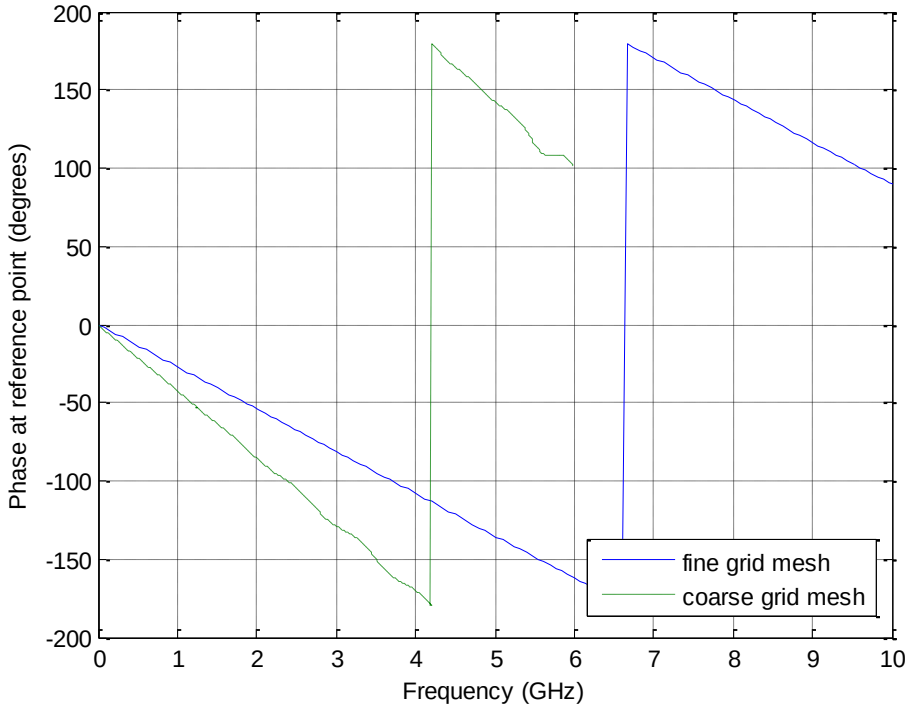

Figure 3.16 Frequency domain phase at reference points

It can be clearly observed that the phases of the two models are different at the reference point. The difference of the rates that the phases vary indicates that the fields in these models travelled different distances before reaching the reference points.

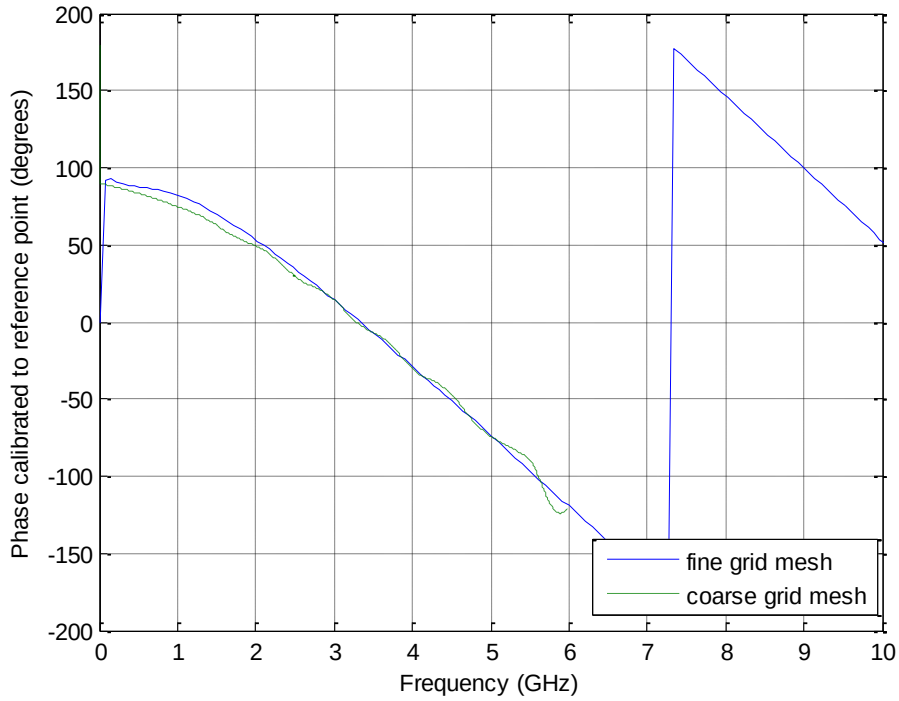

Figure 3.17 Calibrated phases of coarse grid and fine-grid models

In Figure 3.17, after calibration, the phases produced by the two models are within 10 degrees of each other after calibration. Section 3.5 and Section 3.6 has shown that the FDTD equivalent magnetic dipole implementation can not only produce accurate results in both magnitude and phase, but also works in both fine-grid and sub-cellular simulations.

3.6.2. Coordinate change due to mesh size variation

Figure 3.1 shows the structure of the field storage of a FDTD mesh. The field components are calculated and stored at different places on the mesh. The magnetic fields are calculated in the centres of mesh surfaces, while the electric fields are calculated on the edges. Therefore, there is a spatial separation of half a mesh size in-between the electric field and magnetic field. Figure 3.18 was produced according to the definition of FDTD meshes in Vulture [43]. E_{z0} and H_{y0} represent the excitation fields of the model and E_{z1} and H_{y1} represent the field at an observation point 2 coarse meshes, or 20 fine-meshes from the model. During the transformation between fine- and coarse-grid meshes in this modelling work, the aim was to locate the mesh of the fine-grid simulation in the centre of the surface of the coarse mesh, which is normal to the propagation direction of the field, while keeping identical relative distances between the excitation and output electric fields.

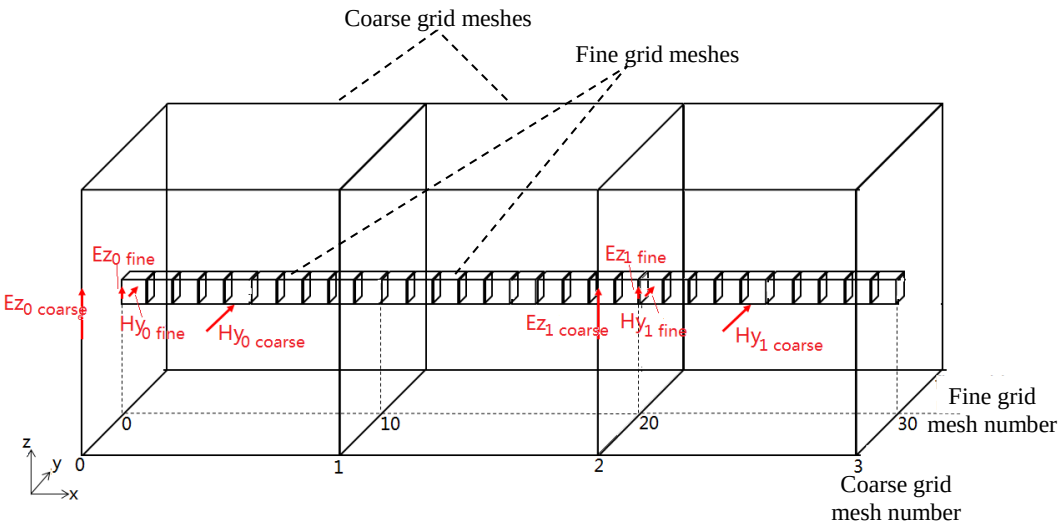

Figure 3.18 Locations of coarse- and fine-grid mesh field components

Figure 3.18 shows that fields propagated a distance in a fine-grid model are at different locations from those simulated using a coarse-grid model with the same propagation distance. In Figure 3.18, $E_{z0\ coarse}$ is the *z*-polarised electric field stored in the coarse-grid mesh number 0, while $H_{y0\ coarse}$ is the *y*-polarised magnetic field in the same mesh. $E_{z0\ fine}$ and $H_{y0\ fine}$ are those fields stored in the fine-grid mesh number 0. The

coarse-grid mesh is ten times the size of the fine-grid mesh. Therefore the field propagated the distance of 20 fine-grid mesh size corresponds to that of 2 coarse-grid mesh size. $E_{z1\ coarse}$ and $H_{y0\ coarse}$ are the *z*-polarised electric field and *y*-polarised magnetic field stored in the coarse-grid mesh number 2, while $E_{z0\ fine}$ and $H_{y0\ fine}$ are those fields stored in the fine-grid mesh number 20 Seen in Figure 3.18, it is clear that the locations of both H_{y0} and E_{z0} are different for fine-grid and coarse-grid meshes. Compared to the location H_{y0} in the fine-grid model, it is moved to the lower side of the*y*-axis and the higher side of the *x*-axis in the coarse-grid model; while the location of E_{Z0} is moved to the lower side of the y-axis. The amount of displacement is the difference of a half-mesh size between the grids. In addition, the observation point of the coarse grid mesh is sampled at a different point of the wave front than that of the fine-grid mesh. In the GA fittings, these displacements between meshes must be taken into account.

3.7. Utilising the dipole model with the frequency-dependent DIGIFILT module

DIGIFILT is another module used as part of the HIRF-SE project. The DIGIFILT module in Vulture is programed by Dr Ian Flintoft in the Physical Layer Research Group at the University of York. It is used to simulate homogeneous materials by equivalent surface impedances. In DIGIFILT, materials are represented with an equivalent surface impedance matrix to represent the material's transmission and reflection characteristics to the tangential fields. The relationship between the fields on two sides of the material and the impedance matrix is shown in Equation 3.7:

$$\begin{bmatrix} \boldsymbol{E_a}^{\boldsymbol{TM}}(\boldsymbol{\omega}) \\ \boldsymbol{E_b}^{\boldsymbol{TM}}(\boldsymbol{\omega}) \\ \boldsymbol{E_a}^{\boldsymbol{TE}}(\boldsymbol{\omega}) \\ \boldsymbol{E_b}^{\boldsymbol{TE}}(\boldsymbol{\omega}) \end{bmatrix} = \begin{bmatrix} \boldsymbol{Z_{aa}}^{\boldsymbol{TM}}(\boldsymbol{\omega}) & \boldsymbol{Z_{ab}}^{\boldsymbol{TM}}(\boldsymbol{\omega}) & \mathbf{0} & \mathbf{0} \\ \boldsymbol{Z_{ba}}^{\boldsymbol{TM}}(\boldsymbol{\omega}) & \boldsymbol{Z_{bb}}^{\boldsymbol{TM}}(\boldsymbol{\omega}) & \mathbf{0} & \mathbf{0} \\ \mathbf{0} & \mathbf{0} & \boldsymbol{Z_{aa}}^{\boldsymbol{TE}}(\boldsymbol{\omega}) & \boldsymbol{Z_{ab}}^{\boldsymbol{TE}}(\boldsymbol{\omega}) \\ \mathbf{0} & \mathbf{0} & \boldsymbol{Z_{ba}}^{\boldsymbol{TE}}(\boldsymbol{\omega}) & \boldsymbol{Z_{bb}}^{\boldsymbol{TE}}(\boldsymbol{\omega}) \end{bmatrix} \begin{bmatrix} \boldsymbol{H_a}^{\boldsymbol{TM}}(\boldsymbol{\omega}) \\ -\boldsymbol{H_b}^{\boldsymbol{TM}}(\boldsymbol{\omega}) \\ \boldsymbol{H_a}^{\boldsymbol{TE}}(\boldsymbol{\omega}) \\ -\boldsymbol{H_b}^{\boldsymbol{TE}}(\boldsymbol{\omega}) \end{bmatrix} = \boldsymbol{Z}(\boldsymbol{\omega}) \begin{bmatrix} \boldsymbol{H_a}^{\boldsymbol{TM}}(\boldsymbol{\omega}) \\ -\boldsymbol{H_b}^{\boldsymbol{TM}}(\boldsymbol{\omega}) \\ \boldsymbol{H_a}^{\boldsymbol{TE}}(\boldsymbol{\omega}) \\ -\boldsymbol{H_b}^{\boldsymbol{TE}}(\boldsymbol{\omega}) \end{bmatrix} \quad \textbf{(3.7)}$$

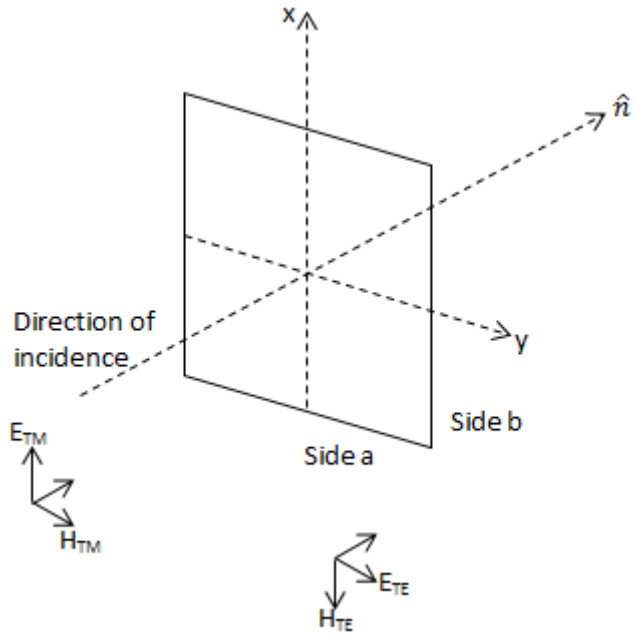

Figure 3.19 Definition of impedance matrix, wave modes and direction of incidence

Where *a* and *b* represent the incident and transmission sides of the material, respectively; *Z* terms are the surface impedances; TM and TE are transverse magnetic and transverse electric modes of the wave, respectively. Based on these impedances, the material is modelled as a digital filter with frequency-dependent characteristics. The filter can be configured as a first-order filter or with a higher order so that a more complicated frequency response may be produced. In macroscopic scale, it can be used to model an electrically small aperture as an aperture has a high-pass response in the frequency domain. Compared to the dipole moment equivalent model introduced previously, its frequency-dependent characteristic could give DIGIFILT more flexibility and accuracy when applied to complex structures. However, the surface impedance technique does not calculate the normal field components as shown in Figure 3.19. For example, the transmission and reflection relationships of an *x*-polarised TM wave are calculated by Equation 3.8:

$$\begin{bmatrix} \boldsymbol{E_x^a} \\ \boldsymbol{E_y^b} \end{bmatrix} = \begin{bmatrix} \boldsymbol{Z_{aa}(\omega)} & \boldsymbol{Z_{ab}(\omega)} \\ \boldsymbol{Z_{bb}(\omega)} & \boldsymbol{Z_{ba}(\omega)} \end{bmatrix} \begin{bmatrix} \boldsymbol{H_x^a} \\ \boldsymbol{-H_y^b} \end{bmatrix} \tag{3.8}$$

The resulting field is then added to the FDTD updated field in the absence of the model. Therefore, similar to the equivalent dipole moment model discussed previously, the DIGIFILT model is also built in as a soft field source.

The impedances, as seen in Equation 3.7 and Equation 3.8, are frequency-dependent parameters. In our case, only the transfer impedance Z_{ab} was considered. The transfer impedance was calculated using Equation 3.9:

$$\boldsymbol{Z_{ab}{}^{TM}(\omega) = Z_{ab}{}^{TM;\infty} + \sum_{q=1}^{N_P^{TM}} \frac{r_q^{TM}}{j\omega - p_q^{TM}}} \qquad \textbf{(3.9)}$$

Where N is the order of the filter, $Z^{\infty}$is the high frequency asymptotic response, and r and p are the filter residuals and poles respectively. The number of poles and residuals depends on the order of the filter. The higher order the filter, the more complicated frequency response of the material could be reproduced, however more computational effort would be needed to find those parameters.

For an electrically small aperture, polarisability is considered to be a constant against frequency, and the following relationship between filter parameters and polarisability has been derived:

$$\boldsymbol{Z_{ba}(\omega) = j\omega\mu_0 \frac{\alpha_M(\omega)}{\Delta x \Delta y}} \qquad \textbf{(3.10)}$$

Where Δx and Δy are the size of the FDTD mesh along x and y axes respectively. Let

$$\boldsymbol{Z_{ba}(\omega) = j\omega M} \qquad \textbf{(3.11)}$$

$$\boldsymbol{M = \mu_0 \frac{\alpha_M(\omega \to 0)}{\Delta x \Delta y}} \qquad \textbf{(3.12)}$$

For a first-order system, at low frequencies, the transfer impedance is:

$$\boldsymbol{Z_1(s = j\omega) = 1 + \frac{p_1}{s - p_1} \xrightarrow[\omega=0]{} -\frac{s}{p_1}} \qquad \textbf{(3.13)}$$

In Equation 3.13, p_1 represents the high-pass cut-off frequency, where $\omega_1 = p_1$ and $r_1 = p_1$. The validation tests of the DIGIFILT application are restricted as first-order filters.

In order to apply the GA to fit DIGIFILT parameters, the relationship between the equivalent magnetic dipole moment and the filter transfer impedance needs to be derived as below:

$$\boldsymbol{Z_{ba}(\omega) = j\omega\mu_0 \frac{\alpha_M(\omega)}{\Delta x \Delta y} = Z_{ba}{}^{\infty} + \sum_{q=1}^{N_P} \frac{r_q}{j\omega - p_q}} \qquad \textbf{(3.14)}$$

The magnetic dipole moment is formed by the short-circuited magnetic field and polarisability as mentioned in Section 1.5.1:

$$\boldsymbol{m = \alpha_M H_{sc}} \tag{3.15}$$

Therefore:

$$\boldsymbol{\alpha_M = \frac{m}{H_{sc}}} \tag{3.16}$$

$$\boldsymbol{Z_{ba}(\omega) = j\omega\mu_0 \frac{m/H_{sc}}{\Delta x \Delta y} = Z_{ba}{}^{\infty} + \sum_{q=1}^{N_P} \frac{r_q}{j\omega - p_q}} \tag{3.17}$$

Moving terms:

$$\boldsymbol{m = \frac{H_{sc}\Delta x \Delta y}{j\omega\mu_0}\left[Z_{ba}{}^{\infty} + \sum_{q=1}^{N_P} \frac{r_q}{j\omega - p_q}\right]} \tag{3.18}$$

The magnitude of residuals and poles are in the order of 10^9 to 10^{12}, and such a search domain is too large for the GA to operate effectively if the residuals and poles are searched directly in real and imaginary parts. Therefore, instead of searching the residuals and poles directly, the search is performed in logarithmic values and phases, so the residuals and poles are constructed as:

$$\boldsymbol{r = 10^{r_{log}} \cdot \exp(jr_\varphi)\ ,\ \ p = 10^{p_{log}} \cdot \exp(jp_\varphi)} \tag{3.19}$$

Where r_{log} and p_{log} are the logarithmics of r and p, and r_φ and p_φ are the phase terms. The filter parameters are then used to calculate the magnetic dipole moment, followed by the calculation of the radiated field from the dipole and the cost function. The design parameters are frequency-dependent and the search is carried out at multiple frequency points. As shown in Equation 3.18, the dipole moment is frequency-dependent as well. Therefore, the dipole moment is calculated at each frequency in the search, and so is the radiated field from it. The cost function is the mean-error cost function that was used by the GA previously, but summed across the frequencies in the search.

$$\boldsymbol{C = \sum_{f=f_1}^{f_{max}} \frac{1}{XY} \sum_{x=1}^{X} \sum_{y=1}^{Y} |E_{GA} - E_{FDTD}|} \tag{3.20}$$

The modified GA was used to fit first-order DIGIFILT parameters for the small aperture model shown below. The radiated field was generated in a fine-grid FDTD model using mesh size 0.5 mm. The square aperture was 3×3 meshes, thus 1.5×1.5 mm in size. The fit used electric field output from a 100×100 mm plane which was 130 mm

from the aperture. The fields used for fitting were taken at 1.5 and 2.5 GHz. The GA was run for 300 generations, and the result passed to a descent optimiser for faster descent towards the bottom of the error surface. The fitted poles and residuals were then applied to a DIGIFILT FDTD model with a mesh size of 1cm.

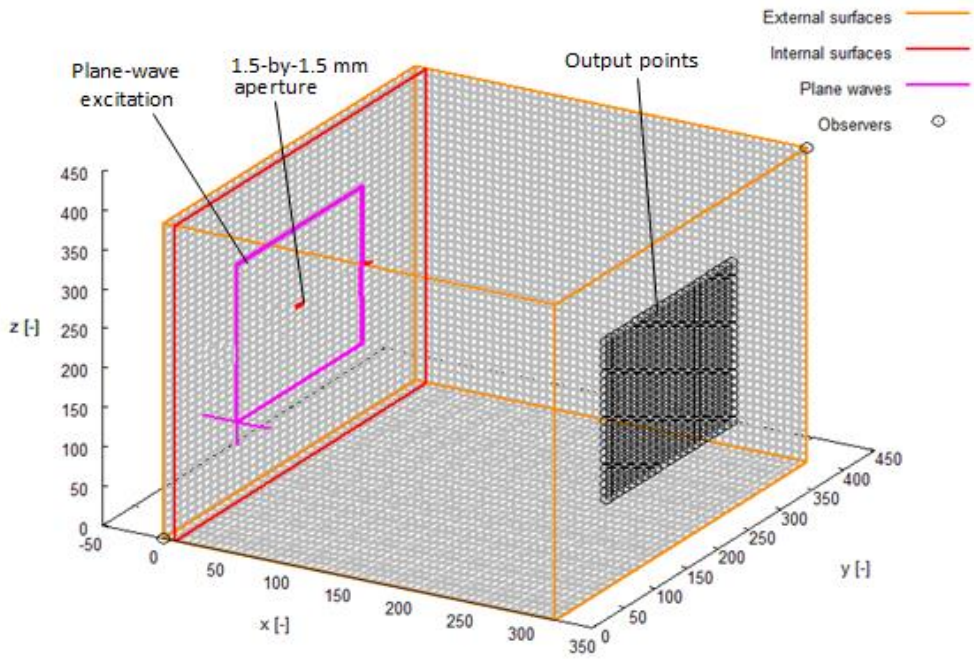

Figure 3.20 Fine-grid FDTD model of a 1.5-by1.5 mm square aperture

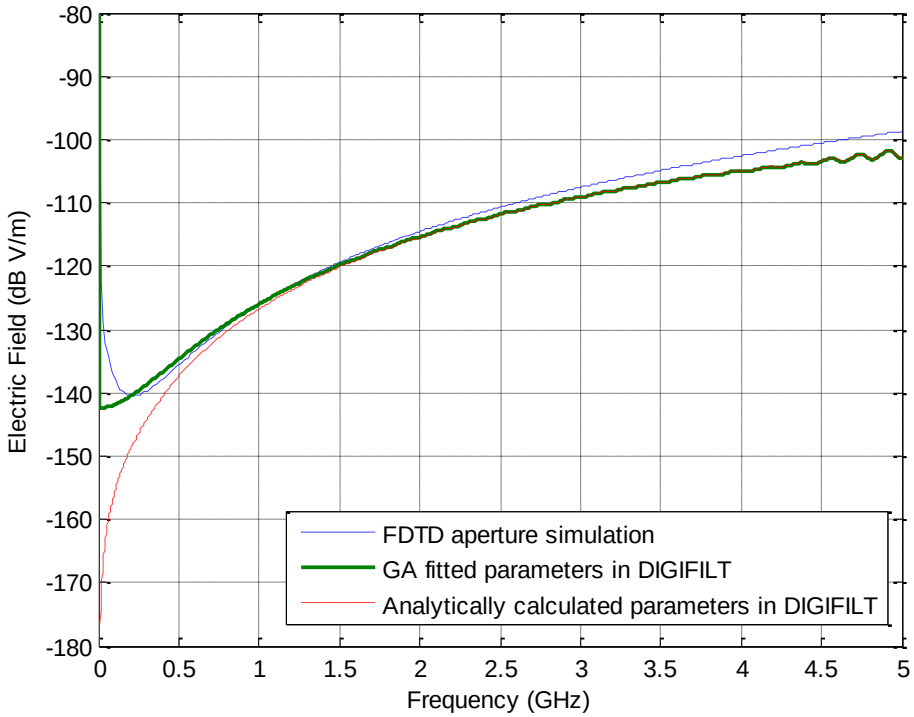

Figure 3.21 Frequency domain response of small aperture by simulation and analytic calculations

Figure 3.21 shows the frequency domain electric field intensity of the fine-grid aperture model and coarse-grid DIGIFILT equivalent model. Since the DIGIFILT model had a larger mesh size than that used in the aperture simulation, the upper frequency that it is capable of simulating was reduced significantly. In addition, it was also shown that the two results agree well at the frequencies between which the fit was performed, but their low frequency behaviours were significantly different. It was found that the result was sensitive to the difference between *p* and *r*. In Figure 3.22 and Figure 3.23, where the poles and residuals are tuned manually, a difference of 1% between poles and residuals will results in distortion at low frequencies. In Figure 3.22, *p*=1.9644e11 shares the same result as *p*=9844e11, while the same results are observed for *p*=1.9444e11 and *p*=2.0044e11. The same effects are seen in Figure 3.23 also. In this first-order model, tuning *p* and tuning *r* had the same effect on the frequency response. This may be due to the fact that at low frequencies, the difference between *p* and *r* dominates the behaviour of the filter.

For a first-order model, the transfer impedance is:

$$\boldsymbol{Z = 1 + \frac{r}{j\omega - p}} \tag{3.21}$$

If the difference between *p* and *r* is represented by the factor *d*, the equation is written as below. At low frequencies, the formation of the transfer impedance depends on *d* and *p*:

$$\boldsymbol{Z = 1 + \frac{p+d}{j\omega - p}} \tag{3.22}$$

$$\boldsymbol{Z = \frac{j\omega - p + p + d}{j\omega - p} \xrightarrow[\omega=0]{} -\frac{d}{p}} \tag{3.23}$$

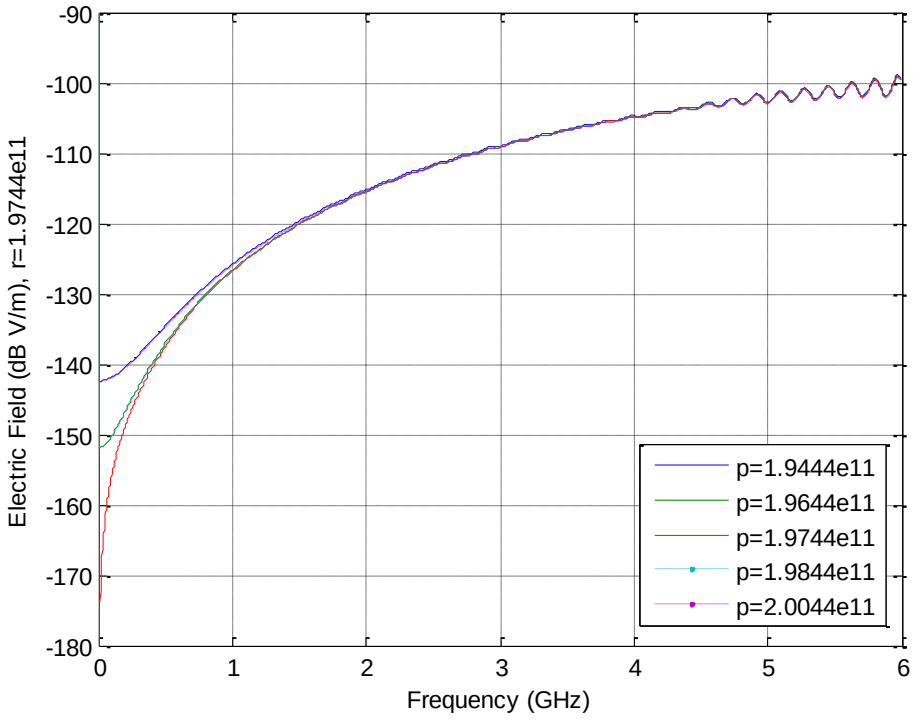

Figure 3.22 DIGIFILT single aperture simulation output with *r* = 1.97e11 and varying *p*

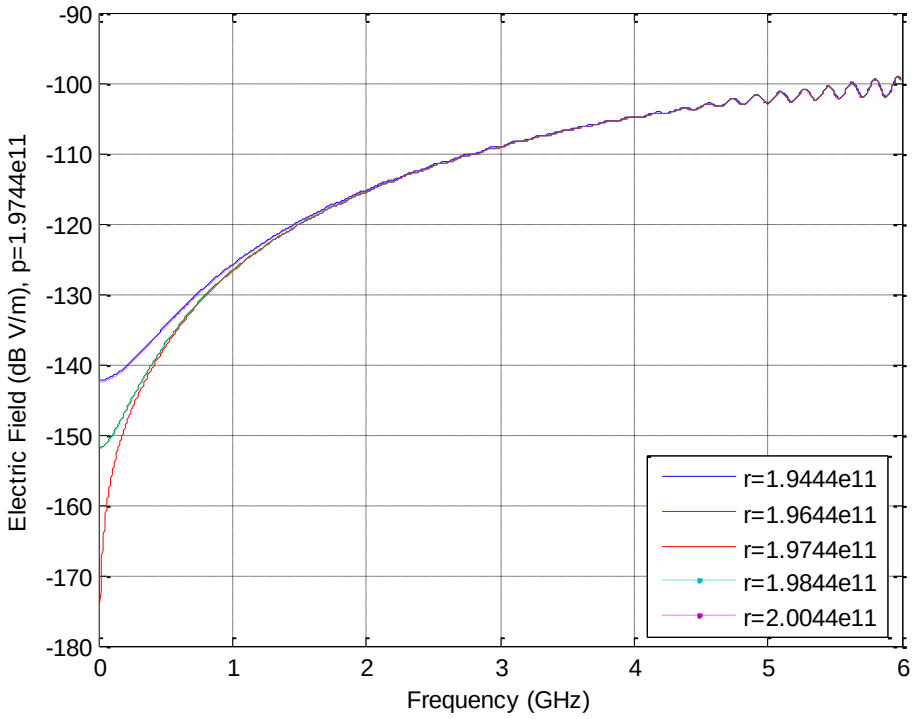

Figure 3.23 DIGIFILT single aperture simulation output with *p* = 1.97e11 and varying *r*

3.8. Summary

A method that calculates the magnetisation of the equivalent magnetic dipole moment was employed to model electrically small apertures in FDTD simulations. It calculated the magnetisation using the short-circuited magnetic field on the incident side of the aperture and the aperture polarisability. The radiated field was then added to the FDTD grid as a soft field source. In this way, the magnetic field was instantaneously forwarded spatially by one mesh size. As a result, a phase correction procedure was developed to calibrate the field to a reference point in order for the results produced by fine-grid and coarse-grid simulations to be comparable. The method employed could reproduce the field radiated by a small square aperture simulated in FDTD in both fine- and coarse-grid simulations. However, the upper frequency limit and spatial resolution was reduced in the coarse-grid simulation, where the model was macroscopic; the field that the macro model produced was within 2 dB of that of the fine-grid model. The phase result was also accurate after the correction procedure. The error was smaller than 10 degrees.

The DIGIFILT module was introduced in this chapter. The transfer characteristic of the object was modelled using a transfer and reflection impedance matrix. The impedances were formed by a series of poles and residuals of the equivalent digital filter. A first-order example of modelling a 1.5mm aperture using 1cm meshes demonstrated that the DIGIFILT can model small apertures in a FDTD mesh much larger than the aperture itself. It was also found that this first-order approach requires poles and residuals to have the same values so that the low frequency behaviour follows that of the analytic solutions. Further investigations are needed to fit higher order filters for small apertures and apertures comparable to mesh size.

Chapter 4. Measurement Devices Development

A measurement system was constructed to perform near-field measurement and provide experimental data as the input to the GA and for the validation of the modelling results. The measurement system consisted of an absorber box and the excitation antenna to provide illumination to the structure being modelled, small antennas as field probes, and a 3-D scanner to locate the antennas for a planar near-field scan. This chapter introduces these measurement devices and present some results measured using this measurement system.

Firstly, the absorber box and its principle are introduced. Then the designs of a dipole antenna as an electric field probe, and a loop as a magnetic field probe are presented, followed by their characterisation measurement results. After that, the 3-D scanner is introduced. The measurement system was used to measure field penetrating slot samples and the measurement results are discussed.

4.1. The absorber box

The absorber box, developed by the Electronics Department Physical Layer Research Group at the University of York [43], was designed to create an environment close to free-space for measuring the shielding-effectiveness of a given material. Figure 4.1 shows the cross-sectional and top views of the absorber box. A horn antenna sits at the bottom of a cavity that is surrounded by a number of layers of LS22 and AN79 absorber. The horn antenna is used as the excitation source for measuring the objects that are placed on top of the absorbers. The box was designed so that the excitation fields are absorbed when reaching the absorbers so the environment in the cavity is like free space for a wave propagating into it. Normally, measuring shielding effectiveness of a material sheet in an anechoic chamber requires edge treatment of the material sheet to avoid field diffracted and propagated around the edge causing measurement inaccuracy. The absorber box allows the measurement of the material sheet to be carried out in a smaller room and without the complex edge treatment of the sheet. In this research program, the absorber box is used as an excitation method to provide the fields illuminating the slot samples.

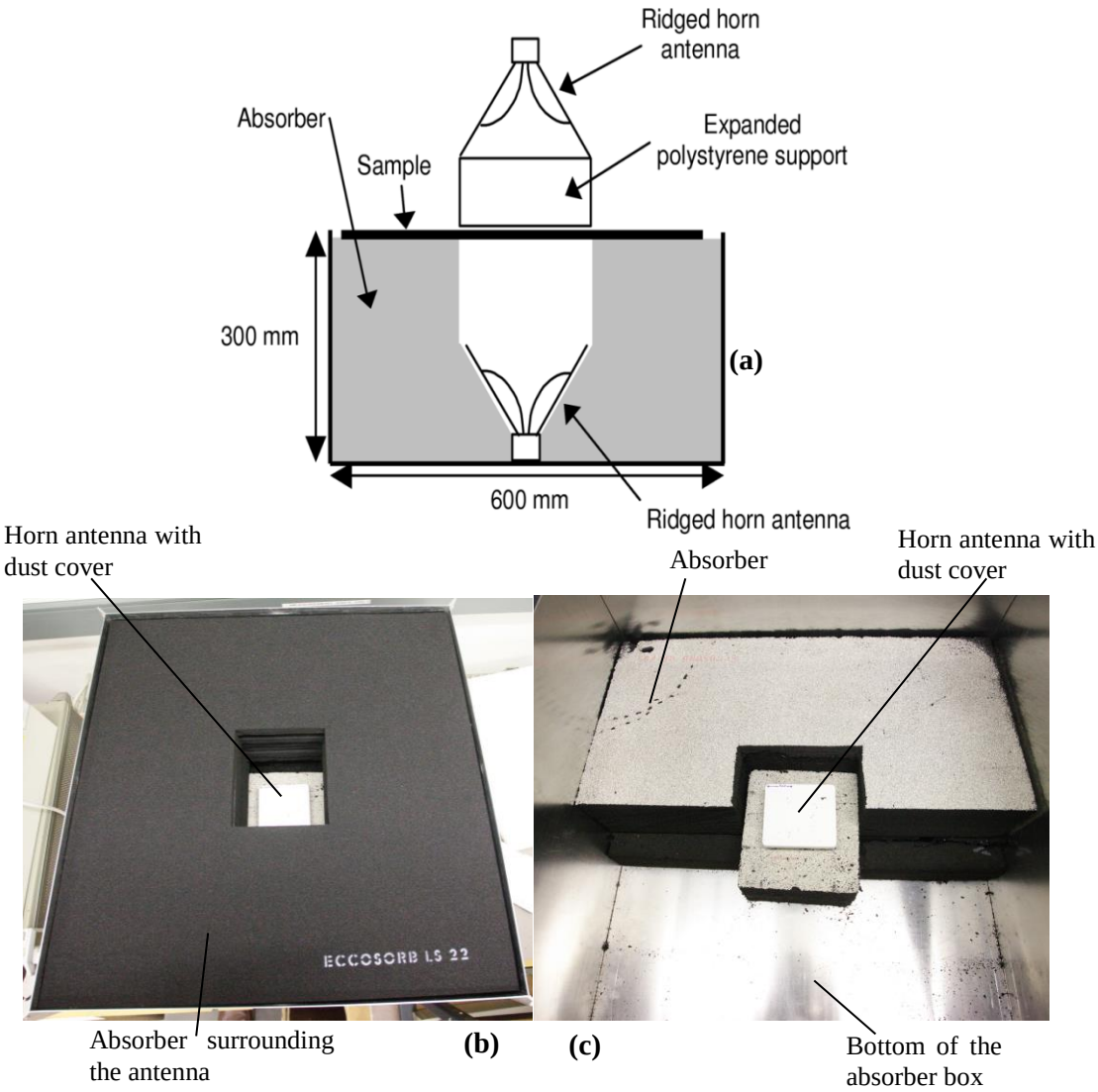

Figure 4.1(a) Cross-sectional view of the absorber box, (b) top view of the abosorber box, (c) absorber box with half of the absorber removed, showing the antenna buried in the absorber

4.2. Near-field probes

Electrically small antennas were built as near-field probes. A small dipole with a differential amplifier as a BALUN was designed as the electric field probe, and a small loop was designed as the magnetic field probe.

4.2.1. Small dipole design

The size of the dipole must be big enough to make the measurement above the noise floor, but not too big to disturb the near-field by the interaction between the dipole and the metal sheet being measured. The dipole was designed by Marschke [48], and as shown in Figure 4.2, it was built on a printed circuit board to minimise its size, hence reducing interference to the field being measured. The dipole head was sized 10mm,

followed by a 50 mm transmission line connecting the head and an ADL5562 differential amplifier, which acts as a BALUN. The two legs of the dipole produce balanced differential signals which act against each other. To produce an output from the dipole, the phase of one of the signals needs to be shifted by 180 degrees before adding them together. A BALUN, in this case the amplifier, performs such phase shift and then the summation of the signals. The amplifier took a 3.3V DC power supply, with the connector mounted next to the SMA connector on the other side of the substrate, opposite to the dipole head.

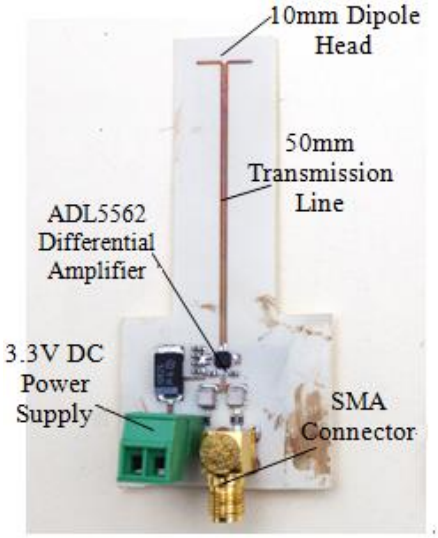

Figure 4.2 Dipole antenna design, photo taken by Ran Xia [48]

The balance, the cross-polar rejection and the sensitivity of the dipole were measured in the anechoic chamber. An EMCO3115 riged horn antenna was used as the excitation source. The dipole was placed 67 cm from the horn antenna, and was taped onto a wooden stand aligning the dipole to the centre of the excitation antenna. The balance and the cross-polar characteristic of the dipole were tested by rotating the horn antenna. In the set up shown in Figure 4.3, the dipole is receiving the co-polar electric field. A cross-polar excitation could be produced by rotating the horn antenna by 90 degrees. The phase balance of the dipole was tested by rotating the horn antenna by 180 degrees from the orientation shown in Figure 4.3 and observing if a phase difference of 180 degrees was produced in the output of the dipole.

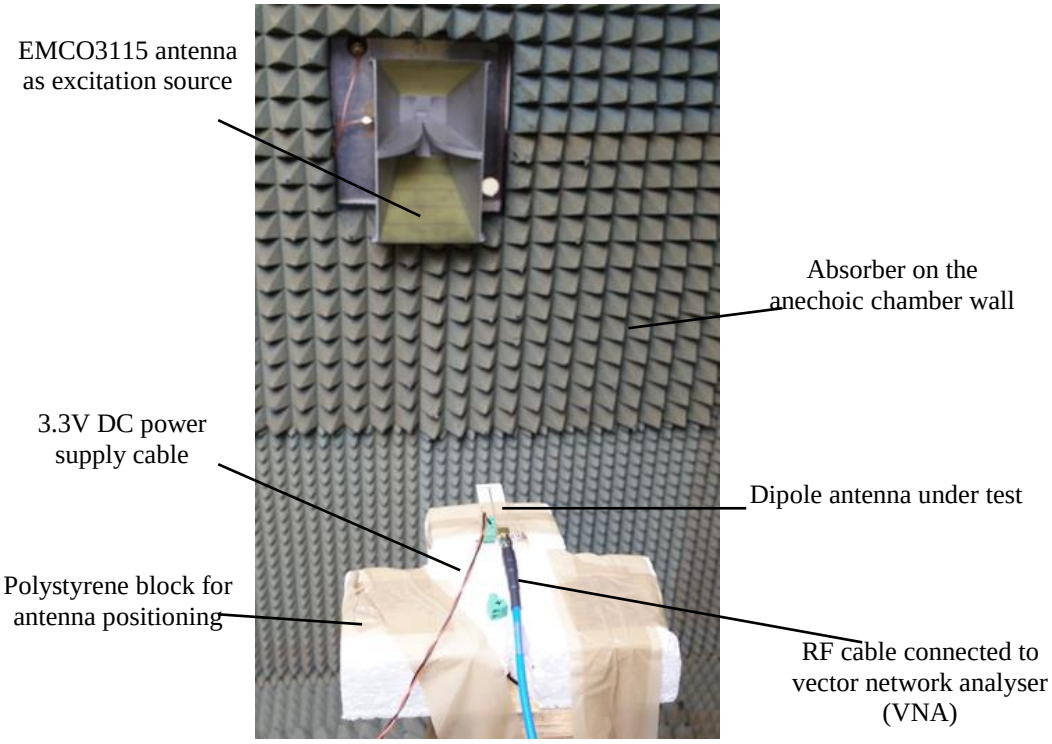

Figure 4.3 Anechoic chamber set up for testing the dipole antenna

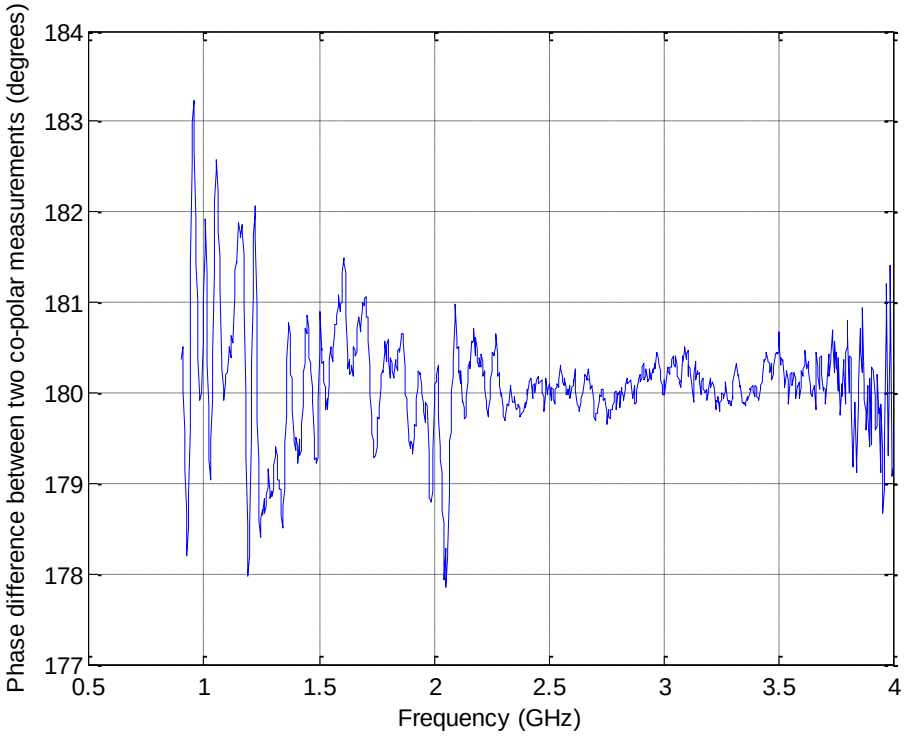

Figure 4.4 Phase balance test result of the dipole antenna

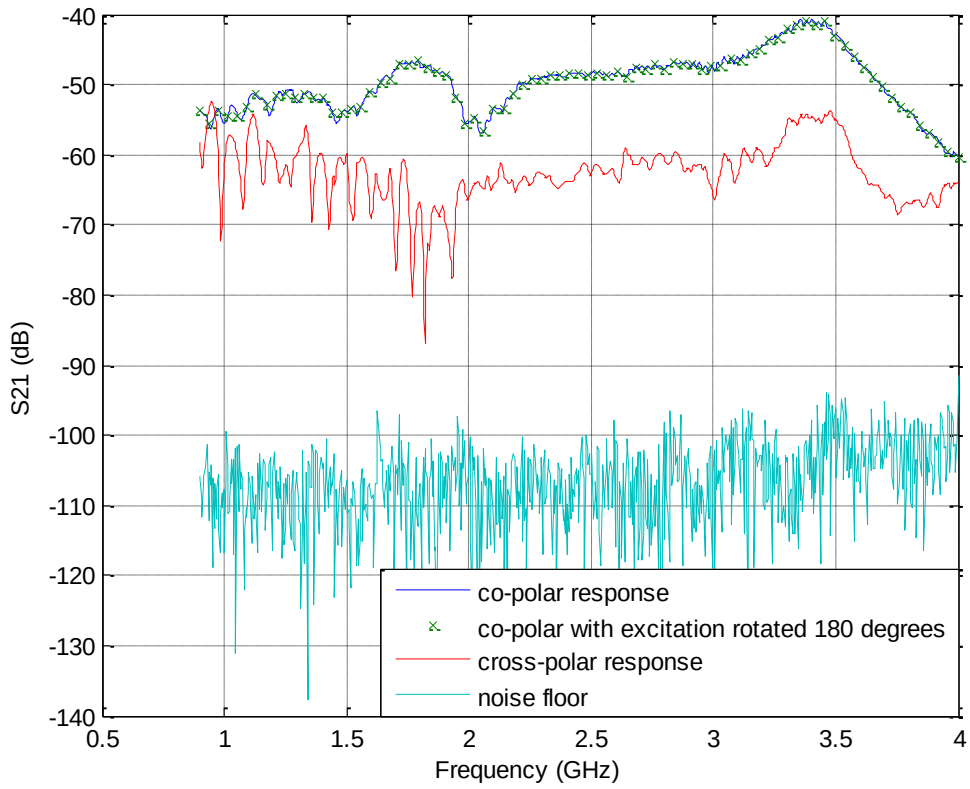

Figure 4.5 Cross-polar rejection test result of the dipole antenna

Figure 4.4 and Figure 4.5 show the measurement results of balance and cross-polar characteristics of the dipole. When the excitation was flipped by 180 degrees, the phase of the field measured by the dipole was shifted by 180 degrees with errors of ±3 degrees, while the field amplitude measured stayed the same. The dipole was well balanced. In Figure 4.5, the measurement was well above the noise floor of the instruments. The co-polar response cleared the cross-polar response by 10 dB between 1.7 and 3.7 GHz.

The sensitivity of an antenna is characterised by the antenna factor (AF), which is defined as the ratio of the incident field and the voltage produced on the load of the antenna. The antenna factor of a dipole can be derived from its equivalent circuit and effective length, where the effective length is defined as the ratio of the open-circuit voltage at the antenna terminal and the incident field.

$$l_e = \frac{V_{oc}}{E_{inc}} \tag{4.1}$$

$$AF = \frac{E_{inc}}{V_L} \tag{4.2}$$

Where l_e is the effective length of the antenna, V_{oc} is the open-circuit voltage at the antenna terminal, E_{inc} is the incident electric field and V_L is the voltage across the load of the antenna.

The relationship between antenna factor and effective length is thus the voltage divider formed by the input impedance of the dipole and the load impedance. The dipole input impedance is calculated using the following equivalent circuit proposed by Tang [49]:

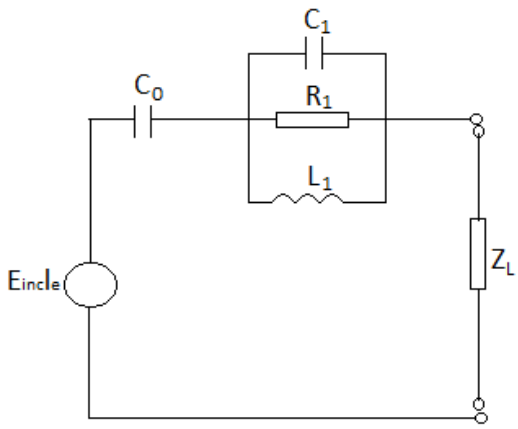

Figure 4.6 Equivalent circuit of a dipole antenna, reproduced from [49]

Where the voltage source represents V_{OC} in Equation 4.1, C_0 is the electrostatic capacitance of the dipole, R_1, C_1 and L_1 are the anti-resonance components, and Z_L is the load impedance. The input impedance of the dipole is then the combination of these components:

$$Z_d = \frac{sL_1R_1}{s^2C_1L_1R_1 + sL_1 + R_1} + \frac{1}{sC_0} \quad \textbf{(4.3)}$$

$$s = j\omega = 2\pi jf \quad \textbf{(4.4)}$$

The voltage developed on the load impedance is then:

$$V_L = E_{inc}l_e \frac{Z_L}{Z_d + Z_L} \quad \textbf{(4.5)}$$

The antenna factor, as it is defined, is:

$$AF = \frac{E_{inc}}{V_L} = \frac{Z_d + Z_L}{l_e Z_L} \quad \textbf{(4.6)}$$

The dipole effective length can be calculated as:

$$l_e = \frac{l\omega_0^2}{s^2 + 2\partial s + \omega_0^2} \quad \textbf{(4.7)}$$

Where l is the length of the dipole, ω_0 is the resonant frequency in radians, f is the frequency at which the effective length is calculated, ∂ is the damping frequency where

$$\partial = \frac{1}{C_0 R_1} \quad \textbf{(4.8)}$$

The detailed equations of calculations for each element in the equivalent circuit are given in Appendix III.

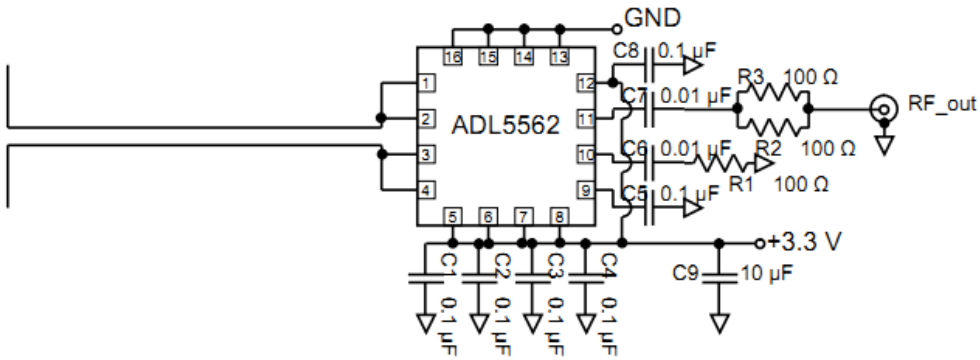

Figure 4.7 Circuit layout of the electric field probe

It is worth noting that the above equivalent circuit is for the dipole antenna only. As shown in Figure 4.7, in addition to the 1cm dipole, the probe contained a 5cm transmission line, a differential amplifier and two load resistors. The amplifier was configured to give a maximum available gain from it, which was 13.5 dB, only one of the differential outputs was connected to the instrument, which resulted in halving the output amplitude, hence reducing the output by 6 dB. The output resistors made an effective 50 Ω resistor connected in series with the measurement instrument, which has a 50 Ω characteristic impedance. This voltage divider halves the voltage reaching the output port again, which reduces the output further by 6 dB. In summary, the expected net gain produced by the system following the dipole antenna is the combination of the 13.5 dB amplifier gain, the 6 dB reduction induced by taking only of the differential amplifier outputs to the RF output, and another 6 dB reduction induced by the output resistors. The expected amplification of this circuit is 13.5 - 6 - 6 = 1.5 dB.

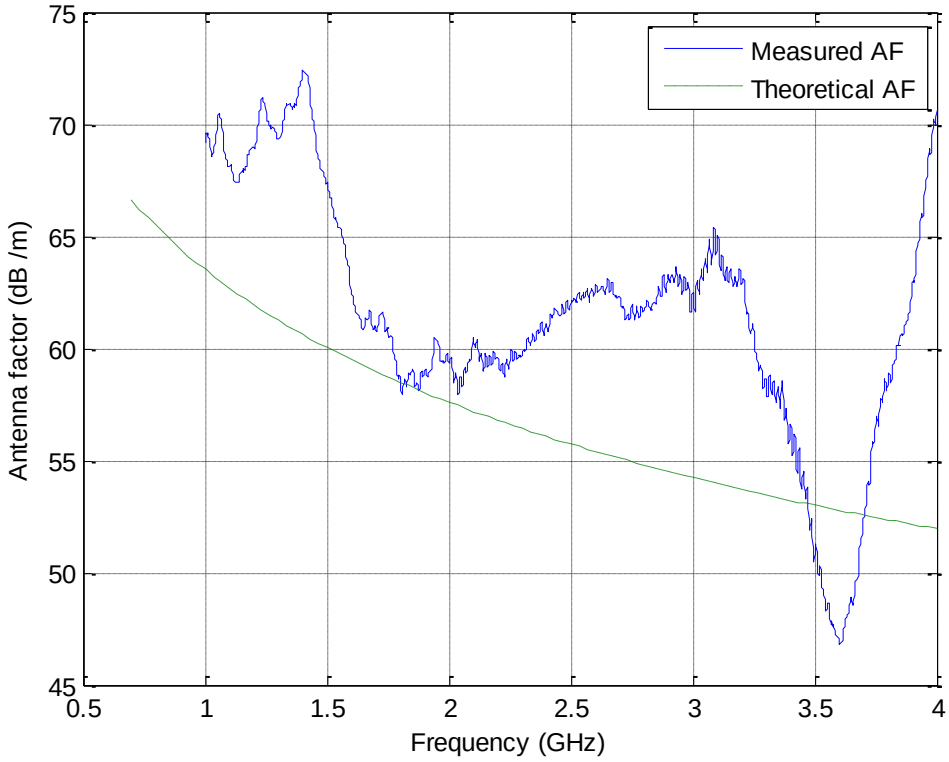

Figure 4.8 Measured and theoretical AF of the dipole antenna

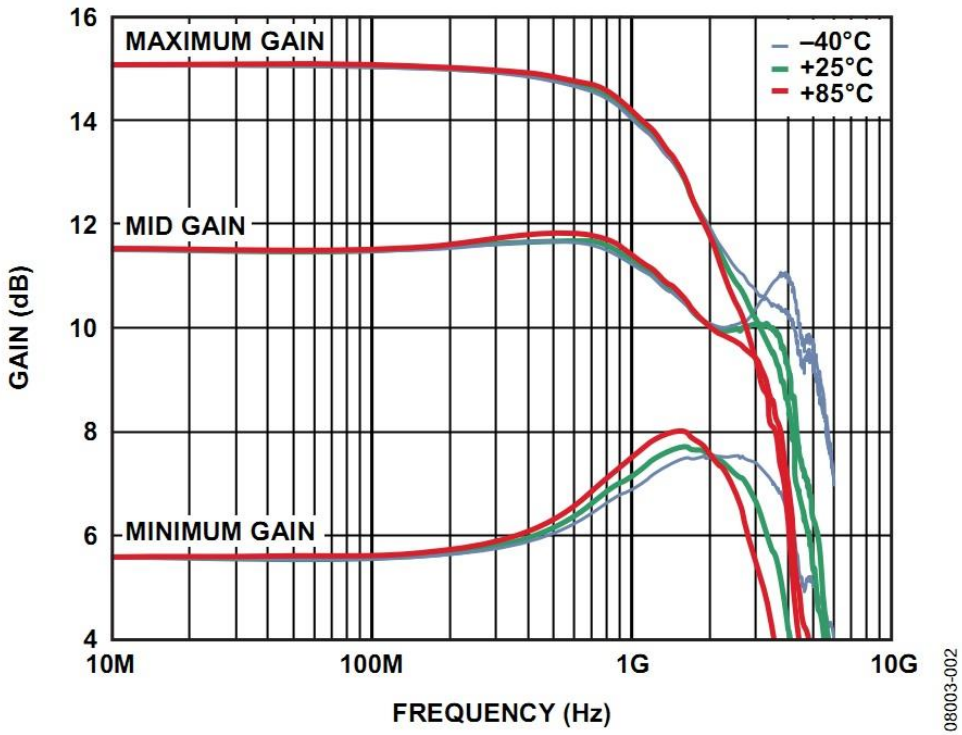

Figure 4.9 Frequency vs Gain characteristics of ADL5562 for 200 Ω differential load. Maximum gain =15.5dB, medium gain = 12dB and Minimum gain = 6dB [50]

In Figure 4.8, it can be seen the overall level of the measured antenna factor is 3dB higher than the calculation and the measured antenna factor is not a smooth curve across frequency. Figure 4.9 shows the frequency-gain characteristics of the amplifier obtained from the data sheet. It can be seen at the frequency band of the antenna factor measurement that the frequency-gain characteristic is not flat and is in fact decreasing from the maximum gain of the amplifier. Operating at the frequencies whereby the gain varies rapidly across frequency is considered to be the reason that the measured antenna factor does not produce a smooth curve.

4.2.2. Small loop design

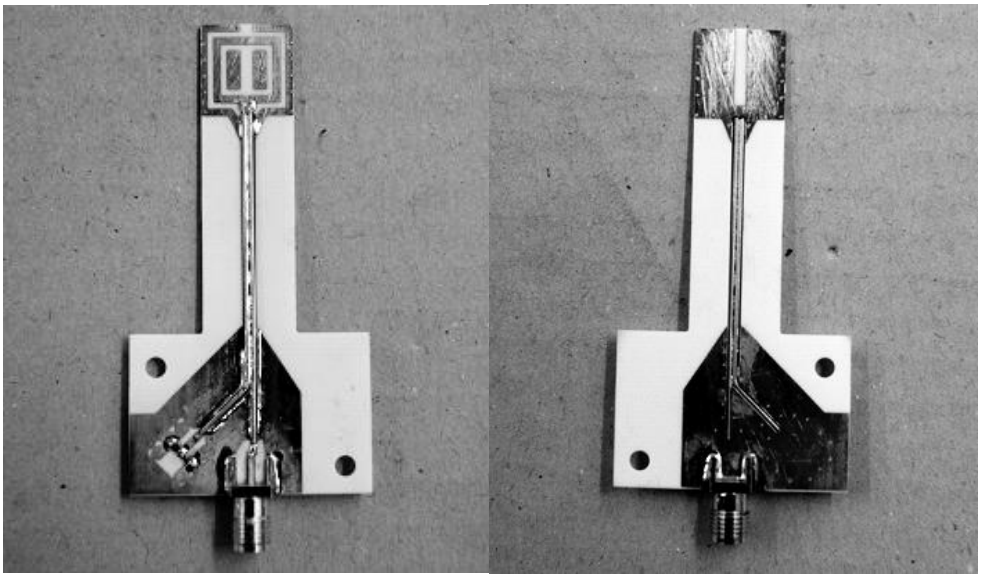

Figure 4.10 Front (left) and back (right) design of the loop antenna

Figure 4.10 shows the design of the loop antenna used to measure the magnetic field. Similar to the dipole, the loop was built on printed circuit board, with semi-rigid cables connecting one end to a 50 Ω load, and another to an SMA connector. The 50 Ω load was constructed using two 100 Ω surface-mount resistors to reduce inductance. To reduce error caused by the current induced by the electric field picked up, it is important to shield the loop against the electric field. As shown in Figure 4.10, there are two copper plates inside the loop to provide a shield against the electric field. In addition, a ground plane with air gap was also built on the back of the loop; with further shielding given by a loop with an air gap built outside the loop used to probe the magnetic field.

The loop was then tested for balance, cross-polar rejection and antenna factor in the anechoic chamber. The test parameters are the same as those of the measurements of the dipole.

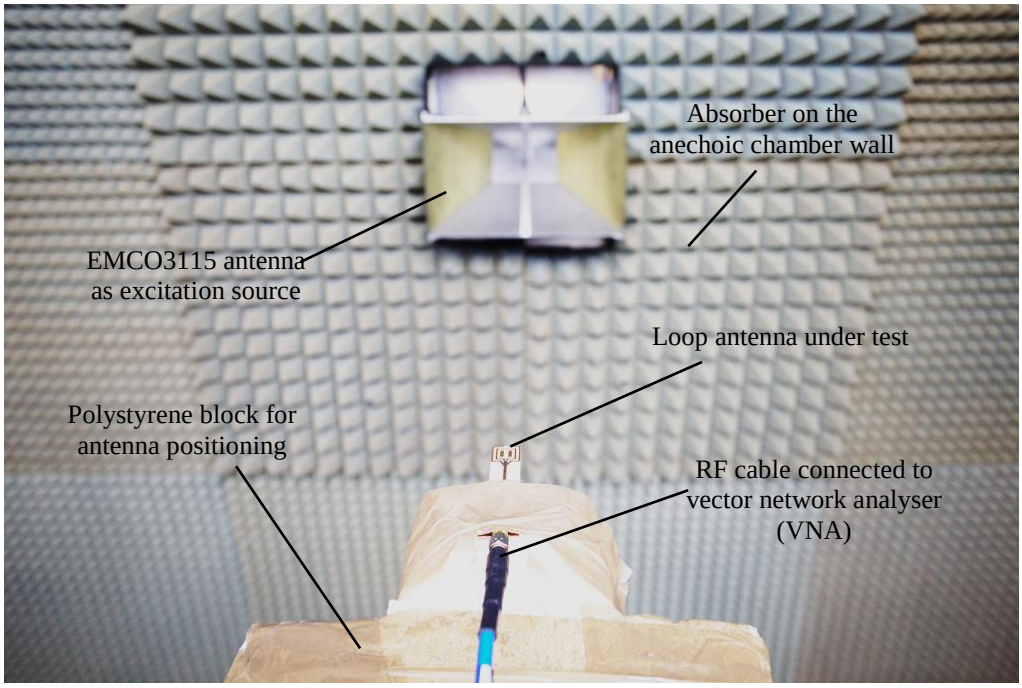

Figure 4.11 Loop under test in the anechoic chamber

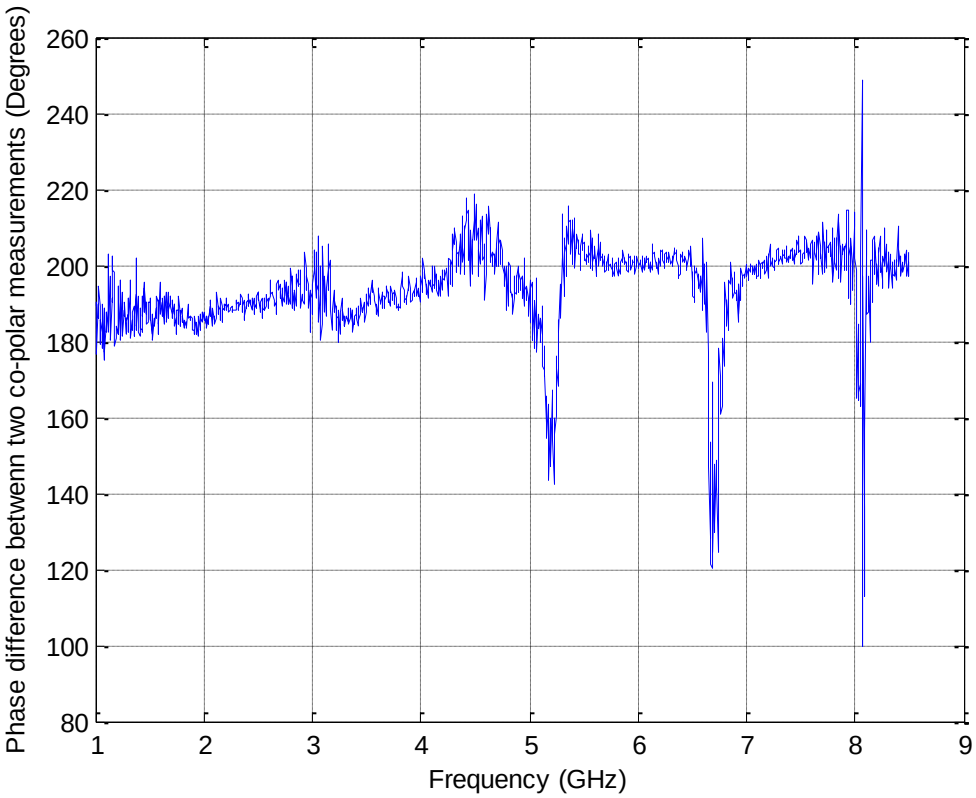

Figure 4.12 Phase balance test result of the loop antenna

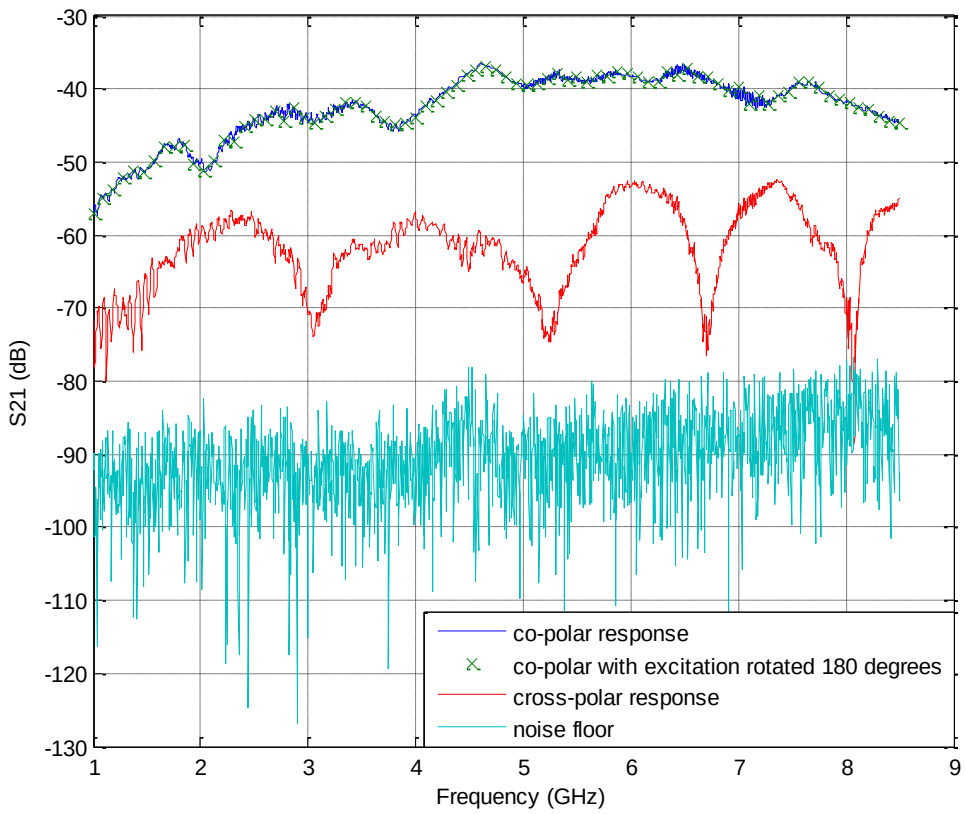

Figure 4.13 Cross-polar rejection test result of the loop antenna

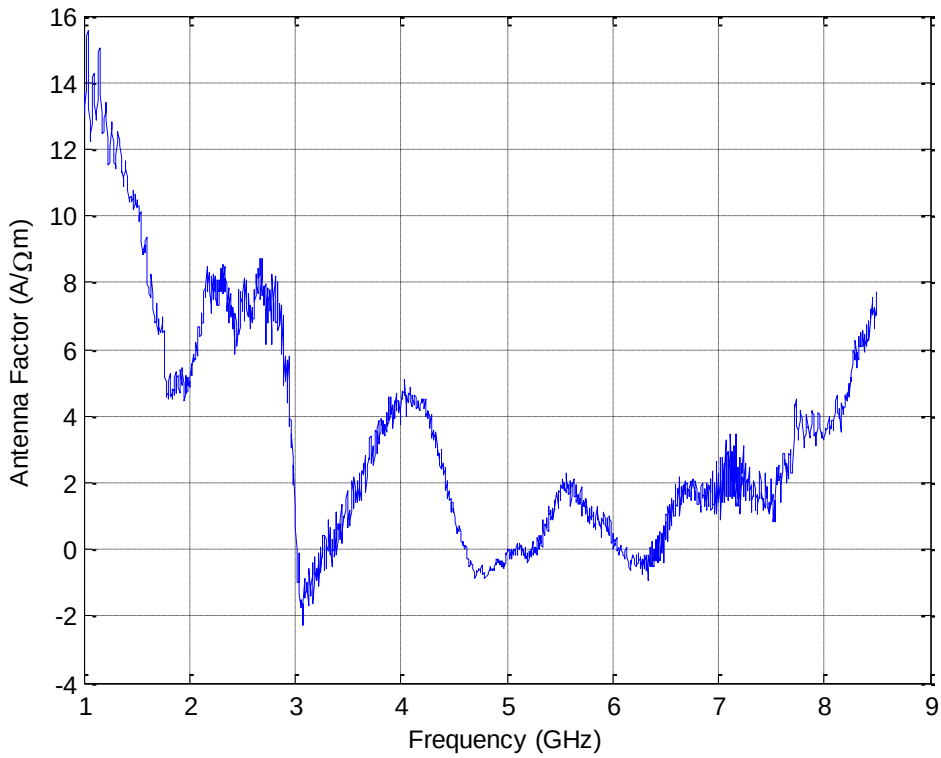

Figure 4.14 Measured antenna factor of the loop

In Figure 4.12 and Figure 4.13, though the loop shows cross-polar rejection larger than 10 dB between 2.5 GHz and 8.5 GHz, it appeared to not be well balanced. The phase difference produced by flipping the excitation source by 180 degrees is about 190 to 120 degrees between 1 GHz and 4 GHz becoming larger as frequency increases. The antenna factor also shows rapid variance in this frequency range. It is considered that a differential amplifier could improve the performance of the loop. As this loop is considered to be unreliable for the magnetic field measurement, and as the research program is limited in time, the following measurements are for electric fields only. The measured antenna factor of the loop is shown in Figure 4.14. In contrast to the dipole antenna factor, which is defined as ratio of incident electric field to the voltage developed on the antenna load, the loop antenna factor, AF_m, is defined as the ratio of incident magnetic field H_{inc} to the voltage on the load V_L, as shown in Equation 4.9. Since the magnitude of the magnetic field is smaller than that of the electric field by a factor of η_0, the overall level of the loop antenna factor is lower than that of the dipole.

$$AF_m = \frac{H_{inc}}{V_L} \qquad \textbf{(4.9)}$$

4.3. The 3-D scanner

A scanning frame was built to carry out measurements of the fields penetrating the joint samples. The scanning frame was designed and constructed by the Physical Layer Research Group and the Technical Support Services (TSS) in the Electronics Department at the University of York. The scanning frame was designed with the absorber box placed at the bottom, exciting the joint sample under measurement. Meanwhile, stepper motors on each of the *x*, *y* and *z* axes drove the antenna to perform a planar field scan above the joint sample. Figure 4.15 shows the top-view of the scanning frame; the scanning frame is connected to a vector network analyser (VNA), with the dipole scanning a joint sample.

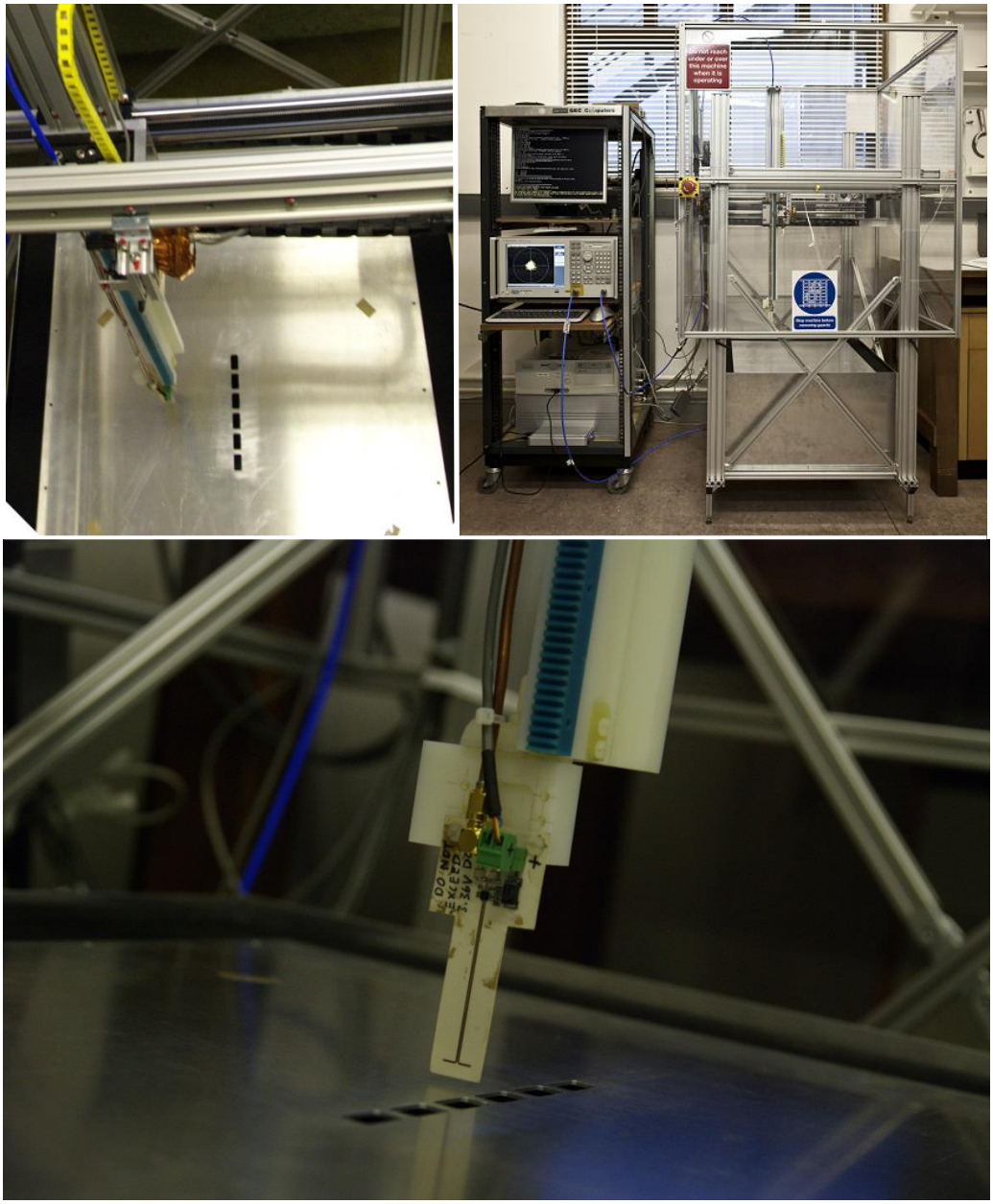

Figure 4.15 Top view of the scanning frame (top-left), scanning frame connected to VNA (top-right) and dipole antenna in measurement driven by the scanning frame (bottom)

This automatic scanning mechanism not only saves time taken if the antenna is re-located manually at every point, but also improves the accuracy and repeatability of the measurements. As in the near-field the field amplitude and phase vary rapidly in space, a slight placement error may result in a large difference in the measurement result.

4.4. Measurement results

The measurement system was then tested by measuring some joint samples. A planar scan of the electric field was carried out on the slot array shown in Figure 4.16. The slot

array consisted of 6, 2 cm long, 1 cm wide slots, separated by 5mm long metal bridges. The dipole antenna was used to measure the electric field; it was placed 17 mm above the slot array, and scanned over a 210 × 210 mm area, with measurement points separated by 5 mm. The electric field was then calculated using the antenna factor determined in Section 4.2.1.

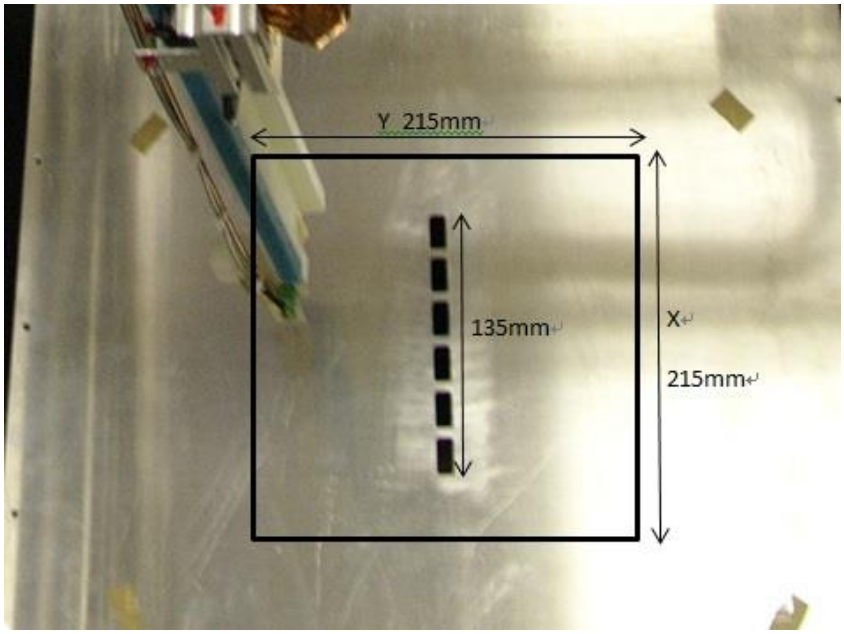

Figure 4.16 Measurement area of the planar measurement above the slot array

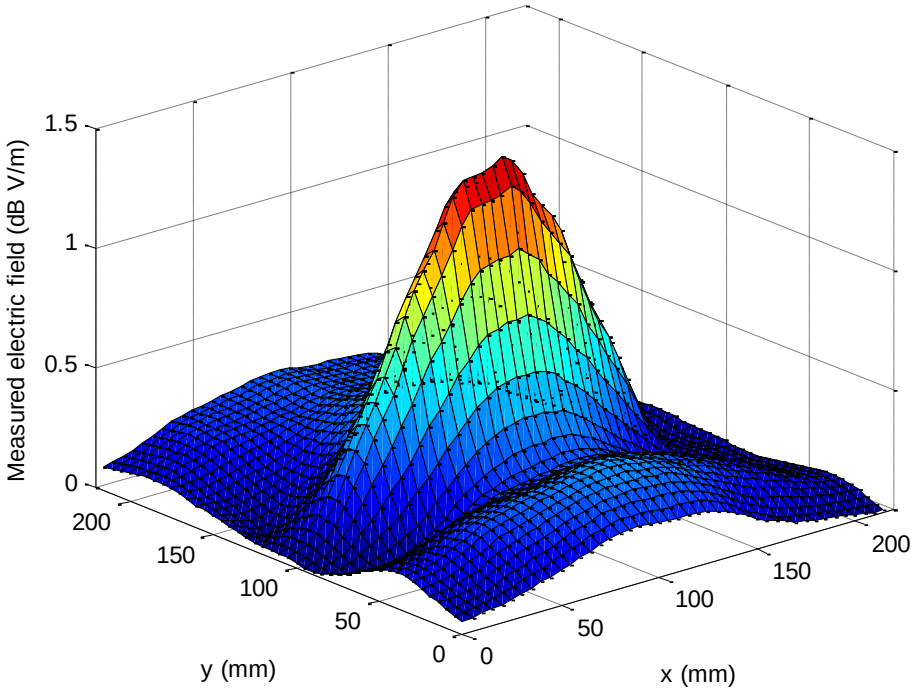

Figure 4.17 Measured *y*- polarised electric field 17mm above the slot array at 3GHz

Figure 4.17 shows the measurement results 17 mm above the slot array at 3 GHz. It can be seen that there are small magnitude electric fields measured in the area about 1 wavelength from the slot array along the *y*-axis. According to Figure 4.16, that area is covered by the metal sheet and the electric field should be shielded. The measured electric field could be from the leakage that has occurred between the sample plate and the absorber, or the dipole might have been interfered with by the electric field in the surrounding environment. However, most of the energy is concentrated in the area of the slot array. At 17 mm, the field distribution appears already smoothed and the details caused by the metal bridges are hard to see.

Another measurement was carried out on two slot samples. In addition to the slot array, a 1 cm wide uniform slot was measured. Instead of measuring a plane, only the centre lines of the samples, where the energy is concentrated, were measured. To observe more field details, the dipole probe antenna was placed 7 mm above the absorber surface. As the sample was 1.65 mm thick, the dipole was placed 5.35 mm above the slot during measurement. The absorber box was also measured with the cavity opened, as a comparison and calibration source for the results obtained from the slot samples.

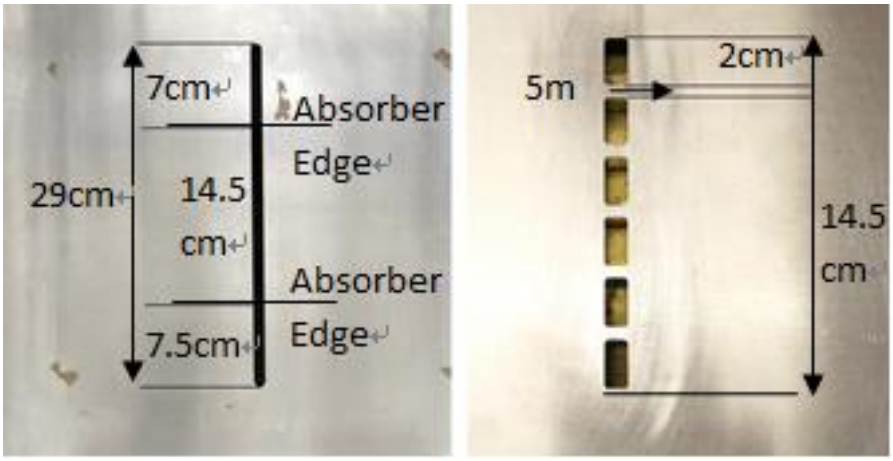

Figure 4.18 Geometry of the slot samples

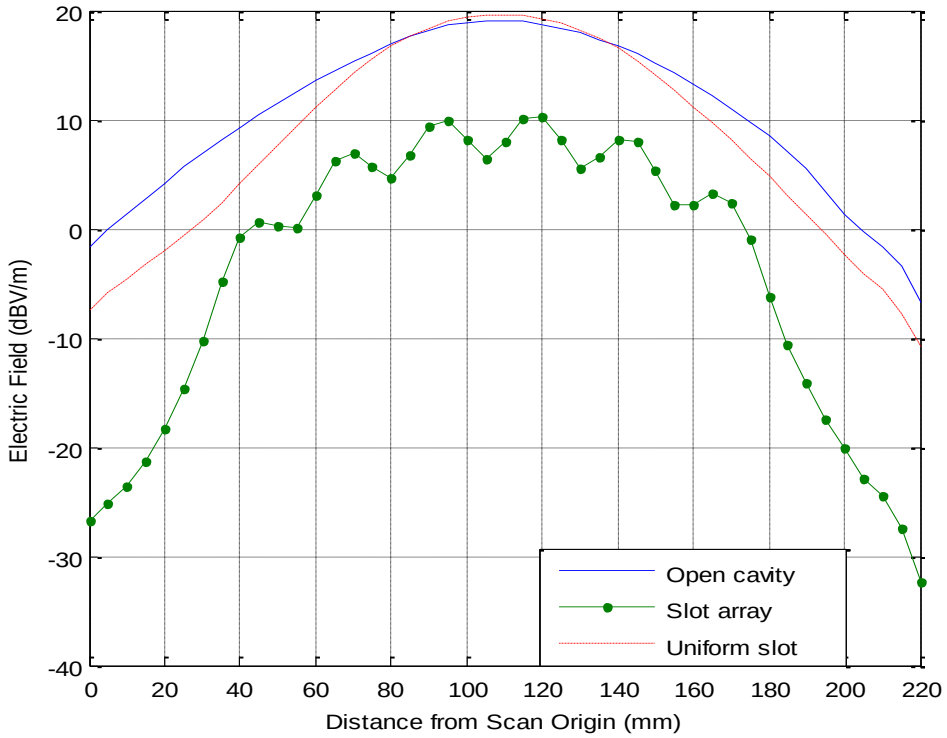

Figure 4.19 Measurement results of the centre lines of the samples

Figure 4.19 shows the electric field along the centre lines of the two slots and the open absorber box aperture, measured at 3GHz. It can be seen here that the excitation generated by the absorber box fell as the slot approached the absorber and the field strength was about 20 dB lower at the absorber edge rather than at the centre. Since we would like to determine the behaviour of a slot or aperture under uniform illumination some compensation must be determined for the actual illumination. Regardless of the measurement methods chosen there is always the possibility of end-effects on a finite length sample, which must be considered.

To observe the accuracy of such measurements, Transmission Line Matrix (TLM) models of the slot samples were simulated with plane-wave excitation and absorptive material terminating the slot. This test was carried out at the early stage of this research program when Vulture was not programmed. The TLM simulation tool 'Hawk' was a reliable method of producing plane wave excitation at that time. 'Hawk' was programmed by Dr John Dawson in the Physical Layer Research Group at the University of York. As the simulation has a different excitation from the absorber box, the ratio of electric field penetrating the sample to the excitation is plotted instead of the absolute field strength.

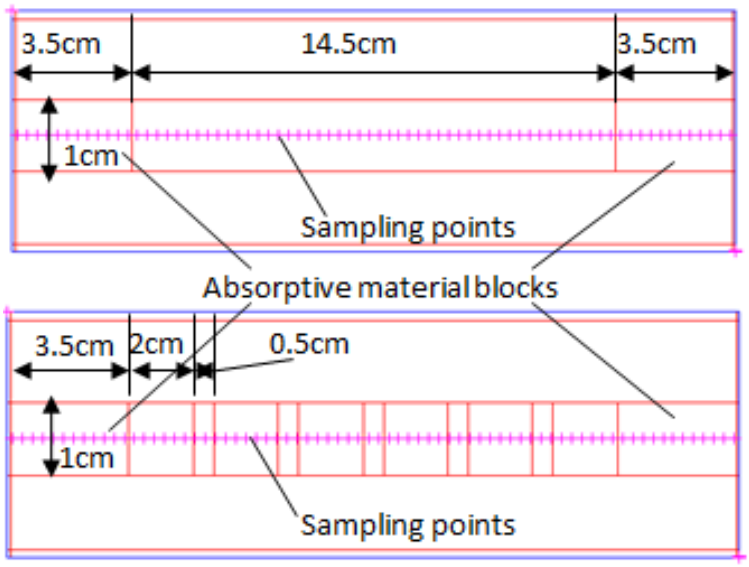

Figure 4.20 TLM simulation geometry of the slot samples

Figure 4.20 shows the TLM simulation geometry. To make the geometry identical to the measurement, the metal bridges at the ends of the slot array were extended to 35 mm and the uniform slot was terminated with two pieces of absorbing material. The mesh size used was 1 mm, and data was extracted every 3 mm along the centre lines of slots.

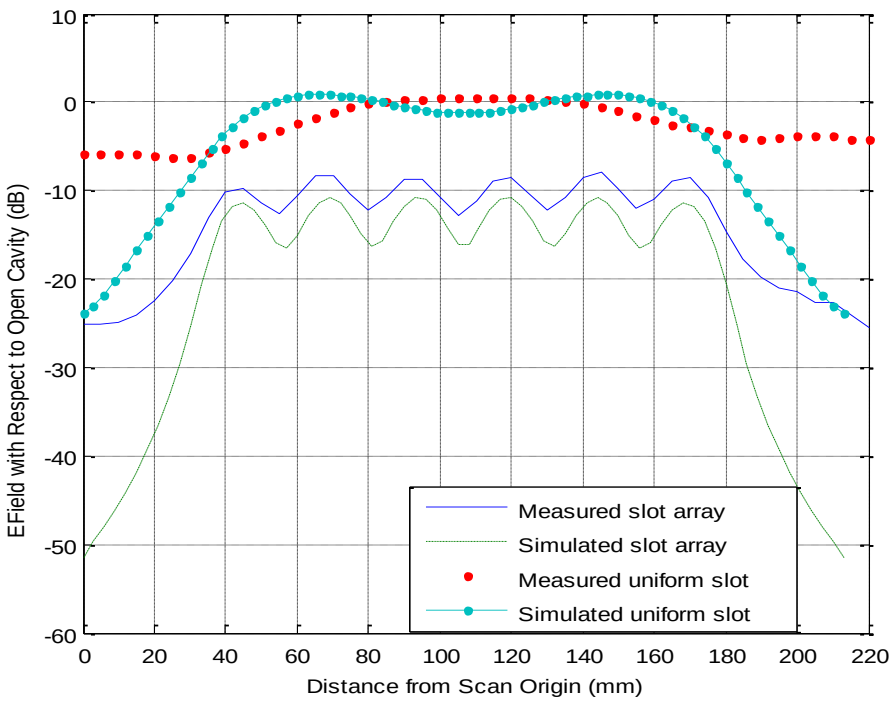

Figure 4.21 Measured and simulated electric field penetrating the slots relative to the excitation fields

By dividing the field measured above the samples by that of the open absorber cavity, it is clearly demonstrated that the curved wave front in Figure 4.19 becomes flattened in Figure 4.21. Measured and simulated results had 5 dB of difference and the measurement shows a shallower roll-off at the ends of the samples. The results of the uniform slot show a narrower flat region than the slot array. A flat line was expected in free space measurement, and the flat region produced by the uniform slot in this measurement was about 3 cm wide. The flat region of the uniform slot measurement was too short to carry out proper characterisation; therefore the following modelling work was based on the slot array measurements.

The differences between the measurement and simulation results have several causes. First, there is imperfection in the excitation antenna and absorber. At such a close distance to the horn antenna, the radiation pattern is still a curved wave front instead of a plane-wave. Additionally, the incident angle of radiation from the horn antenna to the absorber is shallow, which degrades the performances of the absorber. Furthermore, as mentioned when describing Figure 4.17, there are interactions between the excitation field and the slot plate on top of the absorber box. As such a small fraction of the energy is transmitted through the slot, with most of the excitation fields being reflected back into the absorber box. Therefore, the actual field illuminating the slot sample is not the same as that radiated by the excitation antenna in free space and the field measured above the open absorber box is not entirely representative of the illumination field to the slot. Therefore, the calibration method shown here, which calibrates the measured field above the slot samples with that measured above the open absorber box, is a temporary solution before a systematic calibration method is developed. An alternative calibration method that is more accurate is needed for further development of the model.

4.5. Summary

A measurement system was designed and built to carry out planar field scanning to provide measurement data for model building and validation. The absorber box was used to create a free-space environment for the horn antenna located at the bottom of the box. The horn antenna was used as a source of incident field to the slot sample placed on top of the absorbers. A scanning frame was built on top of the absorber box, which used stepper motors to drive the field probe to scan the field above the slot sample. A dipole antenna with a differential amplifier was built as an electric field probe, and a loop without an amplifier was built as a magnetic field probe. The electric field probe with a differential amplifier shows better phase balance, so the rest of the modelling work was

carried out using the electric field measured by it. The loop, however, was not well balanced; therefore it was not used for further measurements.

The illuminating field to the slot sample placed on the absorber box was not the same as the excitation antenna radiating in free space, as the absorber did not work well at a shallow angle of incidence and most of the illuminating field was reflected back into the absorber box. A more systematic calibration method is needed for accurate measurement. In addition, methods to reduce noise, and probe disturbance to the field and diffraction at the sample edge are needed for future measurements on smaller scale structures.

Chapter 5. Model test cases and limitations

As described in the introduction, this modelling work consists of three main modules: an optimisation tool for finding the equivalent source, the implementation of an appropriate FDTD algorithm and measurement device development for gathering validation and verification data. These modules were introduced individually in the previous chapters. This chapter presents the results of the integration of these modules so that the complete modelling process can be validated. First, the GA was used to fit the equivalent dipole moments using the fields measured by the 3-D scanner. These dipole moments were then used as input to the FDTD macro model. Tests on more complex structures were carried out using a simulated near-field since measured fields were not available. Finally, the limitations of this modelling method will be discussed.

5.1. Model application on measured structures

Due to the limitation of the measurement system introduced in Chapter 4, the validation of the macro model using measurement data employed an 'iterative' validation process. A mesh size larger than the slot size was used for the coarse-grid model. At a distance of a multiple of such mesh sizes the scanning frame could not provide reliable measurement data due to the reflection from the scanning frame interfering with the field radiated from the slot; additionally, at this distance, and the field strength could drop below the noise floor. As a result, the measurement data at this distance could not be used for model validation. Therefore, instead of using measured field values, a fine-grid equivalent model was firstly obtained and verified with the measured near-field 7mm above the slot array. This fine-grid model was then used to generate the far-field radiated by the slot array, which was used as validation data for the coarse-grid equivalent model. The interference from the surrounding environment of the scanning frame was removed by using such an iterative validation process.

5.1.1. Model application on planar scanned near-field above the slot array

As mentioned above, the modelling method was firstly applied to the measured electric field in order to obtain a fine-grid FDTD equivalent model. Basically, this first step of validation was carried out by connecting the individually validated GA in Chapter 2 and the FDTD implementation in Chapter 3 together. The field was measured above the array of six 2×1 cm slots, and the GA was set to search for one magnetic dipole moment at the centre of each slot. The population size was set as 50 and the search was performed through 400 generations. The search results were then used as input to the

equivalent model in the FDTD simulation with a 1mm mesh size and the observation plane located 7mm from the equivalent dipoles. The fit was performed at 2 GHz, at which the results in Figure 5.3 were plotted.

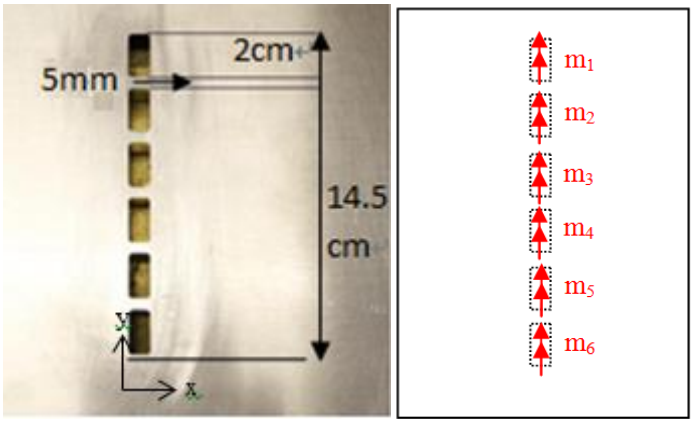

Figure 5.1 Slot array geometry (left) and dipole moment distribution for the GA search (right)

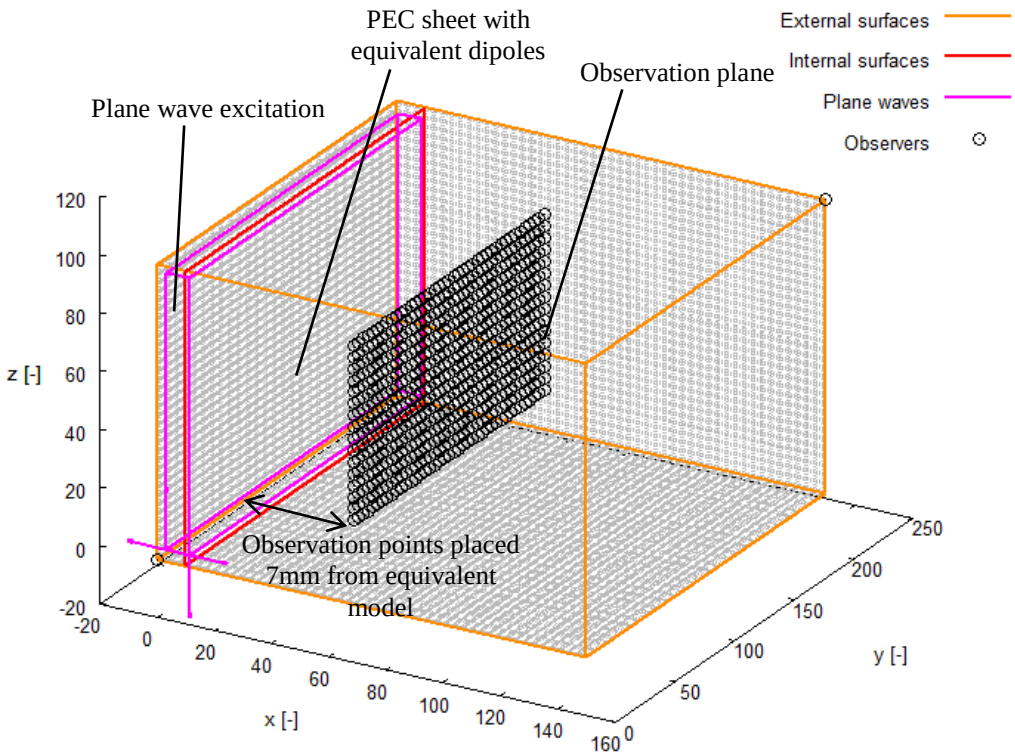

Figure 5.2 FDTD model with equivalent magnetic dipoles to simulate the slot array

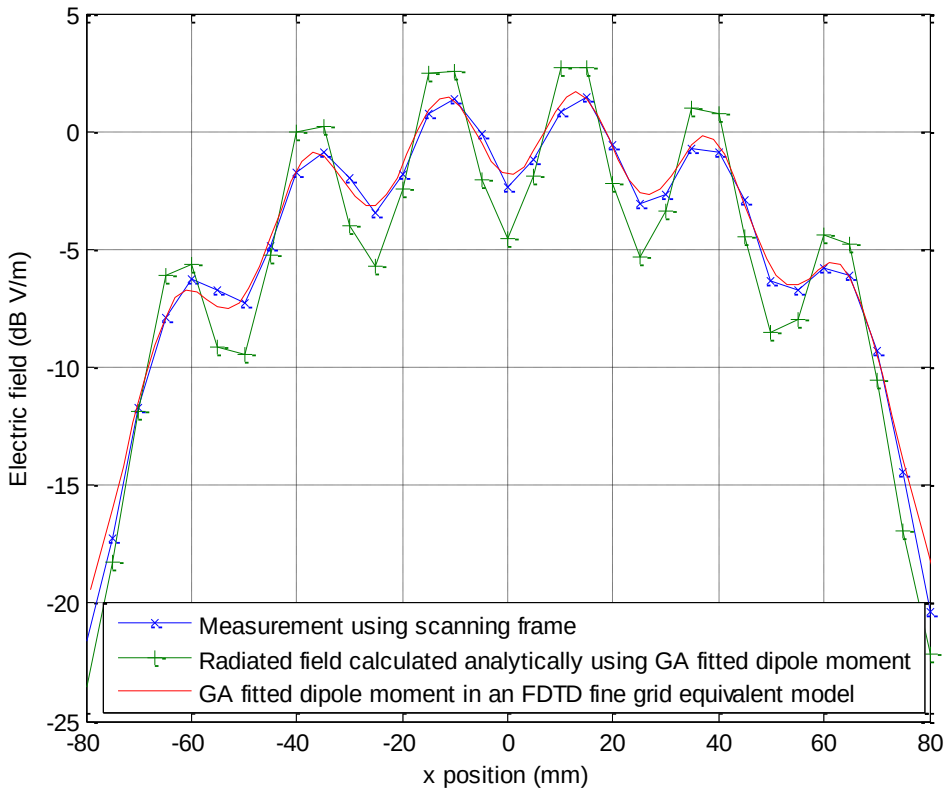

Figure 5.3 GA search result and GA result applied to FDTD equivalent model at 2GHz

Figure 5.3 shows the radiated electric fields from the GA fitted magnetic dipole moments. The fields were also calculated analytically provide comparisons to those generated by the equivalent model in the FDTD simulation. The analytic calculation did not include the mutual coupling between dipoles, which resulted in differences in levels and shapes from the other two curves. The GA searched dipole moments reproduced the amplitude of the electric field from the measurement accurately. The curve obtained from the FDTD model was smoother than that of the measurement due to the increased spatial resolution of output points in the FDTD model than the measurement.

5.1.2. Model application on radiated far-field from slot array in coarse FDTD grid

Having proved the modelling process was able to model the slot array accurately in the 1 mm grid FDTD mesh, the model was then applied to the coarse mesh as a sub-cellular model. As stated previously, the limitation of the measurement method made it impossible to obtain the field radiated from the slot array without excessive interference from the surroundings. At this stage, validation data was generated using the fine-grid model described in Section 5.1.1, which was considered to be more accurate than the measured data in the far-field. Figure 5.4 shows the geometries of the fine-grid and

coarse-grid models. The mesh size increased from 1mm to 25 mm, which was just larger than a single element of the slot array. Note that as the mesh size increased, the spatial resolution of output points significantly decreased.

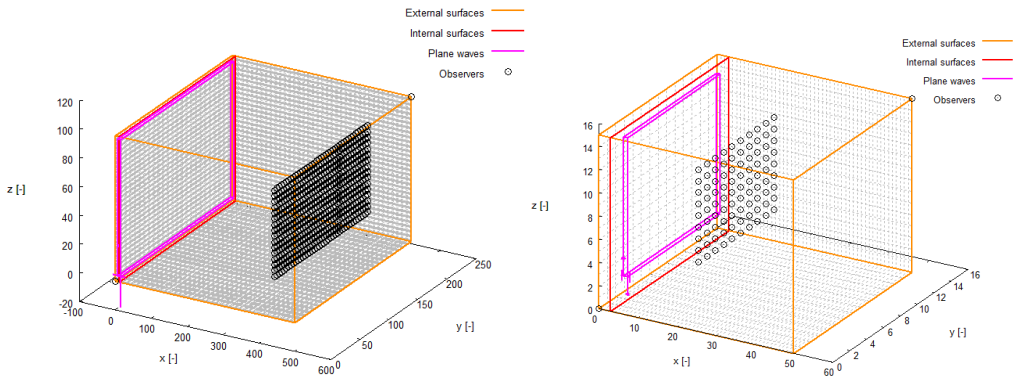

Figure 5.4 Geometries of the FDTD fine-grid (left) and coarse grid (right) models with equivalent dipoles built in

Considering the upper frequency limit of a 25mm FDTD mesh was 1.2 GHz, the results below are plotted at 1 GHz, with the observer plane 30 cm from the slot plane. The phase calibration method introduced in Section 3.6 was applied to these models.

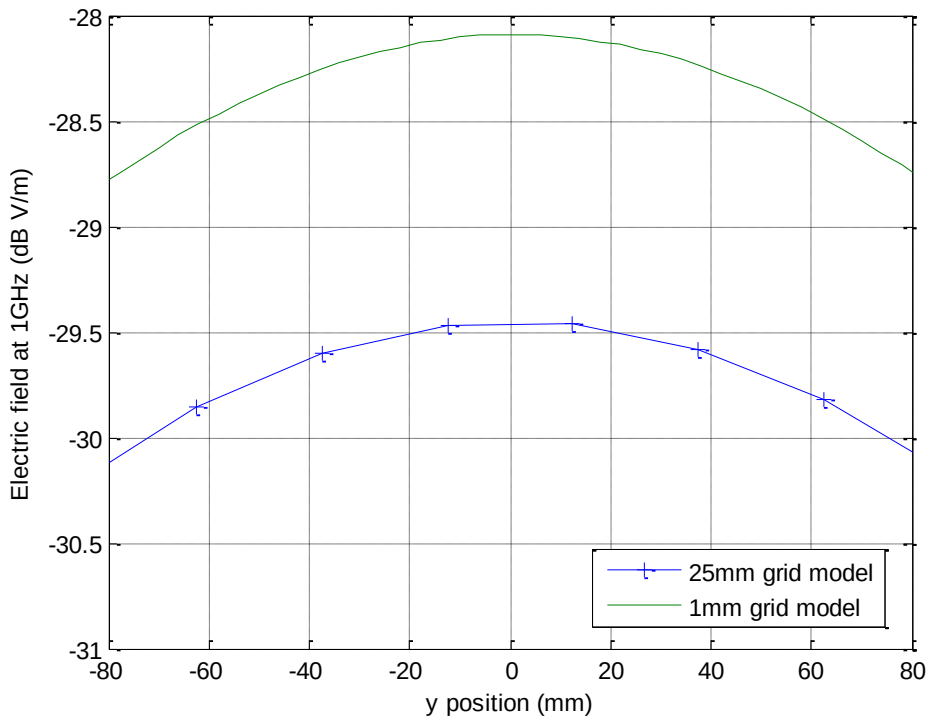

Figure 5.5 Field distribution of fine- and coarse-grid equivalent model of the slot array along *z*- centre line at 1 GHz

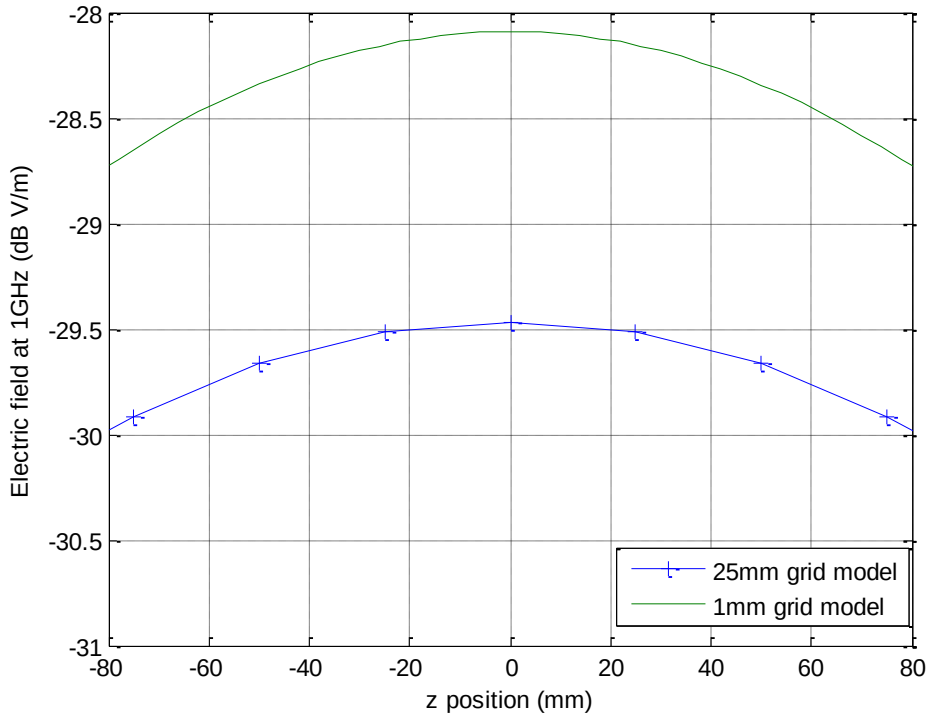

Figure 5.6 Field distribution of fine- and coarse-grid equivalent model of the slot array along *y*- centre line at 1 GHz

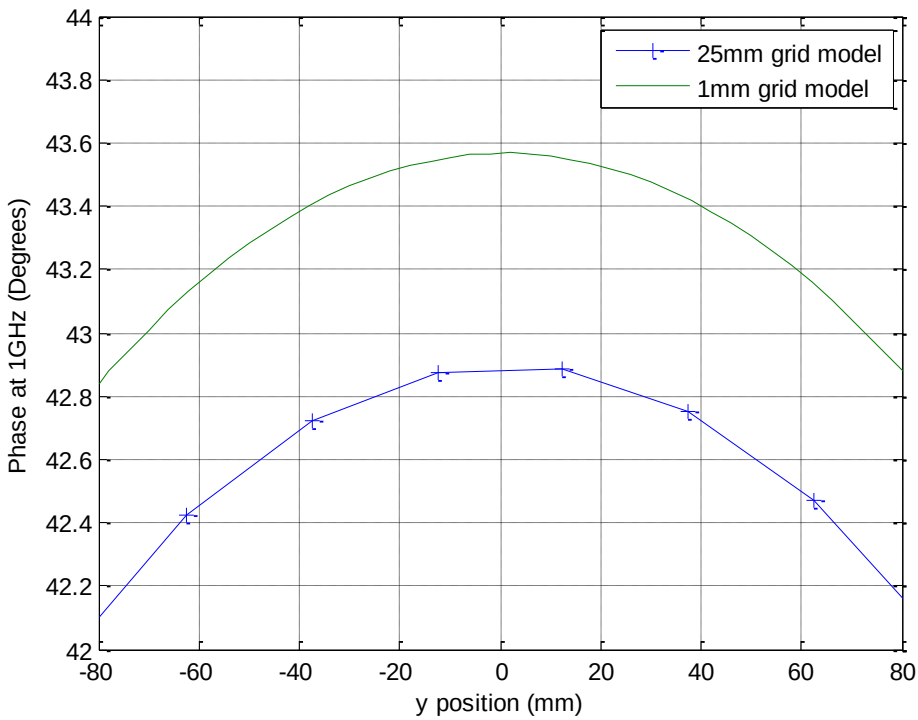

Figure 5.7 Phase of electric field produced by fine- and coarse-grid equivalent model of the slot array along *z*- centre line at 1 GHz

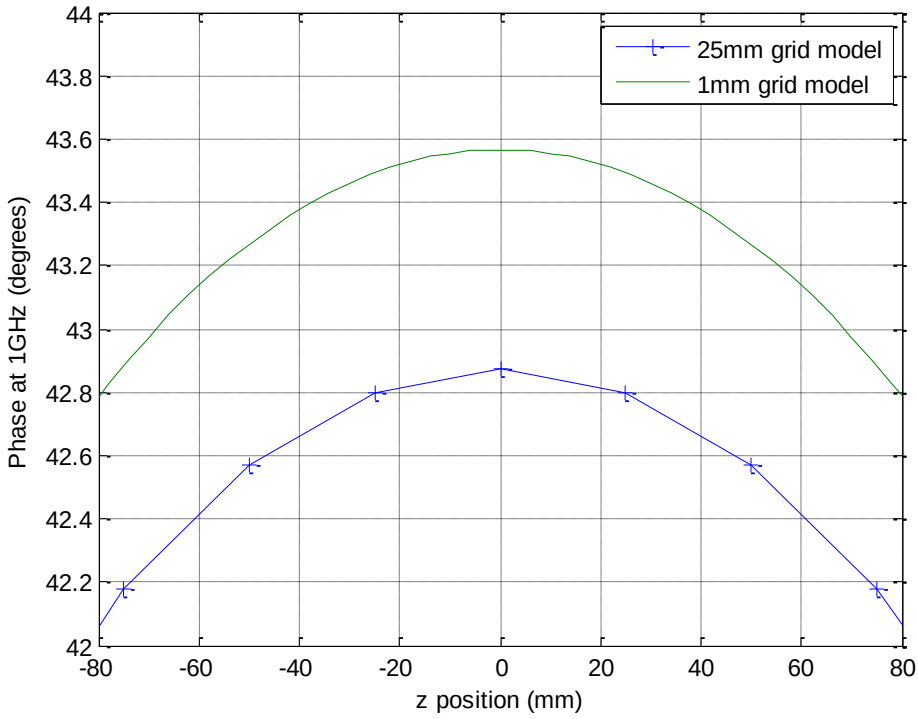

Figure 5.8 Phase of electric field produced by fine- and coarse-grid equivalent model of the slot array along *y*- centre line at 1 GHz

The above figures show that the equivalent model could accurately reproduce the fine-grid simulation with a few dB error in amplitude and that in terms of phase was within a degree across the output plane. Note that the sampling points in the frequency domain of these two models are not at identical frequency points. This was induced by the different time steps of the models due to mesh size variation. The above figures were sampled at the frequency points closest to 1 GHz in the models, which contributed to the errors. Figure 5.9 shows the frequency domain result at the centre of the output plane. It is seen that the frequency point taken in the 1mm grid model is 1.049 GHz, while in the 25 mm grid mesh it is 1.0013 GHz. In the frequency domain, the macro model was capable of following the fine-grid model until about 1.2 GHz, at which frequency the mesh size is too large compared to the wavelength and numerical dispersion starts to affect the accuracy as discussed in Chapter 1 and Chapter 2.

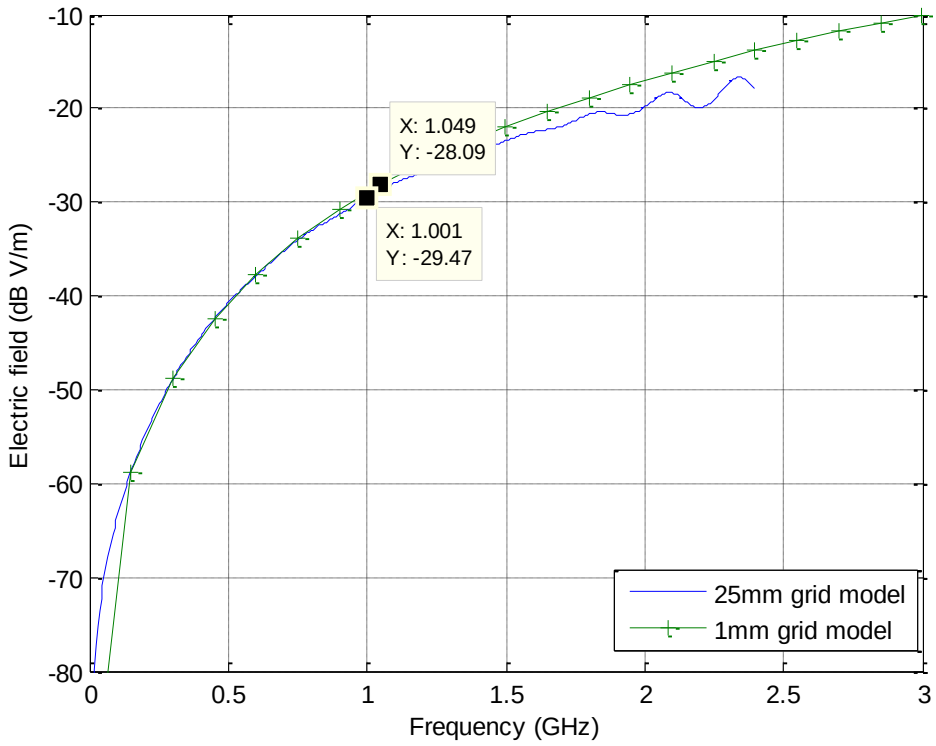

Figure 5.9 Electric field intensity in the frequency domain, produced by fine-grid and coarse-grid equivalent models of the slot array

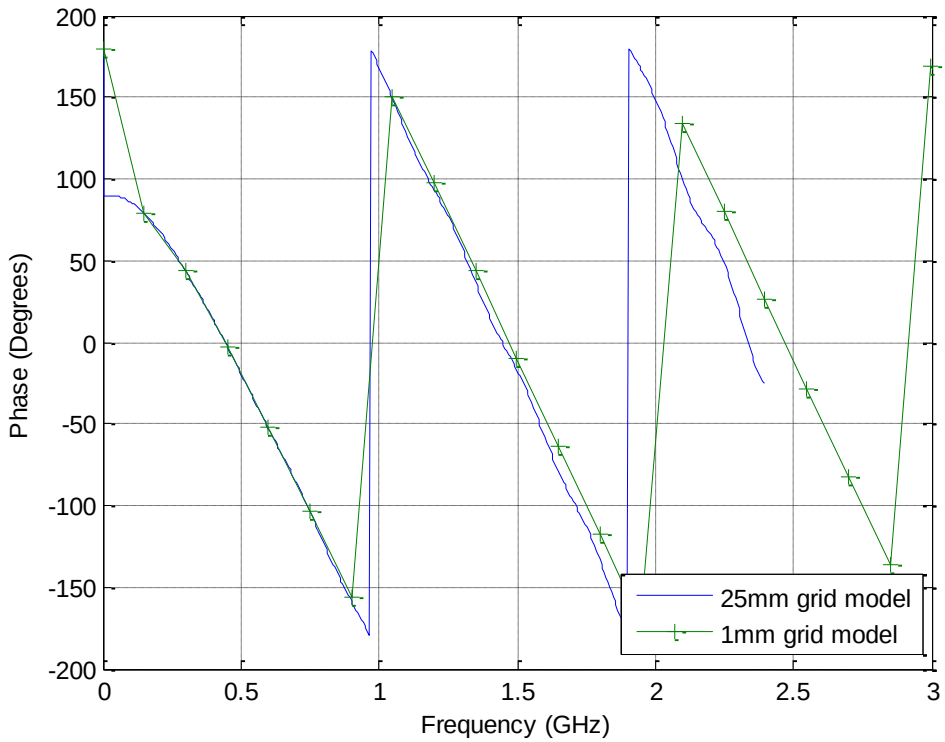

Figure 5.10 Electric field phase in the frequency domain, produced by fine-grid and coarse-grid equivalent models of the slot array

5.2. Model tests on more complex structures

5.2.1. Single aperture spanned across two coarse-grid meshes

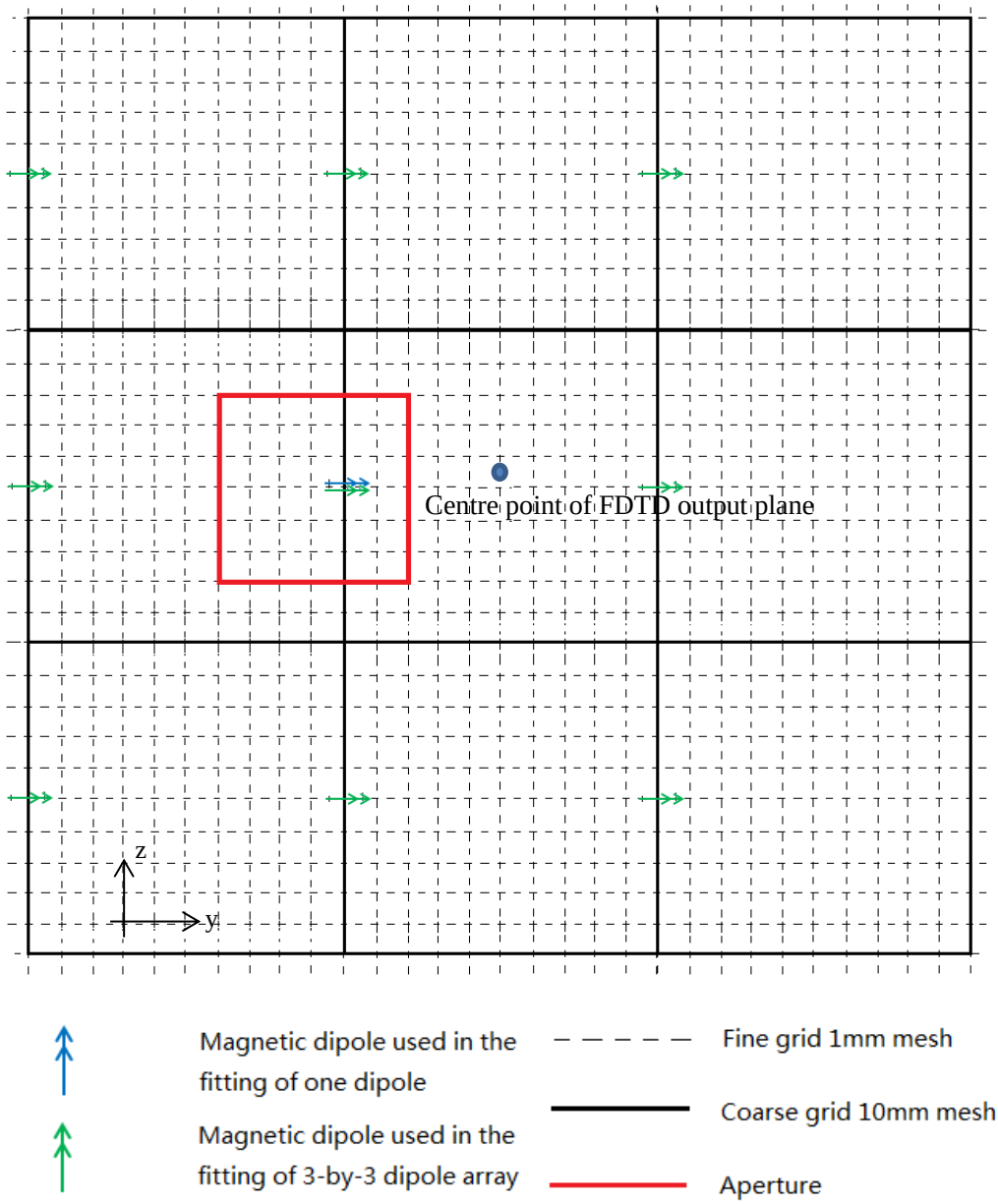

Figure 5.11 Mesh distribution on testing the model with aperture across two coarse meshes

The previous tests have kept the problem symmetrically distributed along the centre axis of the problem space to ease model verification. In the test case shown in Figure 5.11, an aperture is located so that it spans across two meshes in the coarse grid simulation. The aperture was 6 × 6 mm in size, located in the centre of the *z*-axis but occupied 2mm in the centre coarse-grid mesh and 4mm in the adjacent one. The observation points covered an 8 × 8 cm area, located 6cm from the aperture. The coarse-grid mesh used a 10mm mesh size and the observation points were 20 cm from

the equivalent models. Note as described in Section 3.6.2, the dipole moments were located on the lower *y*-surfaces instead of at the centre of the coarse meshes.

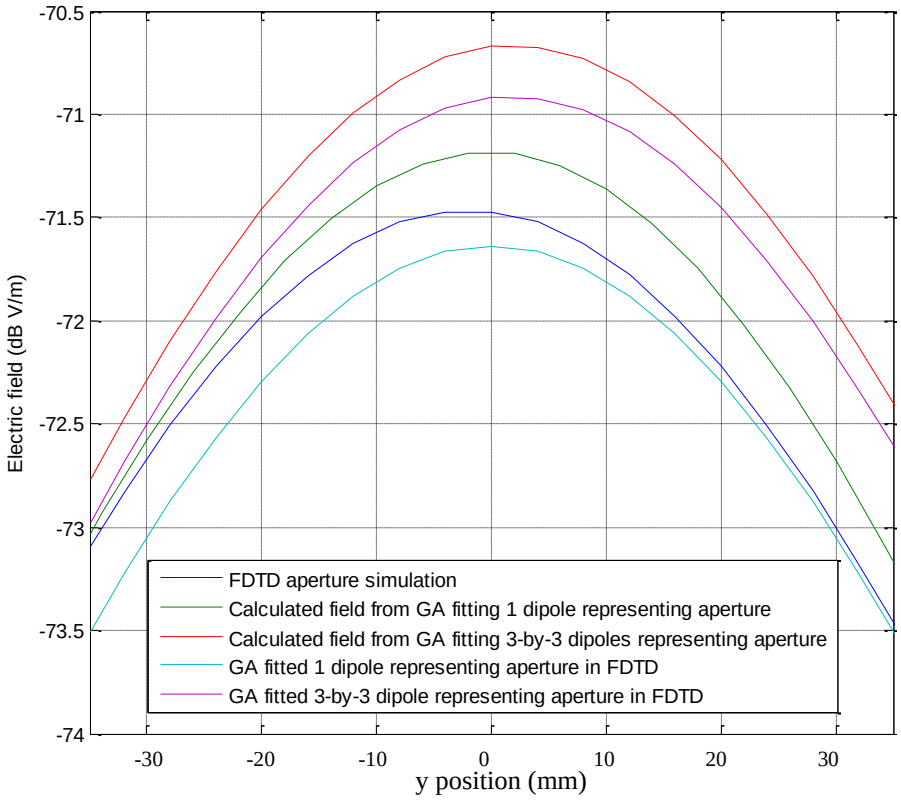

Figure 5.12 Near-field distribution of the aperture simulated by FDTD, calculated using equivalent dipole moment fitted by GA, and simulated with the equivalent dipole moment in FDTD

There were two attempts of GA fittings: a single dipole moment in the centre mesh, and a 3 × 3 dipole array with the aperture covered as shown in Figure 5.11. Figure 5.12 shows the near-field distributions of the GA fitted dipole moments, both calculated analytically and simulated with the equivalent FDTD model. By observing the field distribution obtained from FDTD aperture simulation, it can be seen that maximum field intensity is not at the centre of the *y*-axis, which corresponds to the location of the aperture. In previous examples, the apertures were centred at the position where the magnetic dipoles are calculated in the FDTD meshes. In this case, a single dipole moment could not place the peak value at the right position. On the other hand, as shown in Section 2.3.3, increasing the number of dipole moments added more flexibility to the result, although more generations were needed for the GA to find accurate solutions. As mentioned in the introduction, a GA has some difficulty in reaching the bottom of the error surface, which is clearly shown here. Hybridising the

GA to another optimisation method, such as a descent optimiser, could offer a solution to such a problem. However, despite the inaccuracy of the detailed wave front, the overall levels of these results were within 1 dB of each other. These dipole moments were then inserted into a coarse-grid model with 10mm mesh size and the electric field produced 20 cm from the aperture was observed. A fine-grid simulation with the same dipole moments was used to provide verification data.

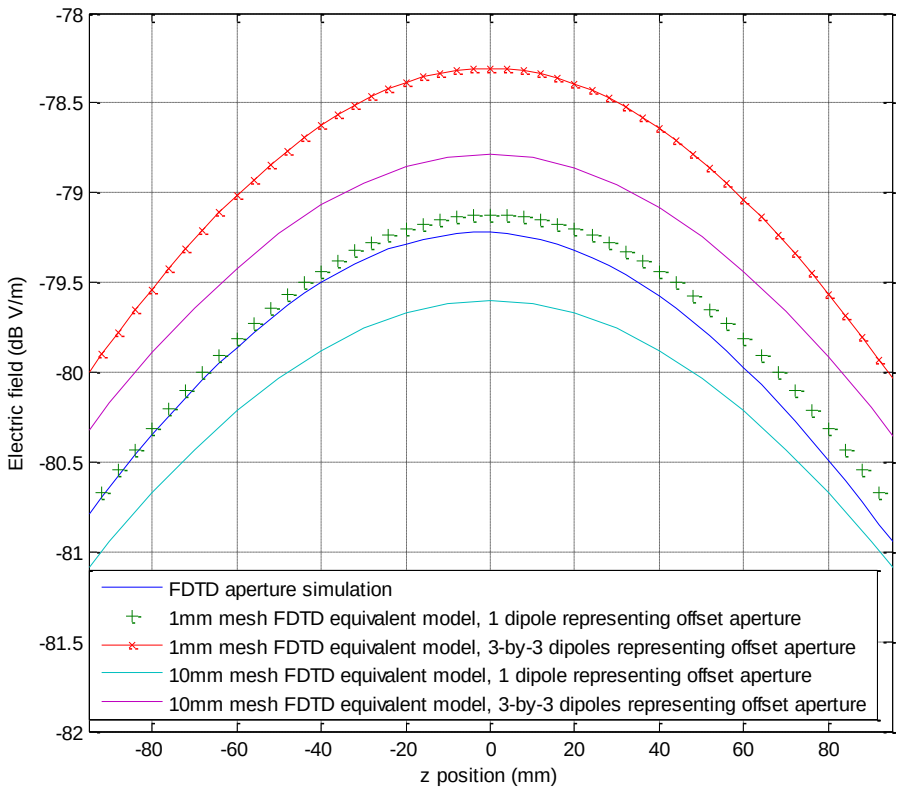

Figure 5.13 *y*-centre line electric field distribution of fine- and coarse-grid models at 2GHz

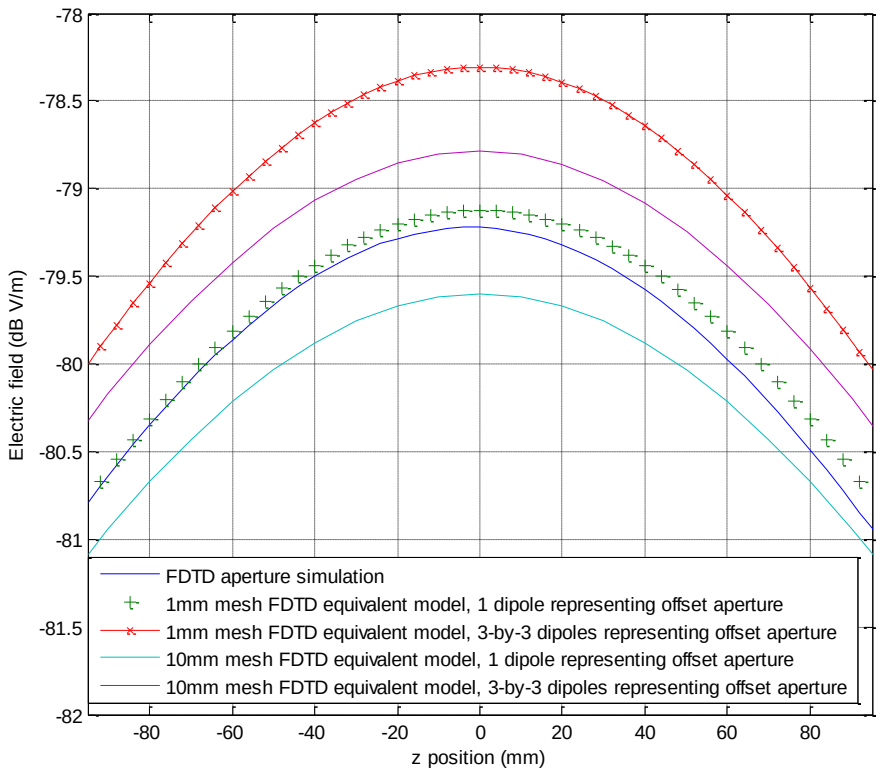

Figure 5.14 *z*-centre line electric field distribution of fine- and coarse-models at 2GHz

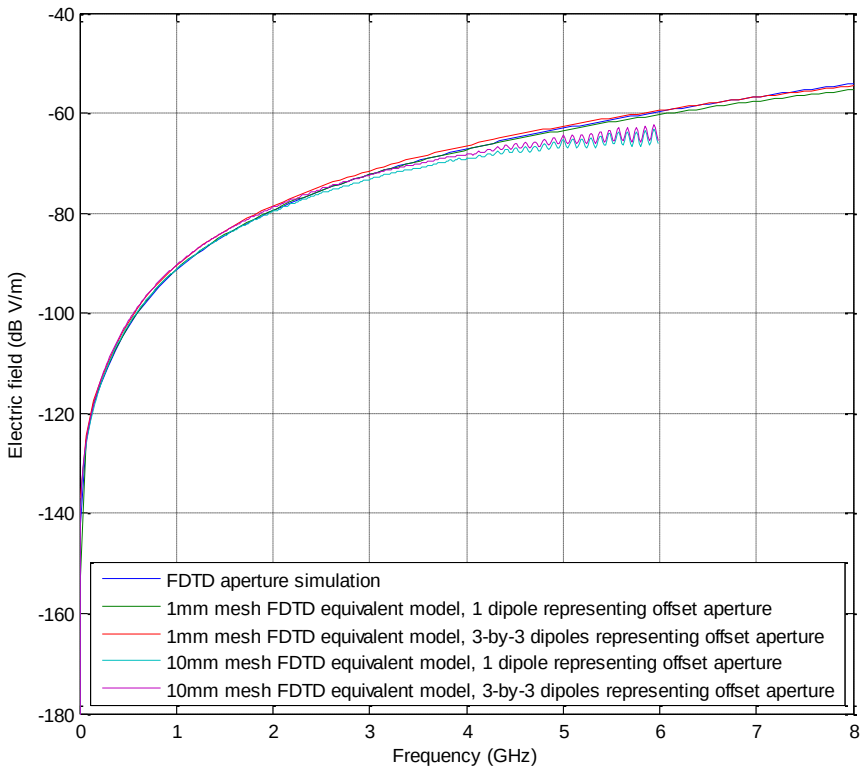

Figure 5.15 Electric field vs frequency at centre point of output plane

Figure 5.13 to Figure 5.15 show the results of the electric field produced by the equivalent models in 1mm and 10mm meshes. It can be seen at a distance significantly larger than the displacement of the aperture from the centre position, the position of the aperture produced little effect on the position of the peak value of the electric field. The overall magnitudes of the electric fields produced by the models were within 2 dB from each other at 2 GHz. Similar magnitude error can be observed in the frequency domain plot from the output point at the centre of the observation plane in Figure 5.15.

Figure 5.16 to Figure 5.18 show the phases of the electric fields plotted above. Similar effects to the magnitude results are seen in these figures. When the displacement of the structure was small compared to the mesh size, the effect it induced was insignificant at a distance much larger than this displacement. A single dipole moment placed in the mesh that contained part of the aperture was capable of reproducing the fields in a macroscopic sized mesh. Though inserting more dipole moments was expected to produce better accuracy, the computational demand was increased significantly as the GA approached the bottom of the error surface more slowly.

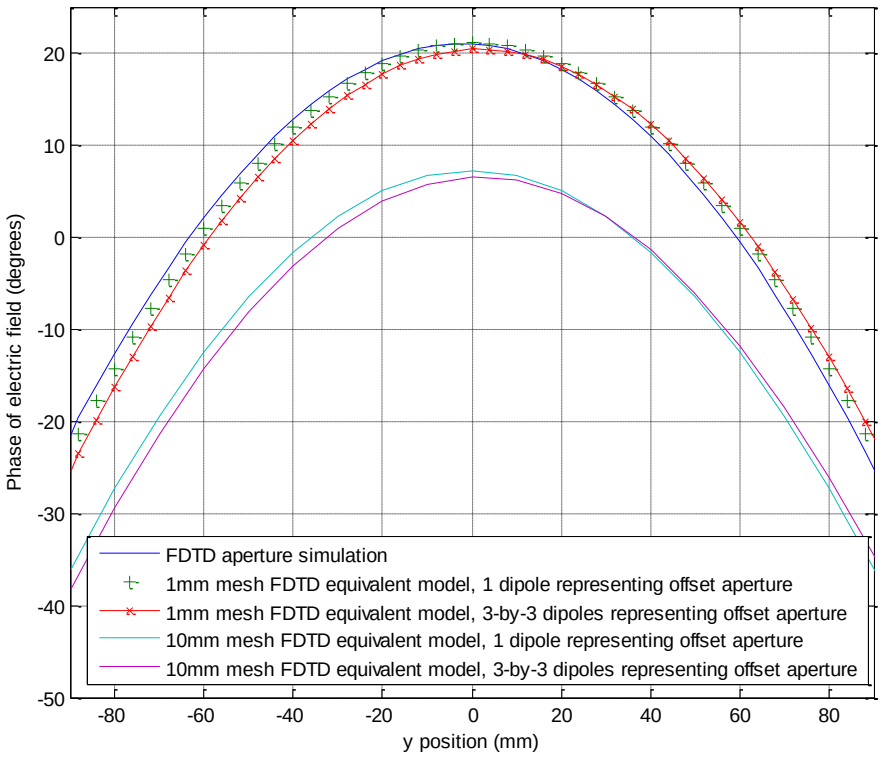

Figure 5.16 *z*-centre line phase distribution of the electric field at 2GHz

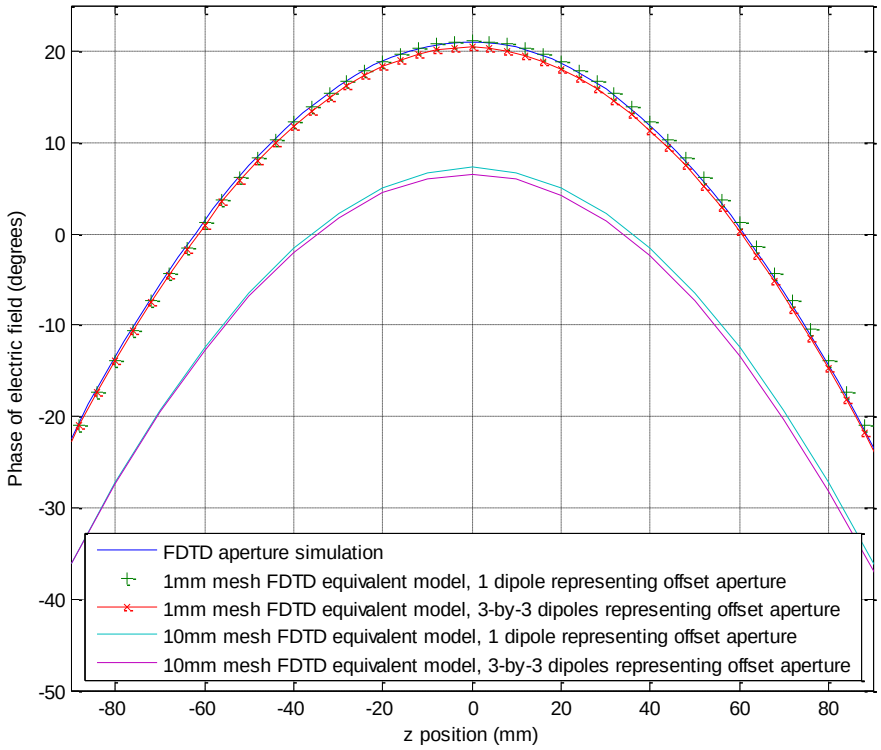

Figure 5.17 *y*-centre line phase distribution of the electric field at 2GHz

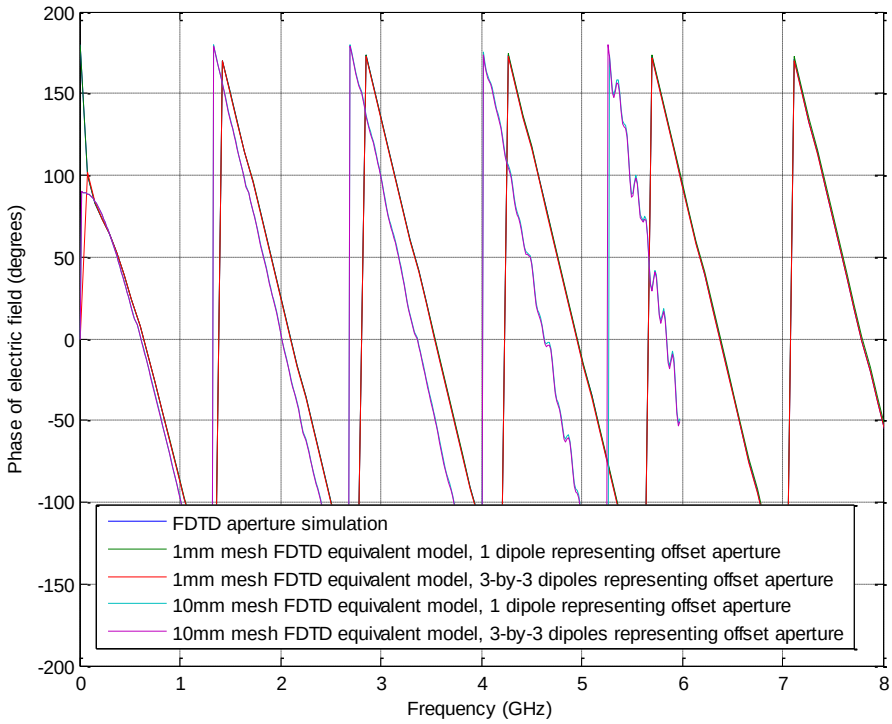

Figure 5.18 Electric field phase vs frequency at centre point of output plane

5.2.2. Two small apertures in one coarse-grid mesh

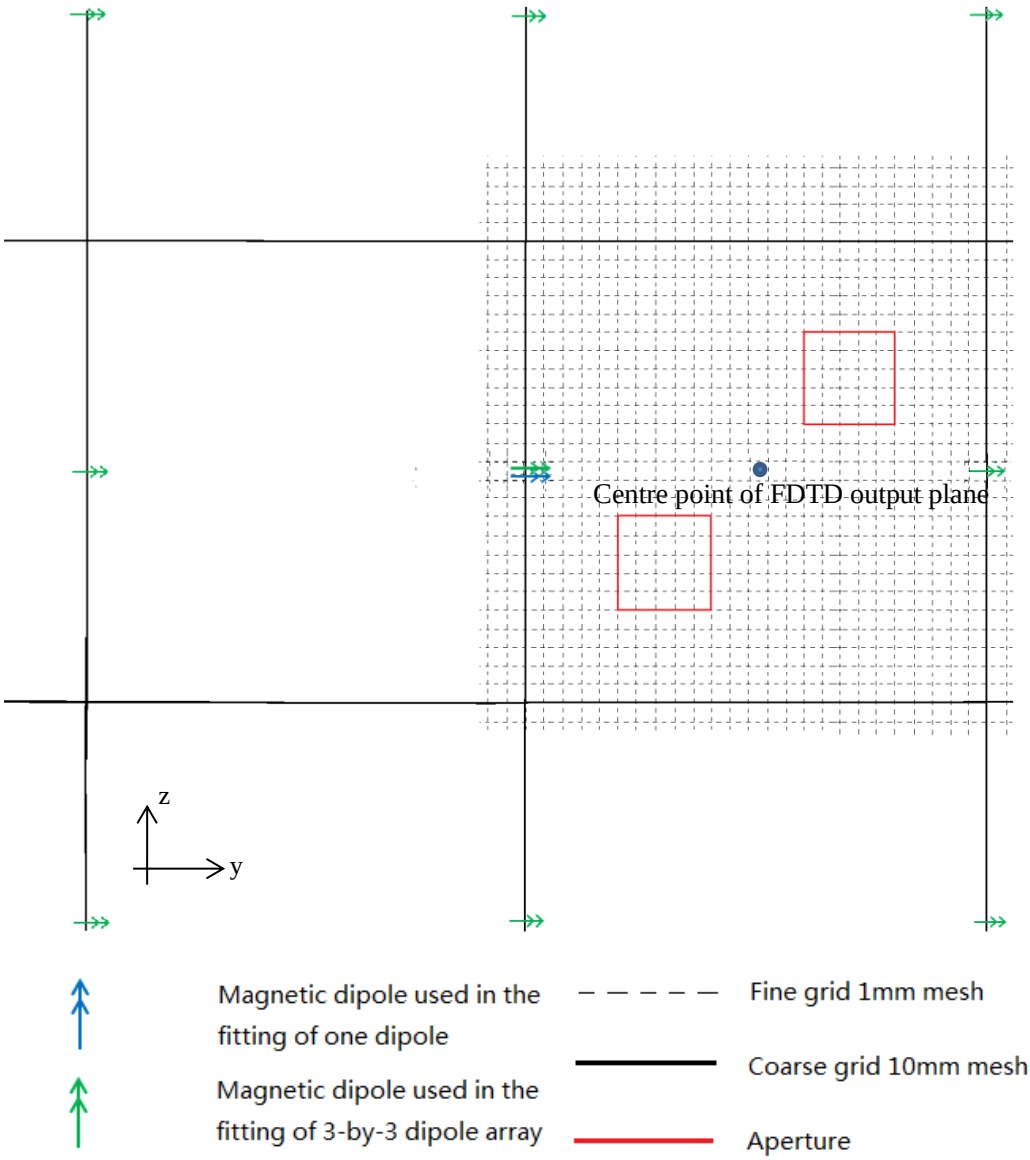

Figure 5.19 Mesh distribution on testing the model with two apertures located in one coarse mesh

In this test, two small apertures were located in one coarse mesh. These apertures were 5 × 5 mm in size, one located 5 mm from lower *y*- and *z*- sides of a coarse mesh, another located 5 mm from higher *y*- and *z*- sides of the same coarse mesh. The other details of the fine-grid simulation, which were used to provide the source field for the GA to fit, were kept the same as in Section 5.2.1. It was expected that with two radiating sources the main lobe of the radiation pattern might be broader than that of a single small aperture. As shown in Figure 5.19, a single magnetic dipole was fitted by the GA to represent the apertures. After that, a 3 × 3 dipole array was fitted to observe whether increasing the number of dipole moments would increase the accuracy of the equivalent model.

Figure 5.20 shows the near-field distributions of the GA fitted dipole moments, both calculated analytically, and simulated using the FDTD equivalent model. Similar effects are seen as in Section 5.2.1, where a single dipole moment could accurately reproduce the field from the structure. The difference between the calculated and simulated results is within 1 dBV/m. In addition, adding more dipoles was expected to increase the accuracy. However, it is clearly shown that with the same generations, the 3 × 3 dipole array did not converge to a result better than the single dipole fit. Considering the field produced by a single dipole moment was about 0.5 dBV/m from that radiated by the actual source, the improvement brought by increasing the number of dipoles was not significant compared to the extra computational effort required.

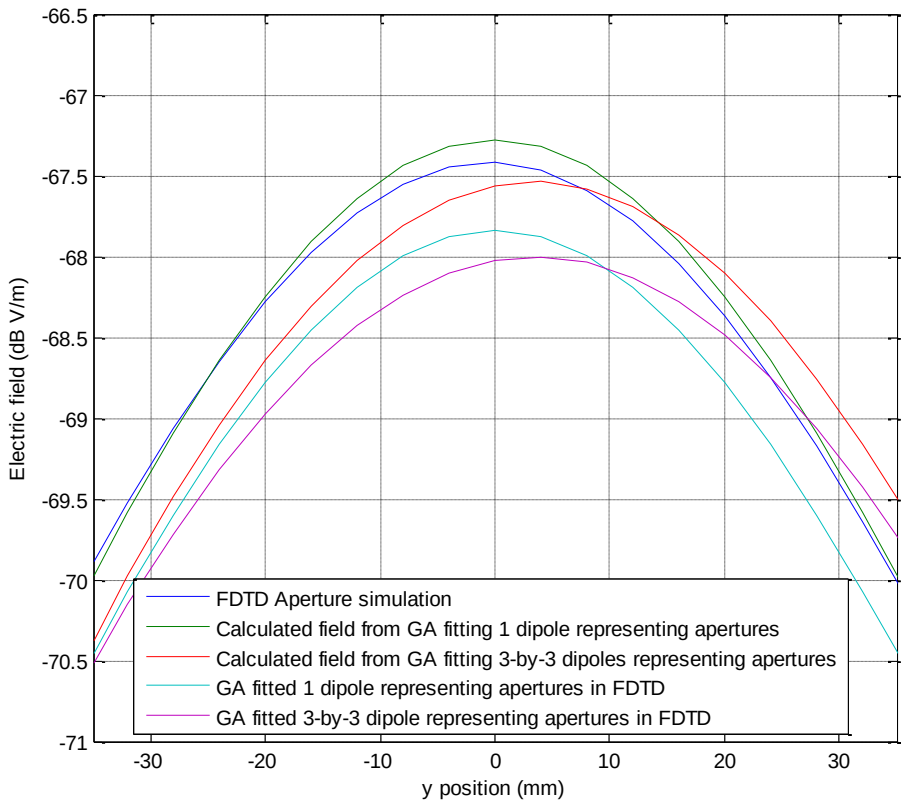

Figure 5.20 Near-field distribution of the two square apertures simulated by the FDTD method, calculated using equivalent dipole moment fitted by the GA, and simulated with the equivalent dipole moment in the FDTD method

Figure 5.21 to 5.23 show the magnitude of far-field 60 cm from the apertures produced by the apertures simulated in the FDTD model, FDTD simulation of the GA fitted equivalent dipoles and field calculated using the GA fitted dipoles. Note the mesh size of the coarse-grid simulation was increased to 25 mm in order to contain the two apertures in a single mesh; in contrast the previous test case used 10 mm mesh size. Since the mesh size chosen was 25 mm, the model appears reliable up to 1.2 GHz; these

results are plotted at 1 GHz. It can be observed that the error is consistent to that shown in Figure 5.20. Moreover, the differences in the location of the maxima of the fields cannot be observed in these figures. In Figure 5.20, the differences in location of the maxima are about 4 mm, since the far-field is simulated at 60 cm from the apertures, these differences became insignificant and cannot be observed. In Figure 5.23, all the results are within 3 dBV/m of each other across the simulated frequency range.

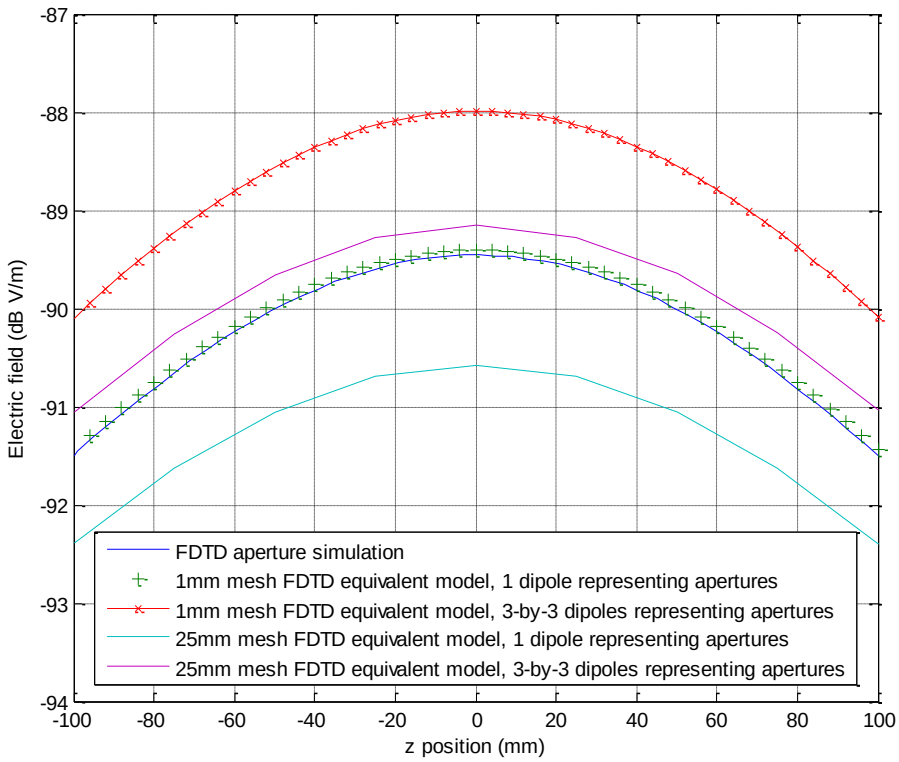

Figure 5.21 *y*-centre line electric field distribution of fine- and coarse-models at 1GHz

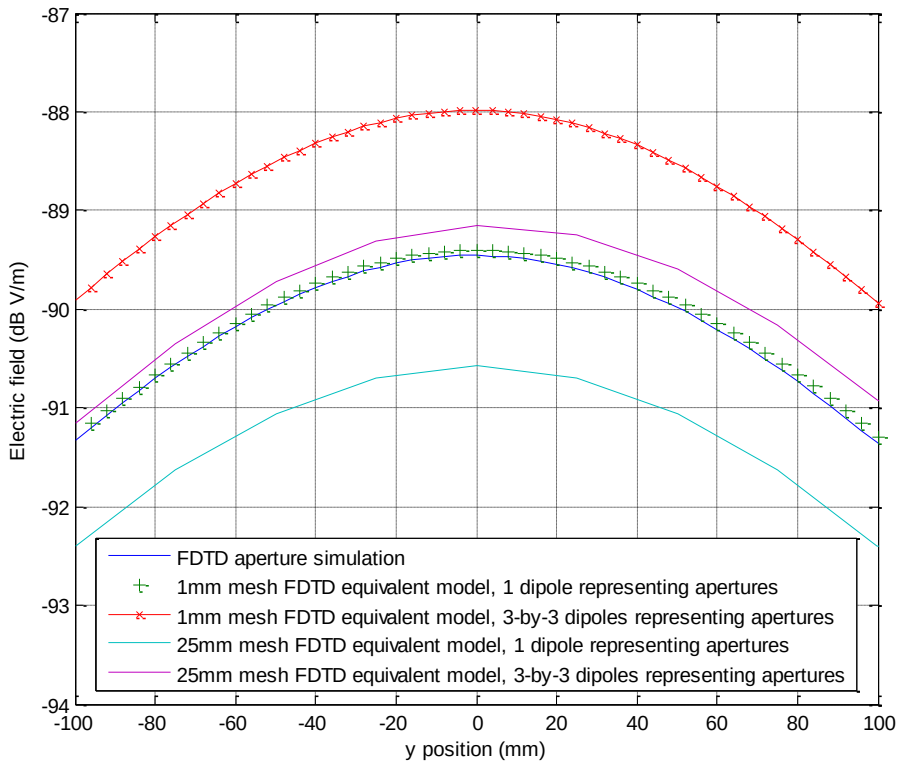

Figure 5.22 *z*-centre line electric field distribution of fine- and coarse-models at 1GHz

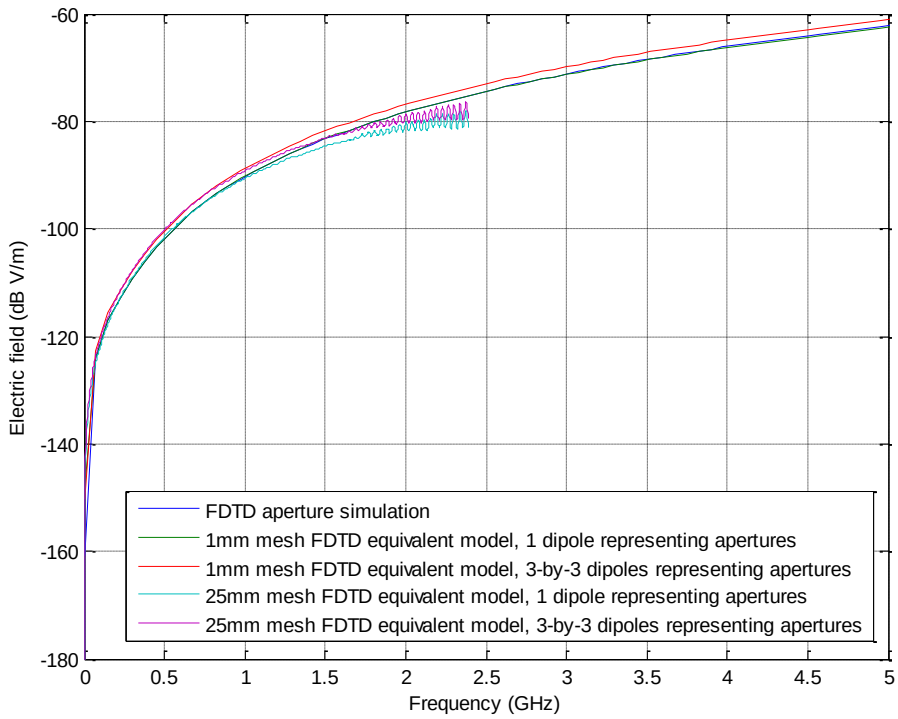

Figure 5.23 Electric field vs frequency at centre point of output plane

Figure 5.24 to 5.26 show the phase produced by the aperture simulated in the FDTD model and represented by equivalent dipoles. The same observations can be made as for Figure 5.21 to 5.23, where the errors produced by the equivalent dipoles are less than 10 degrees from those simulated by the aperture model. These results are considered satisfactory.

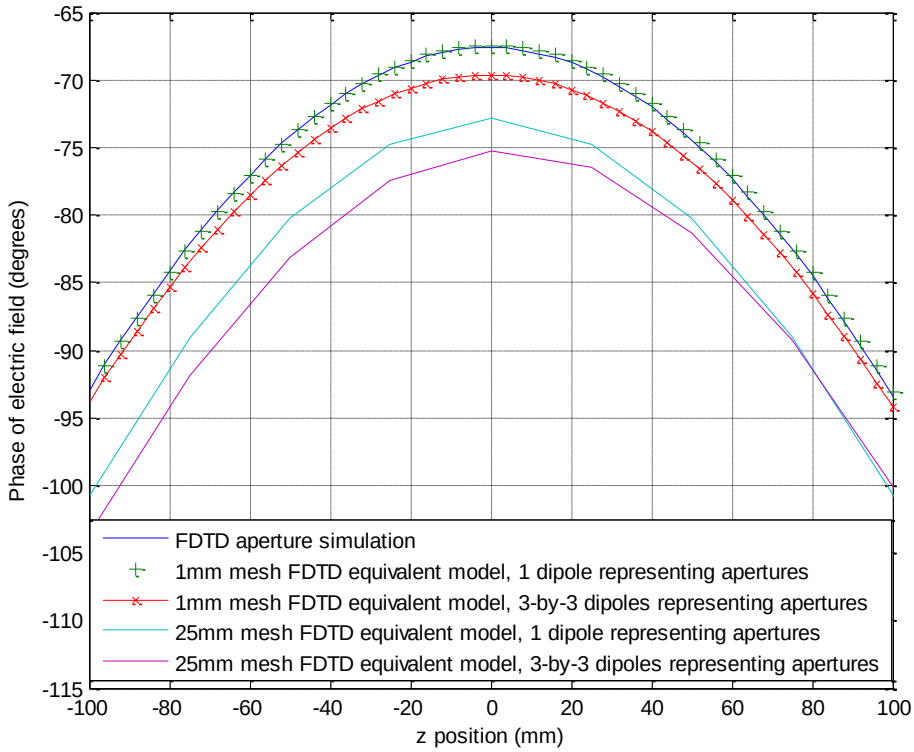

Figure 5.24 *y*-centre line phase distribution of the electric field at 1GHz

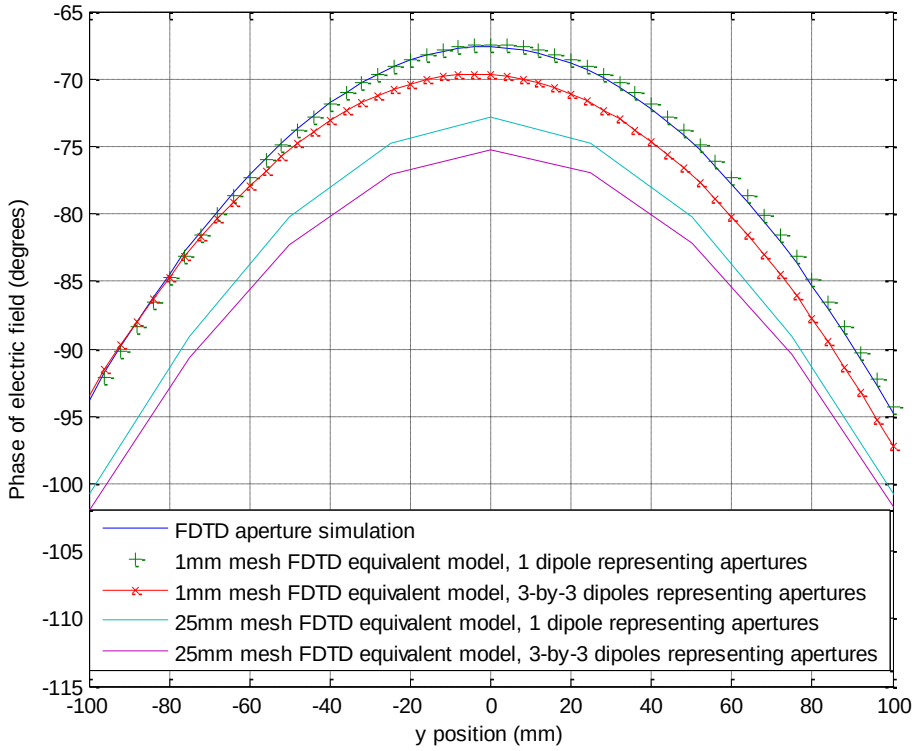

Figure 5.25 *z*-centre line phase distribution of the electric field at 1GHz

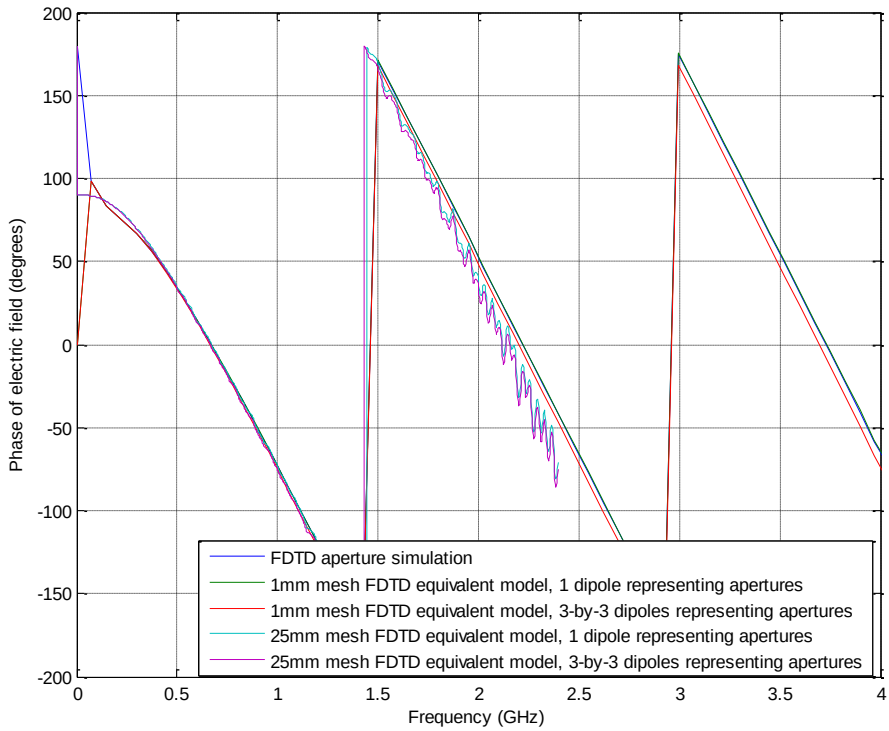

Figure 5.26 Electric field phase vs frequency at centre point of output plane

5.2.3. A more realistic joint

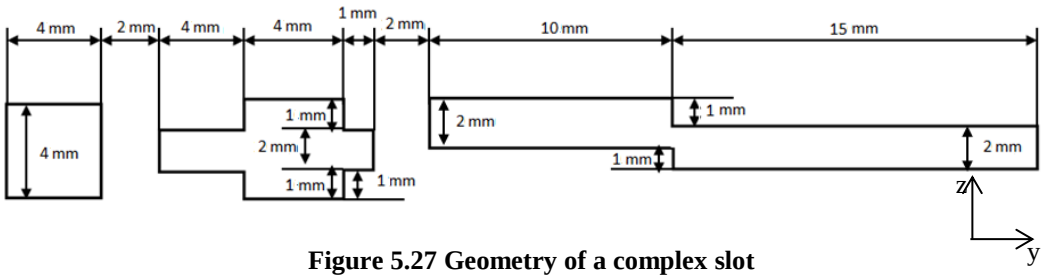

Figure 5.27 Geometry of a complex slot

Figure 5.27 shows the geometry of a complex slot which is more likely to be seen in an airframe. The slot consists of three differently shaped apertures, separated by 2 mm. The width of the structures varies between 2 mm and 4 mm, the whole length of the structure was 41 mm. This structure contains multiple apertures and arbitrary variations in dimensions. It can be used to represent a section of the panel joint or the gap between an aircraft body and a compartment door; where the width is not uniform, and the gap is divided by fasteners. This structure is used as the last step of the model test and validation as it could be the most complex structure modelled.

To maintain accuracy for the detailed simulation of the structure, an FDTD mesh size of 0.5 mm was used; so that there were four meshes across the narrowest part of the structure. Such a mesh size limited the simulation volume, as the memory size required by an FDTD simulation is dependent on the number of meshes contained in the simulation volume. For the maximum number of meshes usable, reducing mesh size would reduce the simulation volume size. Due to such a limitation, the structure could not be designed as one with a very large length-to-width ratio, which is commonly seen on an aircraft. However, the variations on this structure were representative as one section of a joint on an aircraft. In addition, the far-field was simulated 25 cm from the aperture, and the observation plane covered a 60 × 60 cm area.

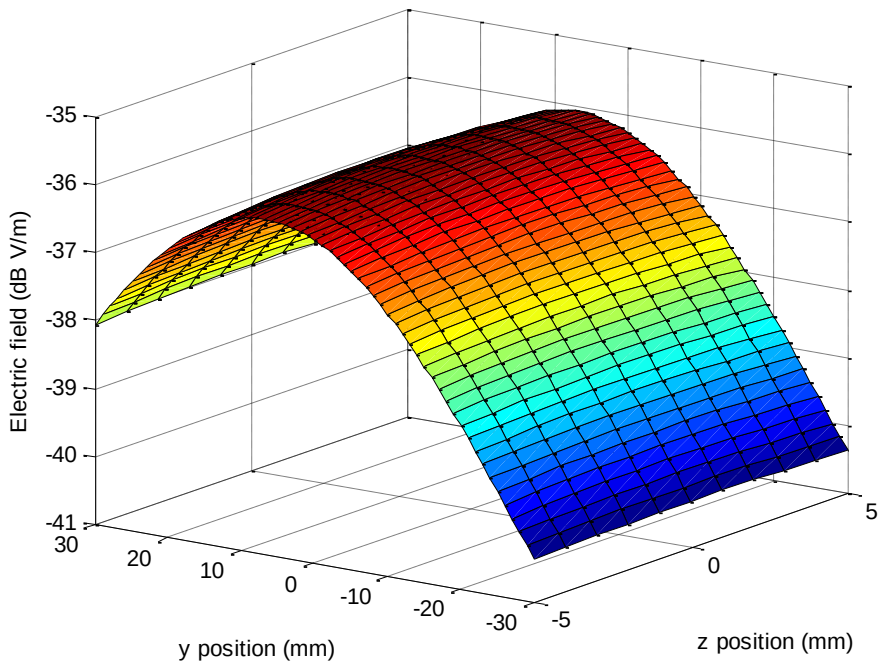

Figure 5.28 3-D plot of the penetrated field 45mm from the structure at 2GHz

A plane wave *z*-polarised electric field was excited to illuminate the structure. The near-field was observed 45 mm from the structure. Figure 5.28 shows a 3-D plot of the near-field at 2 GHz. It is seen that since the structure had a continuous aperture at the higher y-end, the field intensity was higher at that position. However, at 45 mm from the apertures, the details of the wave front created by the variations of width and the metal separators were smoothed out. The GA fitted an 8 × 3 array of magnetic dipoles, separated by 1cm and with a centre point matching that of the structure. Since there were 24 dipoles, the complexity of the GA fitting was increased significantly compared to previous tests, with 3000 iterations run by the GA. Figure 5.29 shows the result of the GA fittings, and the overall error was within 1 dB between the model and the aperture simulation.

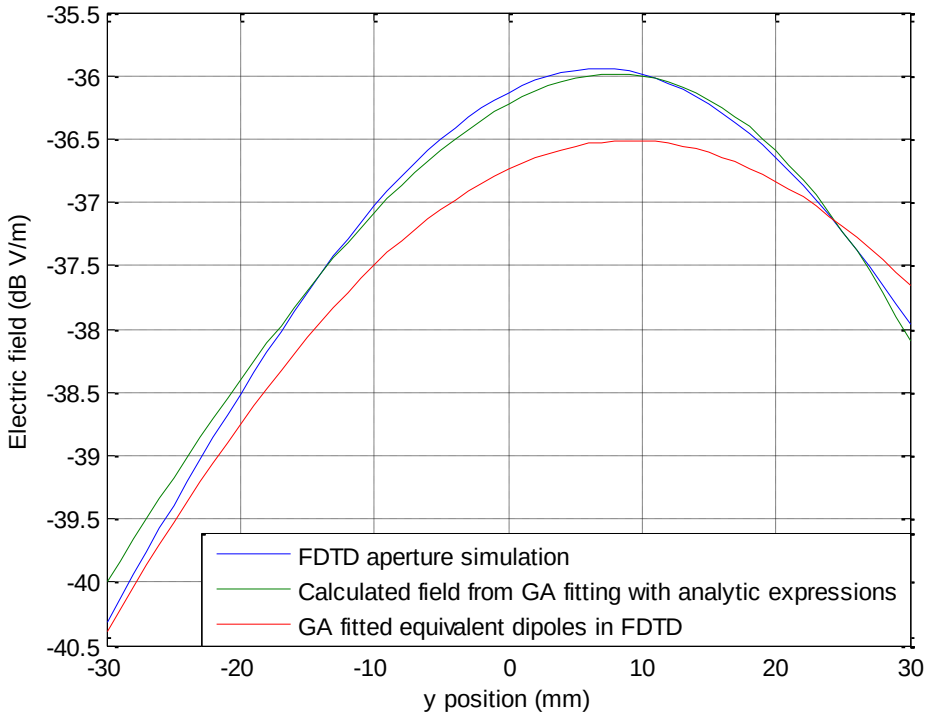

Figure 5.29 Radiated field of the GA fitted dipoles in both analytic calculation and FDTD equivalent model, compared to that of the FDTD aperture simulation

The equivalent model was then simulated in a coarse-grid model with a 1cm mesh size. Figure 5.30 to Figure 5.33 show the far-field modelling results in terms of frequency and spatial domains. In the frequency domain result in Figure 5.30, since the structure was more complicated, there are small ripples at low frequencies and with a resonance appearing at about 5.3 GHz. However, as discussed previously, the equivalent dipole approximation is valid when the aperture is small. The largest dimension of the slot structure is 25 mm, the corresponding frequency when 25 mm is a quarter of a wavelength is 3 GHz. Another factor restricting the upper frequency limit of the model is the FDTD mesh size. The mesh size is 1cm for the coarse-grid model; therefore the FDTD simulation result is reliable up to the frequency where 1 cm is 1/10 of a wavelength, which is 3 GHz. Due to the above limitations of the upper frequency where the model is valid, the spatial field distributions are plotted at 2 GHz. In addition, it can be seen in Figure 5.30, the results of the aperture simulated in the FDTD model and the equivalent dipoles in the fine- and coarse-grid models are within 2 dBV/m of each other up to about 2.5 GHz. Spatially, there are some differences in the slope of magnitude and phase, and a small difference in the positions of the peak of the field as well. These differences were expected as the locations that the fields calculated were different between the fine- and the coarse-mesh. In addition, as the number of dipoles

were increased significantly, it became more difficult for the GA to reach the answer that reproduces the exact field radiated by the aperture.

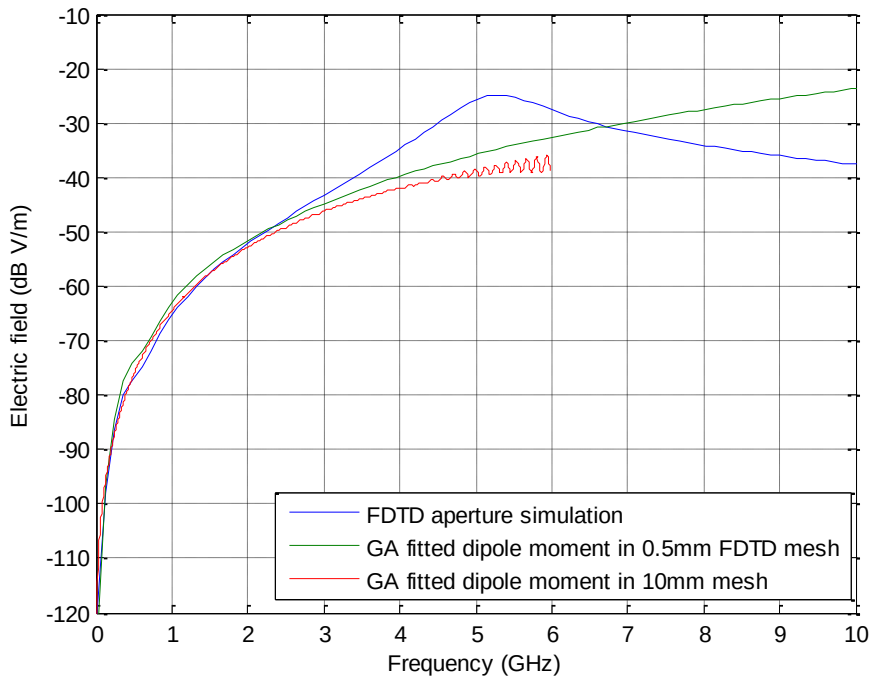

Figure 5.30 Frequency domain result of the equivalent dipole in 0.5mm and 1mm mesh, taken at the centre point of the observation plane

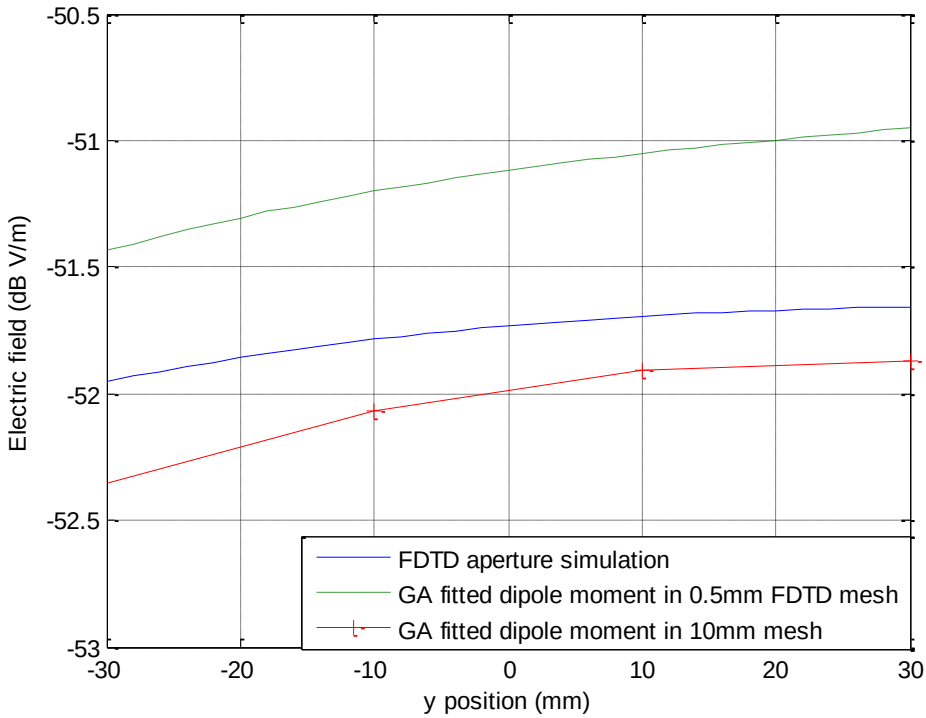

Figure 5.31 *z*-centre line far-field distribution of fine- and coarse-mesh models at 2GHz

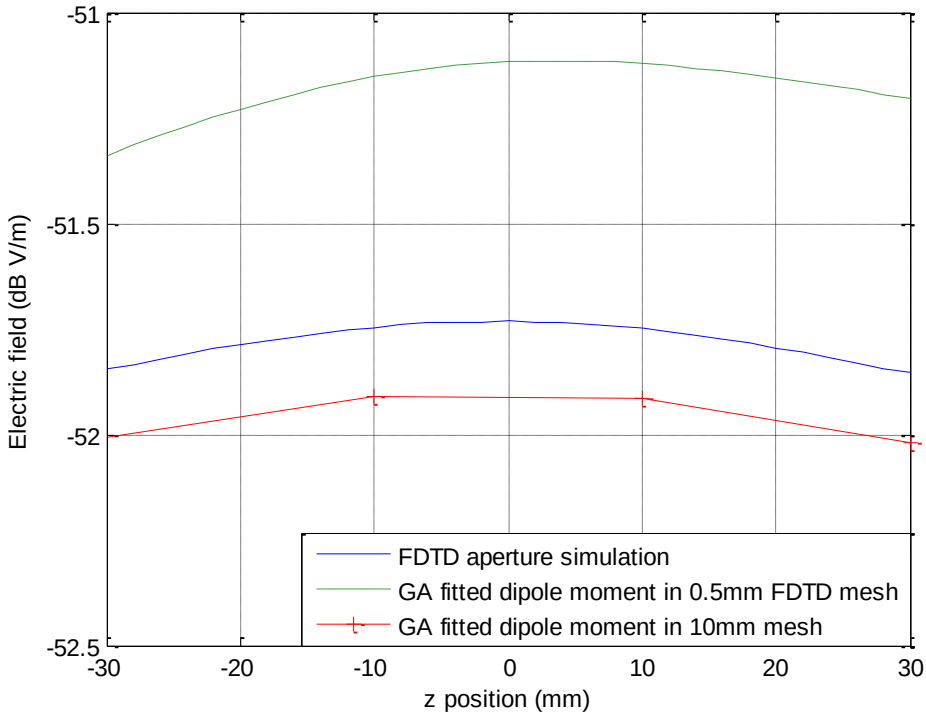

Figure 5.32 *y*-centre line far-field distribution of fine- and coarse-mesh models at 2GHz

Figure 5.33 to 5.35 show the phase of the electric field radiated by the aperture, simulated in an FDTD model and the equivalent dipole moments. Similar errors can be observed to those in the magnitude plots. The overall error in phase is within 10 degrees. Differences in the shapes of the spatial phase distributions can be observed. Again, these differences could be induced by the GA not reaching the bottom of the error landscape, while increasing the number of iteration runs by the GA, or hybridising the GA to another solver could improve the results further.

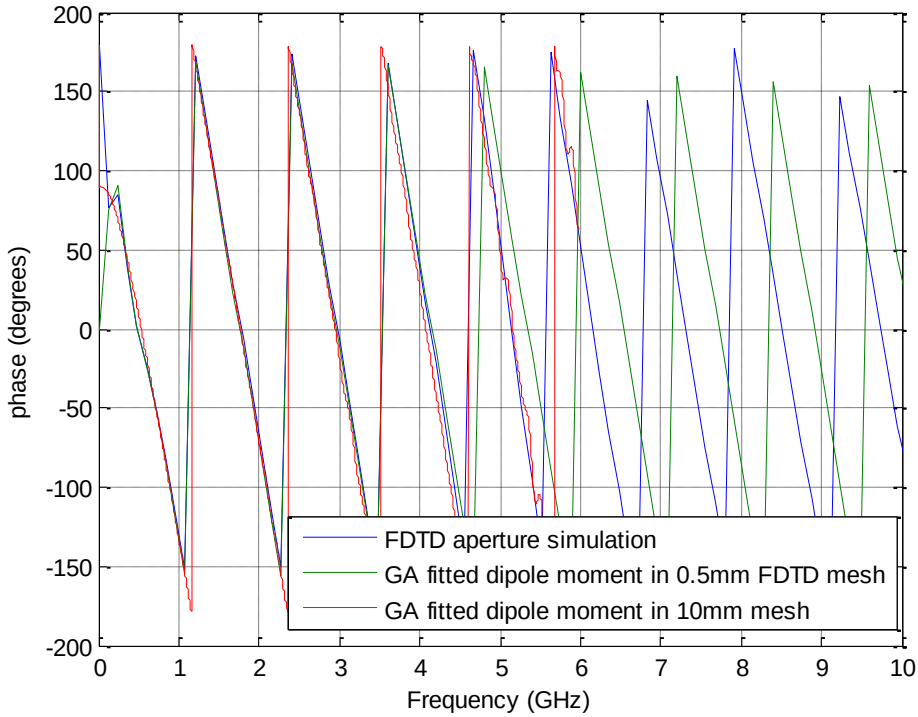

Figure 5.33 Frequency domain phase results of fine- and coarse-grid simulation

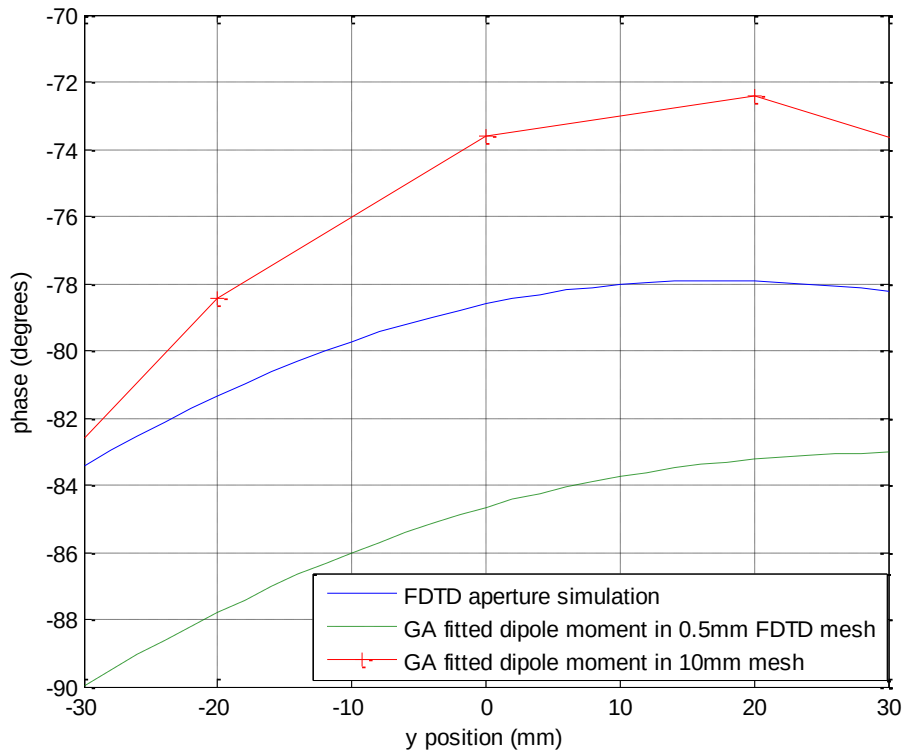

Figure 5.34 *z*-centre line far-field phase distribution of fine- and coarse-mesh models at 2GHz

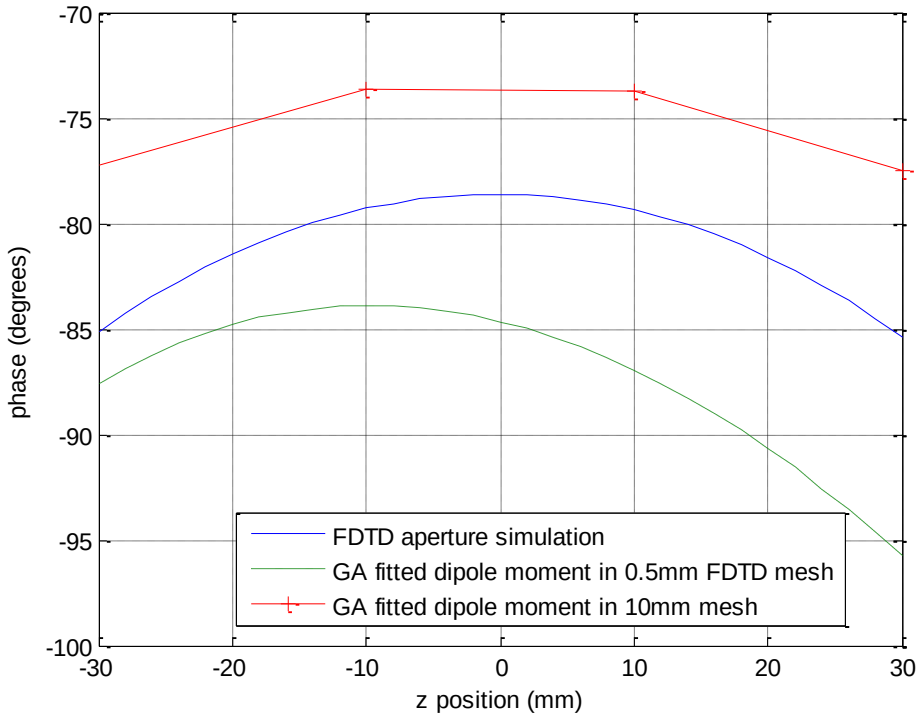

Figure 5.35 *y*-centre line far-field phase distribution of fine- and coarse-mesh models at 2GHz

In summary, the magnitude and phase that the equivalent model produced are considered as satisfactory, as there are a number of factors that limit the modelling accuracy, for example, the contrast of the mesh size between fine- and coarse-grid models and the slow convergence of the GA. The limitations of this modelling method are discussed in more details in the following section.

5.3. Model limitations

In the previous sections, the proposed modelling technique has been proved to be able to model electrically small structures in a macroscopic scaled FDTD mesh, both using simulation and measured data as the source of modelling. However the FDTD mesh and the polarisability approximation have some limitations in the modelling application, such as numerical dispersion and frequency-independent approximation. This section discusses such issues.

5.3.1. Numerical Dispersion in FDTD

The numerical dispersion in FDTD is introduced in Section 1.5.3.2. It is induced by the discretisation of the problem space. In FDTD modelling, it is normally to use mesh size smaller than 1/10 of the shortest wavelength to be simulated to reduce the effect of

numerical dispersion. The numerical dispersion can be reduced but not eliminated; therefore it must be accounted for when evaluating FDTD simulation results.

5.3.2. Error introduced by non-perfect PML boundaries

During the modelling work, it was found that the PML boundary of the FDTD package did not absorb the evanescent wave components well. Significant error was generated by the reflected evanescent wave at close electrical distance. At low frequencies, when the distance between the aperture and output points was a fraction of a wavelength, the effect of the PML not absorbing the evanescent wave was significant, causing phase distortion. An example was made using the following single aperture model with a line of output points, as shown in Figure 5.36, where the excitation was a plane wave of a z-polarised electric field.

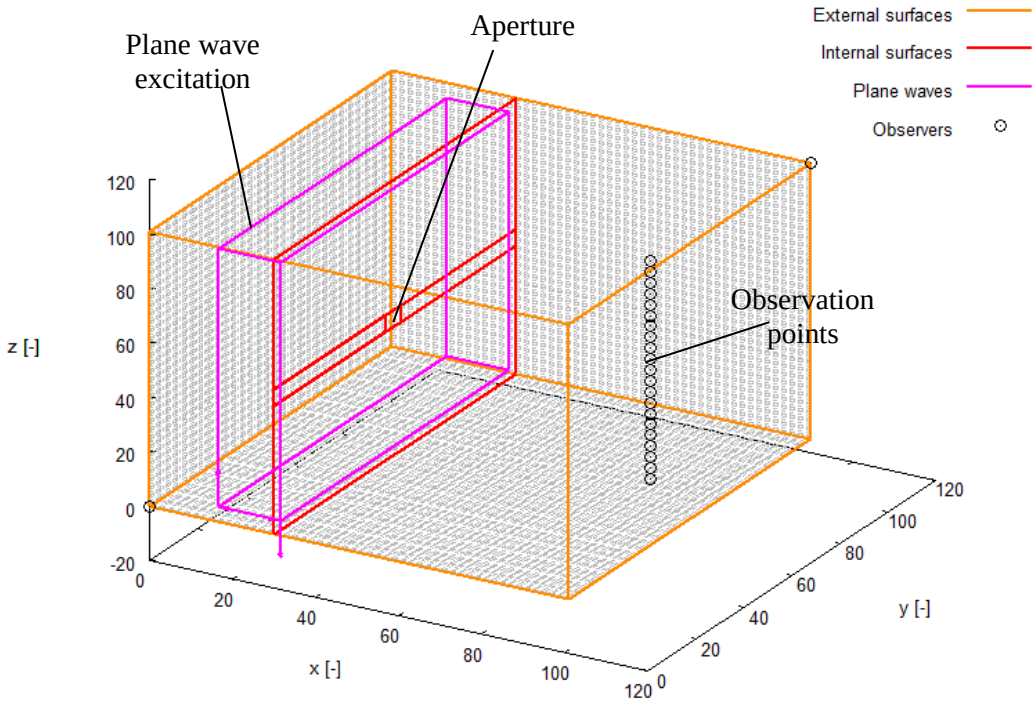

Figure 5.36 Single aperture model for observation of phase of the penetrated field

Figure 5.37 shows the phase of the electric field calculated analytically and simulated by the FDTD method at 1GHz, where the output points were on a plane $\lambda/5$ from the aperture and the simulation boundary was $\lambda/6$ from the aperture. It is clear that at the centre point of the observation plane, where the penetrated field dominates, the phase produced by the two methods agree with each other. However, the phase distortions were greater at the observation points closer to the simulation boundary. Such phase distortion could cause serious error when there were multiple apertures and the fields are added in complex form.

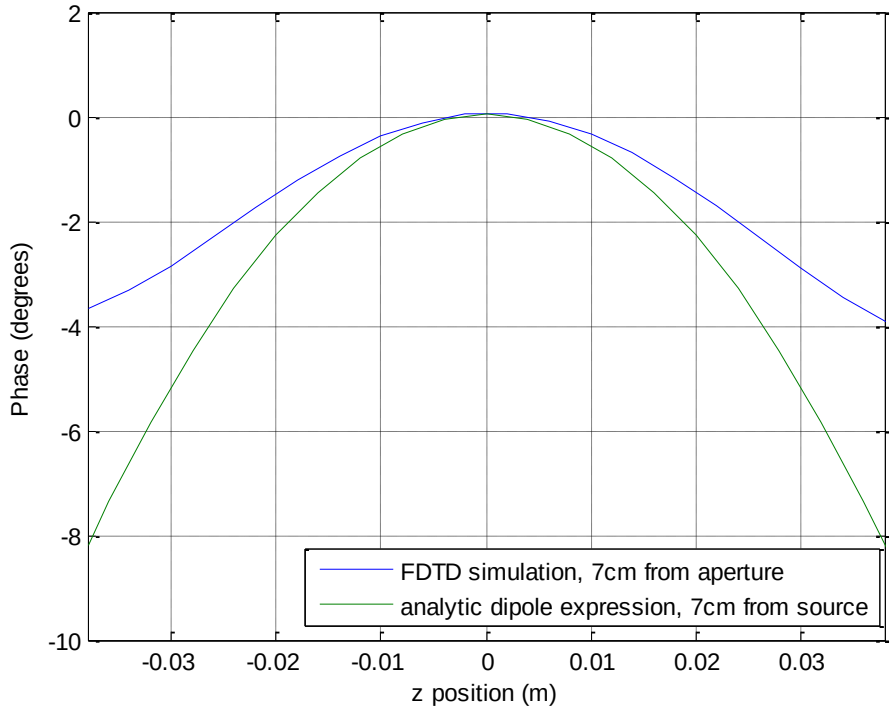

Figure 5.37 Phase of field penetrating the square aperture and radiated by equivalent dipole moment

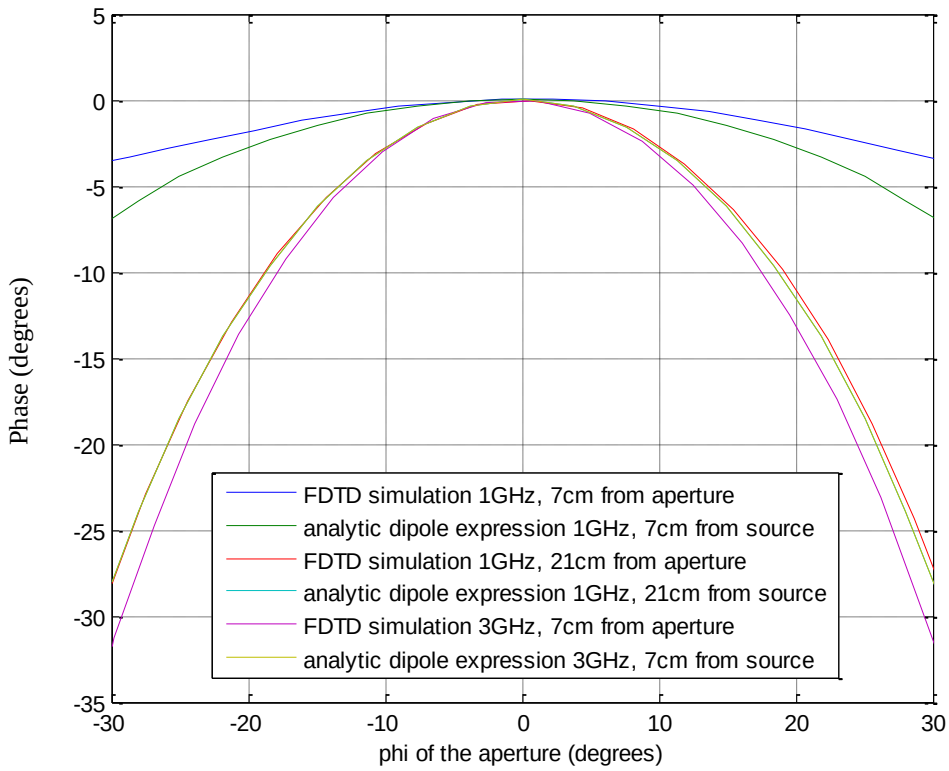

Figure 5.38 Effect on the phase of increasing the electrical distance between the aperture and the measurement surface

Since it was the electrical distance that affected the strength of the evanescent wave, it was considered that increasing the frequency had the same effect as increasing the physical distance between the aperture and output points. Figure 5.38 shows the results of increasing the physical and electrical distances. To make the results produced at 7 cm and 21 cm from the aperture plane comparable, φ of the aperture was used as the horizontal axis instead of distance in millimetres. As expected, the phase distortion was reduced and the FDTD results were close to the analytic calculations. In summary, at close distance, the evanescent field components interacted with the PML boundary and produced phase distortion at locations close to the boundary. The phase distortion could be reduced by increasing the observation frequency so that the electrical distance was increased; or increasing physical distance by taking the observation points further from the boundary and the aperture. In addition, to reduce the evanescent field further, it is suggested that as many layers of PML as possible are used without increasing the computational demand too much.

5.3.3. Frequency-domain limitations

The frequency domain accuracy was affected by two factors. First, the frequency-independent approximation of aperture polarisability was for electrically small apertures. As shown in Section 3.5, this approximation started to lose accuracy when the aperture became electrically large. When the aperture size was comparable to the wavelength, the equivalent dipole approximation was no longer valid as the field across the aperture started resonating. The aperture size was considered to be electrically large when the largest dimension of the aperture became one quarter of the wavelength of the field penetrating it. Figure 5.39 shows the frequency domain results of a 6 $\times$ 6 mm aperture on a 1mm mesh simulation. It is clear that the results start to deviate at about 9 GHz. The frequency at which the aperture is one quarter of the wavelength is 12.5 GHz

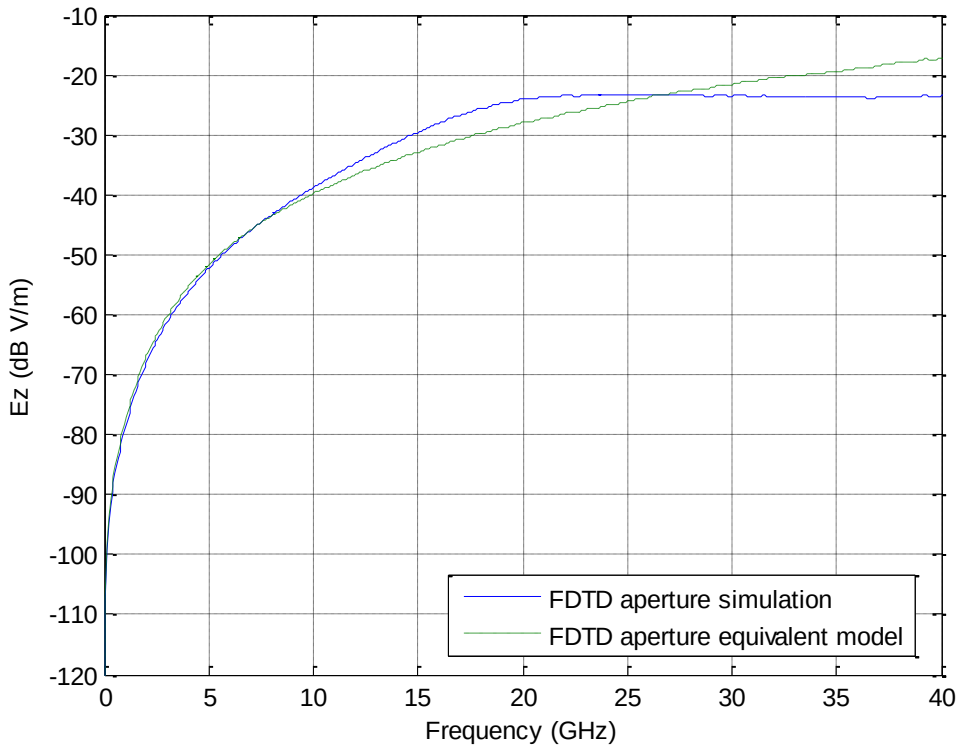

Figure 5.39 Frequency domain responses of aperture simulated in FDTD model and represented by an equivalent dipole

The second limit on the upper frequency limit of the model is given by the mesh size used in the simulation. Due to numerical dispersion, the FDTD mesh can simulate accurately up to the frequency at which the mesh size is $\lambda/10$. At some circumstances where higher accuracy was required, a mesh size of $\lambda/20$ was used. Figure 5.40 shows the frequency domain results of the GA fitted dipole moments using the measured electric field on the slot array shown in Section 5.1. The same dipole moments were applied on a 1 mm mesh grid, and a 25 mm mesh grid. The coarse-grid result was plotted up to the frequency at which the mesh size is $\lambda/5$. It can be seen from 1.2 GHz, at which frequency the mesh size was $\lambda/10$, the coarse mesh simulation started to lose accuracy and ripples were superimposed onto the curve.

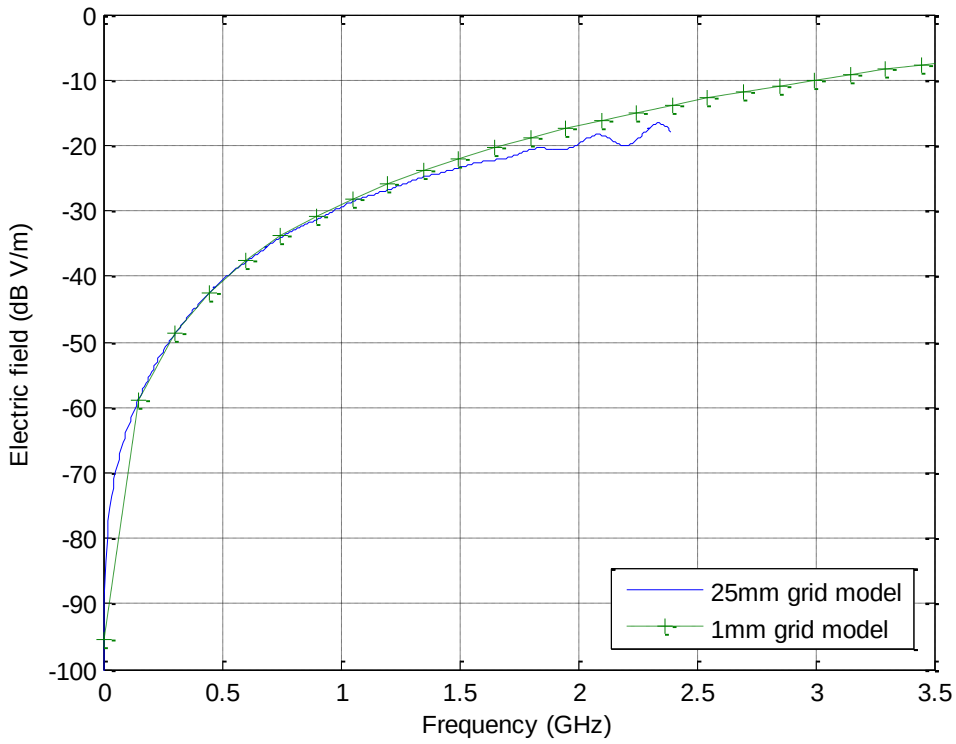

Figure 5.40 Comparison of frequency-domain results of the GA fitted dipole moments from measured field above the slot array on 1mm and 25mm grid models

5.4. Summary

The first two sections of this chapter carried out intensive tests of the modelling method using both measurement and simulated data. Limited by the measurement system, the tests on a more realistic structure were carried out using a simulated near-field. The model has shown good results in frequency and phase in all these tests. For the structure placed off the centre axis of a coarse mesh, the model could still produce accurate results. This was because the displacement was relatively small compared to the distance between the aperture and the observation point of the far-field. In addition, a single dipole moment was able to represent small apertures placed close to each other, such that they could be treated as a single radiating source. More complicated structures require more dipole moments and a longer GA run time.

Numerical dispersion, non-perfect boundaries, loss of accuracy of the low-frequency polarisability approximations, the measurement system and the displacement of field storage positions between fine- and coarse- FDTD meshes all introduced error into the modelling results. Careful design during the modelling of a structure is needed to maintain as high accuracy as possible.

Chapter 6. Conclusions

This thesis has investigated a method of modelling small radiating structures using the FDTD method with a mesh larger than the structure size. A small structure, for example a panel gap on an aircraft, usually has a variable width, plus features such as fasteners and flanges, which make it difficult to model in detail. The proposed modelling method therefore replaces the structure with an equivalent source, which is constructed from an array of dipole moments. This method combines the equivalent surface theory and the approximation of small apertures using radiating dipole moments. An advantage of this technique is that the dipole moments do not need to be placed at the exact location of the radiating structure. It therefore enables us to model unknown structures, provided that the radiated field is available from either measurement or simulation. The hypothesis is that such equivalent sources can be determined using an optimisation method, and the results produced by the equivalent sources in FDTD models are more accurate than direct FDTD simulations of the aperture with a mesh size comparable to the aperture size. A GA is employed as the optimisation method to find these dipole moments using the measured or simulated field radiated by the structure. Then the hypothesis is verified by a number of tests that are carried out in this thesis. The test results have shown that such a modelling method can accurately model small structures in both detailed and macroscopic FDTD meshes.

6.1. Optimisation method

In Chapter 2, the MATLAB GA employed by this research program was proved to be efficient in finding the equivalent dipoles that reproduce the radiated fields of an aperture within 2 dB error. A GA requires properly obtained search bounds and cost functions to operate efficiently. In our case, the search bound derived from the analytic expressions of the fields radiated by the dipole moments; this was done in order to set the search bound as close as possible to the result so that the GA search is made quicker. Accuracy of this estimation is shown in Figure 2.2, where the GA reached the lower part of the error surface within tens of generations.

The cost function is the mean error over the observation plane between fields radiated by the GA fitted dipole and the source field. Section 2.3.3 discusses the GA performance with different dipole moment distributions and cost functions. By increasing the density of dipole moments, a more accurate result can be achieved, although this also increases the computational load. Tests using different cost functions

show that the cost function must be in a complex form so that the phase information is included. The fittings of the dipole moments must also be in a complex form so that the field can be added correctly when there are multiple dipole moments.

The fittings for the DIGIFILT parameter fit the logarithmic magnitude, and phase terms, instead of the real and imaginary part of the parameter. This is because the magnitudes of the DIGIFILT parameters are within the scale of 10^{10}, which is too large a search bound for the GA to find an accurate answer efficiently if the search is in linear magnitude. The GA was also hybridised with a simple descent optimiser during the fitting of the DIGIFILT parameters.

6.2. Measurement system

A 3-D scanning frame was built to carry out automatic planar field scans, as positioning the field probe by hand is inaccurate and the results are hardly repeatable. The scanning results show that the scanning frame can accurately position the probe to within the spatial resolution used by the planar near-field scan of the slot samples. The spatial resolution was limited by the size of the field probes. A 5 mm separation between the measurement points was used in this research program.

An absorber box was used to provide an excitation field to the slot panel. Section 4.4 shows that the excitation is not a plane wave, due to the absorber not working well at the shallow angle of incidence of the field radiating from the horn antenna. A calibration method was developed that by taking the ratio of the field measured above the slot sample to the value taken from the open absorber box measurement. The measurement results in Section 4.4 show that this method can calibrate the measurement so that the results are close to those given by TLM simulations. However, a fraction of the incident field is reflected back from the slot panel into the absorber hole, which is causing the difference shown in Figure 4.21; this interaction is difficult to measure and a calibration method is needed against this effect.

A small dipole, which uses a differential amplifier as the BALUN, was built to function as the electric field probe. The measurements in Section 4.2.1 show that the dipole has good phase balance and cross-polar rejection of the dipole. A small loop was built as the magnetic field probe, although the loop is connected directly to the output without an amplifier. The measurement of the loop phase balance and cross-polar rejection suggests a BALUN may be needed to improve its performance. Therefore, only the electric field was measured and modelled in this research program.

6.3. FDTD modelling results

The FDTD algorithm employed by this modelling work is based on the concept of magnetisation, or dipole moment density. The magnetisation is calculated using the polarisability of the aperture and the mesh size utilised by the model. The radiated field next to the aperture is then added to the original field in the FDTD grid as if the aperture was closed. The model is therefore implemented as a soft field source in the FDTD method.

Throughout this research program, this method of representing an equivalent magnetic dipole by magnetisation has proved to be accurate both in detailed models and macro models of the apertures at frequencies where the apertures are considered as electrically small. Since the field is forwarded instantaneously by the distance of one mesh size in this method, and since the location of excitation is different between fine- and coarse-grid simulations, a phase correction method was developed to validate the coarse grid results against the detailed simulations. The phase correction requires the phases of the two simulations to be referenced to the same point spatially, so the corrected results are comparable. However, real applications of the model may not require such a process, as the excitation comes from the adjacent mesh with known phase information. The error produced by the FDTD model of the aperture is less than 3 dB in magnitude and less than 10 degrees in phase. As mentioned in Section 3.6.2, the location at which the dipole moments are excited could be different between the coarse- and fine-grid meshes depending on the mesh size, contributing to the error. In addition, the fine-grid simulations used to provide validation results for the coarse-grid models used a large amount of meshes. Since the effect of numerical dispersion increases with the number of meshes used in the model, the error caused by this must be accounted for when evaluating the results.

In the frequency domain, the upper frequency at which the model works is limited by two factors. The first of these is the aperture size: Figure 3.8 shows the frequency of independent polarisability is only valid when the aperture is electrically small, in which case the largest dimension of the aperture is shorter than one quarter of the wavelength to be simulated. Secondly, the FDTD simulation starts to lose accuracy when the mesh size is larger than $\lambda/10$. This is due to numerical dispersion caused by the discretisation of the simulation. Within the frequency range defined by these two factors, this model has shown good accuracy.

Spatially, it was found that the PML boundary of the FDTD package does not absorb the evanescent wave well in the reactive near-field. In fact, the reflected evanescent wave interferes with the wave penetrating the aperture and induces phase distortion. Such phase distortion could cause error when the fields from multiple apertures are added up. It has been shown that keeping the output points at least $\lambda/6$ from the simulation boundary, and at least $\lambda/4$ from the radiating structure can significantly reduce the error caused by this effect so that it can be ignored. It is also suggested that as many layers of PML as possible are used, without increasing the computational load significantly, so that the evanescent wave is absorbed further.

The DIGIFILT module was also used to model small apertures. DIGIFILT represents the reflection and transmission characteristics of the object with a reflection and transmission impedance matrix. Unlike the magnetisation method, DIGIFILT can produce frequency-dependent characteristics of the aperture; however more effort is required to obtain the filter parameters. DIGIFILT has been verified to be capable of modelling small apertures on a mesh much larger than in Section 3.7. However, more investigation of DIGIFILT's capability is needed.

6.4. Further work

The equivalent source modelling method for FDTD simulation has shown to produce satisfactory results. However, it is tested using a single polarisation plane wave. Other polarisations should be implemented and the equivalent electric field dipole which represents the normal electric field should be investigated. This modelling method is proved to work as expected, with properly built interface, it will act as part of a full-aircraft simulation framework and provide the penetrated field of electrically small apertures. To make the model work more effectively and accurately, there are some suggestions for further improvements:

The GA is able to accurately find the dipole moment that reproduces the radiated field from the apertures. However, the locations of the dipole moments are pre-assigned, and all the dipole moments are stored in the results. In the future, mechanisms for locating the dipole moments that depend on mesh and field geometries should be developed. In addition, algorithms that disable the dipole moment when its contribution to the result becomes insignificant will help improve the efficiency of the modelling even further.

From the measurement point of view, a better magnetic field probe needs to be designed and built. As stated in Chapter 4, there are a number of imperfections in the current measurement system, such as the incident field to the slot sample not being clearly determined. A calibration method is needed to determine the actual field illuminating the slot sample on the absorber box. Furthermore, methods to reduce error caused by noise, diffraction and probe disturbance to the field would make the measurement result more accurate.

Reproducing the frequency-dependent behaviours of the object is also important in future modelling work. One solution would be to divide the frequency domain into segments and fit polarisability to each segment individually. The points to be improved that are mentioned in this section will refine the model with better computational efficiency and produce more comprehensive output.

In summary, this macro-model of electrically small apertures requires less knowledge of the details of the structures as it provides an equivalent model instead of a detailed model. The sub-cellular modelling method also means the small structure can be modelled using the same mesh size as other parts of the aircraft, therefore reducing the computational load. The test cases shown in Chapter 5 prove that this modelling method has good accuracy in terms of both magnitude and phase. With all the improvements mentioned above, this model will bring better accuracy and efficiency to full-aircraft simulation for EMC performance. As the demand simulating aircraft EMC performance for certification and design purposes increases, this model will contribute to the aviation industry by reducing the computation load required by full-aircraft simulation, while maintaining accuracy.

Appendix I. Transform analytic expression of radiated field from electric dipole moment from e^{ikr} phasor notation to e^{-jkr} notation

The analytic calculation of radiated fields from electric and magnetic dipole moments mentioned in this thesis is uses MATLAB code which is based on a set of vector expressions that calculate the radiated fields using dipole moments [1]. These equations are:

Electric dipole moment:

$$\mathbf{E} = \frac{1}{4\pi\varepsilon_0}\left\{k^2(\hat{\mathbf{r}}\times\mathbf{p})\times\hat{\mathbf{r}}\frac{e^{ikr}}{r} + \left[3\hat{\mathbf{r}}(\hat{\mathbf{r}}\cdot\mathbf{p})-\mathbf{p}\right]\left(\frac{1}{r^3}-\frac{ik}{r^2}\right)e^{ikr}\right\}$$

$$\mathbf{H} = -\frac{ck^2}{4\pi}(\hat{\mathbf{r}}\times\mathbf{p})\frac{e^{ikr}}{r}\left(1-\frac{1}{ikr}\right)$$

Magnetic dipole moment:

$$\mathbf{E} = -\frac{\eta_0}{4\pi}k^2(\hat{\mathbf{r}}\times\mathbf{m})\frac{e^{ikr}}{r}\left(1-\frac{1}{ikr}\right)$$

$$\mathbf{H} = \frac{1}{4\pi}\left\{k^2(\hat{\mathbf{r}}\times\mathbf{m})\times\hat{\mathbf{n}}\frac{e^{ikr}}{r} + \left[3\hat{\mathbf{r}}(\hat{\mathbf{r}}\cdot\mathbf{m})-\mathbf{m}\right]\left(\frac{1}{r^3}-\frac{ik}{r^2}\right)e^{ikr}\right\}$$

Where

***E**:* radiated electric field

***H**:* radiated magnetic field

k: wave number

c: speed of light

***p**:* electric dipole moment

***m**:* magnetic dipole moment

r: magnitude of distance between dipole moment and the observation point

η_0*:* impedance of free space

$\hat{\boldsymbol{r}}$: unit vector pointing from the dipole moment to the observation point

The above expressions are from a book that uses the $e^{i\omega t}$ phasor notation. In order to use them in our application, they need to be compatible with other expressions used here, thus they need to be converted to the $e^{-j\omega t}$ phasor notation.

The expression of electric field radiated by electric dipole moment using $e^{i\omega t}$ phasor is:

$$\mathbf{E} = \frac{1}{4\pi\varepsilon_0}\left\{k^2(\hat{\mathbf{r}}\times\mathbf{p})\times\hat{\mathbf{r}}\frac{e^{ikr}}{r} + \left[3\hat{\mathbf{r}}(\hat{\mathbf{r}}\cdot\mathbf{p})-\mathbf{p}\right]\left(\frac{1}{r^3}-\frac{ik}{r^2}\right)e^{ikr}\right\}$$

To make such a conversion, replace $i \rightarrow -j$: to get the equation in $e^{-j\omega t}$ convention:

$$\mathbf{E} = \frac{1}{4\pi\varepsilon_0}\left\{k^2(\hat{\mathbf{r}}\times\mathbf{p})\times\hat{\mathbf{r}}\frac{e^{-jkr}}{r} + \left[3\hat{\mathbf{r}}(\hat{\mathbf{r}}\cdot\mathbf{p})-\mathbf{p}\right]\left(\frac{1}{r^3}+\frac{jk}{r^2}\right)e^{-jkr}\right\}$$

The same modifications are made on other equations in this set.

Verification of the transformation

The electric dipole moment is given by:

$$\mathbf{p} = \frac{I\,\mathbf{dl}}{j\omega} = \frac{\mathbf{J}_s\,\mathrm{d}l^2}{j\omega} = \frac{\mathbf{J}\,\mathrm{d}l^3}{j\omega}$$

Where dl is the size of the electric dipole moment, which in our case is the TLM or FDTD mesh size, $\boldsymbol{J}_s$ is the surface current density and $\boldsymbol{J}$ is the volumetric current density.

Substituting **p** into the expression:

$$\boldsymbol{E} = \frac{k^2 e^{-jkr}}{4\pi\varepsilon_0 r}\frac{I_m dl}{j\omega}\left\{(\hat{\mathbf{r}}\times\hat{\mathbf{z}})\times\hat{\mathbf{r}} + \left[3\hat{\mathbf{r}}(\hat{\mathbf{r}}\cdot\hat{\mathbf{z}})-\hat{\mathbf{z}}\right]\left(\frac{1}{k^2r^2}+\frac{j}{kr}\right)\right\}$$

Where $\hat{\mathbf{z}}$ the unit vector of the direction that p points to. Transforming $\hat{\boldsymbol{z}}$ to the spherical coordinate system:

$$\hat{\mathbf{z}} = \hat{\mathbf{r}}\cos\theta - \hat{\boldsymbol{\theta}}\sin\theta$$

The cross product

$$(\hat{\mathbf{r}} \times \hat{\mathbf{z}}) \times \hat{\mathbf{r}} = \hat{\mathbf{r}} \times (\hat{\mathbf{r}}\cos\theta - \hat{\boldsymbol{\theta}}\sin\theta) \times \hat{\mathbf{r}} = -\hat{\boldsymbol{\theta}}\sin\theta$$

And

$$[3\hat{\mathbf{r}}(\hat{\mathbf{r}} \cdot \hat{\mathbf{z}}) - \hat{\mathbf{z}}] = 3\hat{\mathbf{r}}(|\hat{\mathbf{r}}||\hat{\mathbf{z}}|\cos\theta) - \hat{\mathbf{r}}\cos\theta + \hat{\boldsymbol{\theta}}\sin\theta = 2\hat{\mathbf{r}}\cos\theta + \hat{\boldsymbol{\theta}}\sin\theta$$

Replacing $(\hat{\mathbf{r}} \times \hat{\mathbf{z}}) \times \hat{\mathbf{r}}$ and $[3\hat{\mathbf{r}}(\hat{\mathbf{r}} \cdot \hat{\mathbf{z}}) - \hat{\mathbf{z}}]$ terms, the expression becomes:

$$\boldsymbol{E} = \frac{k^2 e^{-jkr}}{4\pi\varepsilon_0 r}\frac{Idl}{j\omega}\left\{-\hat{\boldsymbol{\theta}}\sin\theta + (2\hat{\mathbf{r}}\cos\theta + \hat{\boldsymbol{\theta}}\sin\theta)\left(\frac{1}{k^2r^2} + \frac{j}{kr}\right)\right\}$$

Taking θ component of the E field:

$$E_\theta = \frac{k^2 e^{-jkr}}{4\pi\varepsilon_0 r}\frac{Idl\sin\theta}{j\omega}\left\{-1 + \frac{1}{k^2r^2} + \frac{j}{kr}\right\}$$

$$E_\theta = j\frac{k^2 e^{-jkr}}{4\pi\varepsilon_0 r}\frac{Idl\sin\theta}{\omega}\left\{1 - \frac{1}{k^2r^2} + \frac{1}{jkr}\right\}$$

Since $k = \frac{2\pi}{\lambda} = \frac{2\pi f}{c}$, $\omega = 2\pi f$:

$$E_\theta = j\frac{ke^{-jkr}}{4\pi\varepsilon_0 r}\frac{Idl\sin\theta}{2\pi f}\frac{2\pi f}{c}\left\{1 - \frac{1}{k^2r^2} + \frac{1}{jkr}\right\}$$

$$E_\theta = j\frac{kIdl\sin\theta e^{-jkr}}{4\pi r\varepsilon_0 c}\left\{1 - \frac{1}{k^2r^2} + \frac{1}{jkr}\right\}$$

$$\eta_0 = \mu_0 c_0 = \frac{1}{\varepsilon_0 c_0}$$

Then:

$$E_\theta = j\frac{\eta_0 kI\Delta l\sin\theta e^{-jkr}}{4\pi r}\left\{1 - \frac{1}{k^2r^2} + \frac{1}{jkr}\right\}$$

Which yields the equation in [2]:

$$E_\theta = j\eta_0\frac{kI_0\sin\theta}{4\pi r}\left[1 + \frac{1}{jkr} - \frac{1}{(kr)^2}\right]$$

A Similar simplification can be done for the r component:

$$\mathbf{E} = \frac{1}{4\pi\varepsilon_0}\left\{k^2(\hat{\mathbf{r}}\times\mathbf{p})\times\hat{\mathbf{r}}\frac{e^{-jkr}}{r} + \left[3\hat{\mathbf{r}}(\hat{\mathbf{r}}\cdot\mathbf{p})-\mathbf{p}\right]\left(\frac{1}{r^3}+\frac{jk}{r^2}\right)e^{-jkr}\right\}$$

Taking r component of the above expression:

$$E_r = \frac{k^2 e^{-jkr}}{4\pi\varepsilon_0 r}\frac{I\Delta l}{j\omega}\left\{2\cos\theta\left(\frac{1}{k^2r^2}+\frac{j}{kr}\right)\right\}$$

$$E_r = j\frac{\eta_0 kIdl\cos\theta e^{-jkr}}{2\pi\varepsilon_0 r}\left\{\frac{1}{jkr}-\frac{1}{k^2r^2}\right\}$$

$$E_r = \frac{\eta_0 Idl\cos\theta e^{-jkr}}{2\pi r^2}\left\{1-\frac{jkr}{k^2r^2}\right\}$$

$$E_r = \frac{\eta_0 Idl\cos\theta e^{-jkr}}{2\pi r^2}\left\{1+\frac{1}{jkr}\right\}$$

Strength of TLM Source

The above expressions were tested using a single-node TLM excitation model, and with equivalent excitation current of a TLM cell as:

$$I_0 = \frac{E_0\,\mathrm{d}l}{\eta_0}$$

Where E_0 is the excitation electric field strength, dl is the cell size, and η_0 is the impedance of free space.

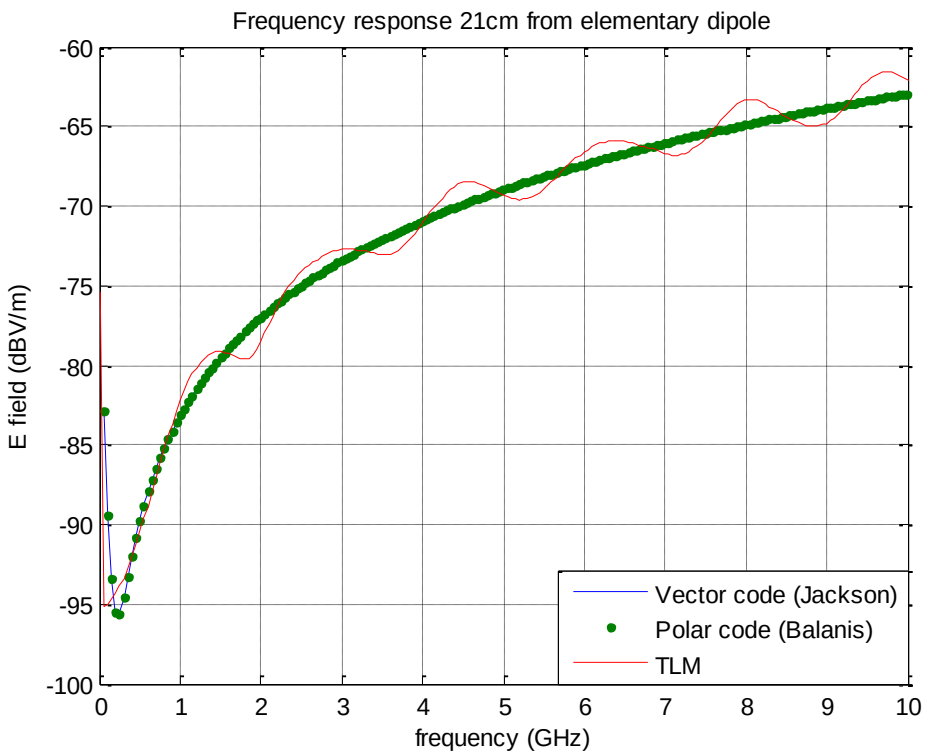

Figure I.1 Frequency response of the elementary dipole

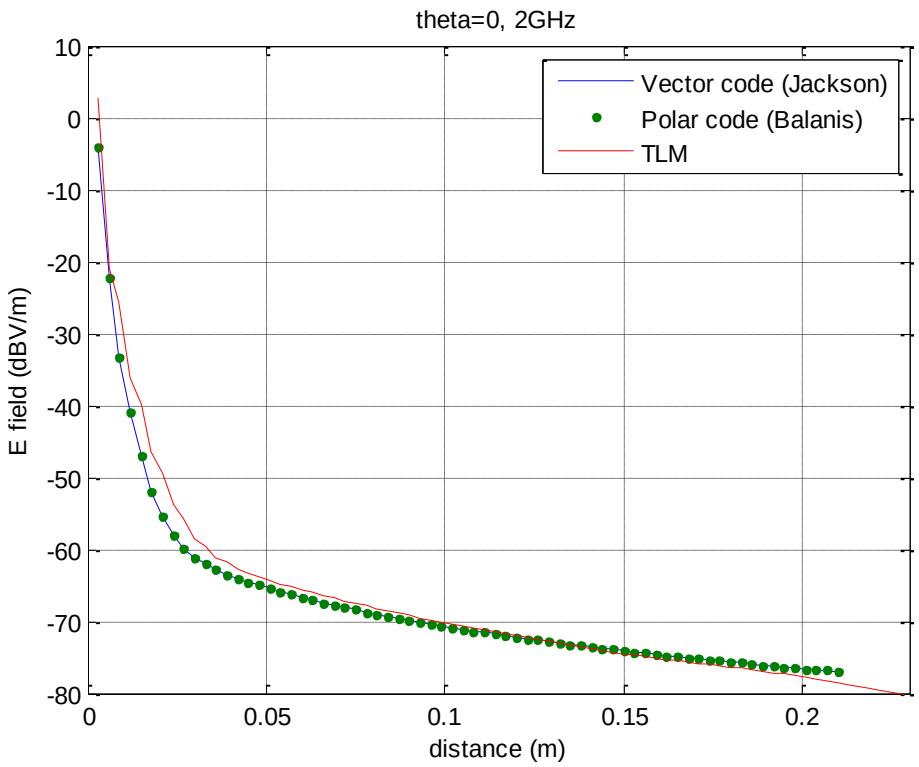

Figure I.2 Results of radiated field from an elementary dipole at 2GHz

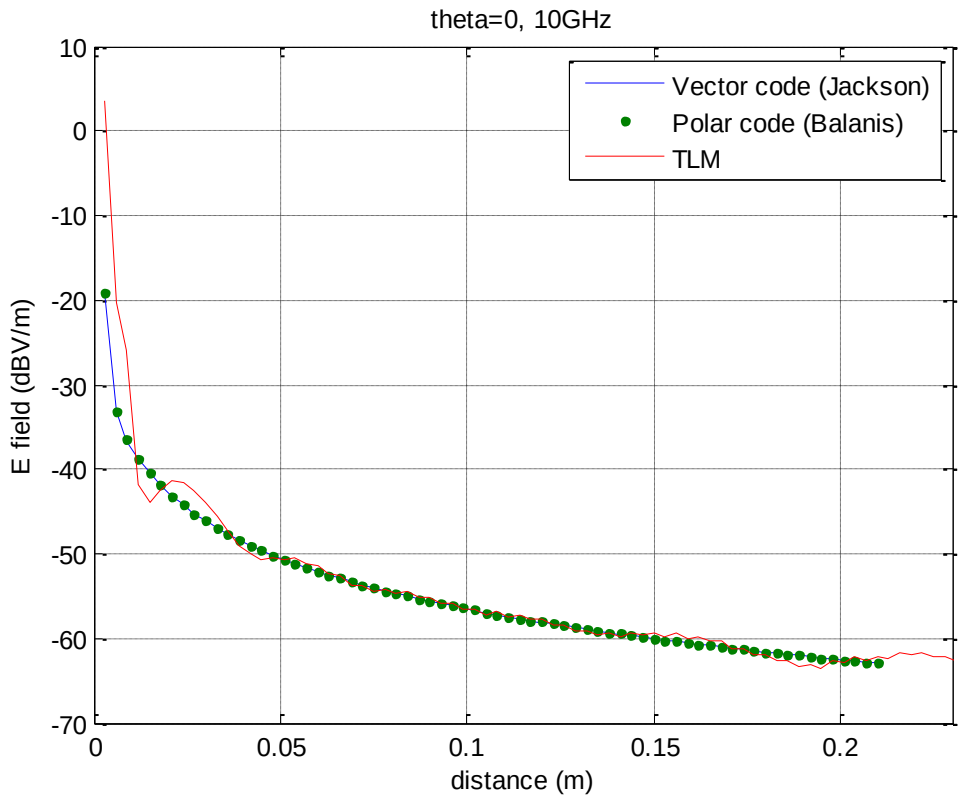

Figure I.3 Results of radiated field from an elementary dipole at 2GHz

The three methods employed here produce the same results, with ripple superimposed on the TLM result due to the truncation of the wave front at the simulation boundary. The test is carried out at 2 GHz and 10 GHz and they have good agreement.

[1] J. Jackson, Classic Electromagnetics, 3rd Edition, John Wiley & Sons, Inc. pp 411-413

[2] C. A. Balanis, 'Antenna Theory, Analysis and Design 2nd Edition'. John Wiley & Sons, Inc.,1997. pp620-625.

Appendix II. Transform analytic expression of radiated field from magnetic dipole moment from from e^{ikr} phasor notation to e^{-jkr} notation

In TLM, a single node excitation of electric field would give an electric current as $I_e = \varepsilon_0 E_0 \Delta l c_0$

By using the duals between electric and magnetic fields, the magnetic current I_m of a single node magnetic field excitation in TLM is $I_m = \mu_0 H_0 \Delta l c_0$

Where Δl is the mesh size, c_0 is the speed of light in free space, μ_0 is the permittivity of free space and ε_0 is the permeability of free space.

Jackson gives radiated magnetic field of a magnetic dipole moment as:

$$\boldsymbol{H} = \frac{1}{4\pi}\left\{k^2(\hat{\mathbf{r}}\times\mathbf{m})\times\hat{\mathbf{r}}\frac{e^{ikr}}{r} + [3\hat{\mathbf{r}}(\hat{\mathbf{r}}\cdot\mathbf{m})-\mathbf{m}]\left(\frac{1}{r^3}-\frac{jk}{r^2}\right)e^{ikr}\right\}$$

Converted to the e^{-jkr} phasor:

$$\boldsymbol{H} = \frac{1}{4\pi}\left\{k^2(\hat{\mathbf{r}}\times\mathbf{m})\times\hat{\mathbf{r}}\frac{e^{-jkr}}{r} + [3\hat{\mathbf{r}}(\hat{\mathbf{r}}\cdot\mathbf{m})-\mathbf{m}]\left(\frac{1}{r^3}+\frac{jk}{r^2}\right)e^{-jkr}\right\}$$

Where r is the distance between $\boldsymbol{m}$ and observation point P, $\hat{\boldsymbol{r}}$ is a unit vector pointing from the dipole moment to the observation point, $\boldsymbol{m}$ is the magnetic dipole moment, k is wave number and $\boldsymbol{H}$ is the radiated magnetic field

Starting from Jackson's expression [1]:

$$\boldsymbol{H} = \frac{1}{4\pi}\left\{k^2(\hat{\mathbf{r}}\times\mathbf{m})\times\hat{\mathbf{r}}\frac{e^{-jkr}}{r} + [3\hat{\mathbf{r}}(\hat{\mathbf{r}}\cdot\mathbf{m})-\mathbf{m}]\left(\frac{1}{r^3}+\frac{jk}{r^2}\right)e^{-jkr}\right\}$$

Moving $\frac{k^2 e^{-jkr}}{r}$ out of the bracket:

$$\boldsymbol{H} = \frac{k^2 e^{-jkr}}{4\pi r}\left\{(\hat{\mathbf{r}}\times\mathbf{m})\times\hat{\mathbf{r}} + [3\hat{\mathbf{r}}(\hat{\mathbf{r}}\cdot\mathbf{m})-\mathbf{m}]\left(\frac{1}{k^2r^2}+\frac{j}{kr}\right)\right\}$$

Since **m** is polarised along z-axis,

$$\mathbf{m} = m\hat{\mathbf{z}}$$

$$m = \frac{I_m \Delta l}{j\omega\mu_0}$$

$$\mathbf{m} = \frac{I_m \Delta l}{j\omega\mu_0}\hat{\mathbf{z}}$$

Substituting **m** into the expression:

$$\boldsymbol{H} = \frac{k^2 e^{-jkr}}{4\pi r}\frac{I_m \Delta l}{j\omega\mu_0}\left\{(\hat{\mathbf{r}}\times\hat{\mathbf{z}})\times\hat{\mathbf{r}} + \left[3\hat{\mathbf{r}}(\hat{\mathbf{r}}\cdot\hat{\mathbf{z}}) - \hat{\mathbf{z}}\right]\left(\frac{1}{k^2 r^2} + \frac{j}{kr}\right)\right\}$$

Transforming $\hat{\boldsymbol{z}}$ to the spherical coordinate system:

$$\hat{\mathbf{z}} = \hat{\mathbf{r}}\cos\theta - \hat{\boldsymbol{\theta}}\sin\theta$$

The cross product

$$(\hat{\mathbf{r}}\times\hat{\mathbf{z}})\times\hat{\mathbf{r}} = \hat{\mathbf{r}}\times\left(\hat{\mathbf{r}}\cos\theta - \hat{\boldsymbol{\theta}}\sin\theta\right)\times\hat{\mathbf{r}} = -\hat{\boldsymbol{\theta}}\sin\theta$$

And

$$\left[3\hat{\mathbf{r}}(\hat{\mathbf{r}}\cdot\hat{\mathbf{z}}) - \hat{\mathbf{z}}\right] = 3\hat{\mathbf{r}}\left(|\hat{\mathbf{r}}||\hat{\mathbf{z}}|\cos\theta\right) - \hat{\mathbf{r}}\cos\theta + \hat{\boldsymbol{\theta}}\sin\theta = 2\hat{\mathbf{r}}\cos\theta + \hat{\boldsymbol{\theta}}\sin\theta$$

Replacing $(\hat{\mathbf{r}}\times\hat{\mathbf{z}})\times\hat{\mathbf{r}}$ and $\left[3\hat{\mathbf{r}}(\hat{\mathbf{r}}\cdot\hat{\mathbf{z}}) - \hat{\mathbf{z}}\right]$ terms, the expression becomes:

$$\boldsymbol{H} = \frac{k^2 e^{-jkr}}{4\pi r}\frac{I_m \Delta l}{j\omega\mu_0}\left\{-\hat{\boldsymbol{\theta}}\sin\theta + \left(2\hat{\mathbf{r}}\cos\theta + \hat{\boldsymbol{\theta}}\sin\theta\right)\left(\frac{1}{k^2 r^2} + \frac{j}{kr}\right)\right\}$$

Taking θ component of the H field:

$$H_\theta = \frac{k^2 e^{-jkr}}{4\pi r}\frac{I_m \Delta l\sin\theta}{j\omega\mu_0}\left\{-1 + \frac{1}{k^2 r^2} + \frac{j}{kr}\right\}$$

$$H_\theta = j\frac{k^2 e^{-jkr}}{4\pi r}\frac{I_m \Delta l\sin\theta}{\omega\mu_0}\left\{1 - \frac{1}{k^2 r^2} + \frac{1}{jkr}\right\}$$

Since $k = \frac{2\pi}{\lambda} = \frac{2\pi f}{c}$, $\omega = 2\pi f$:

$$H_\theta = j\frac{ke^{-jkr}}{4\pi r}\frac{I_m \Delta l \sin\theta}{2\pi f \mu_0}\frac{2\pi f}{c}\left\{1-\frac{1}{k^2r^2}+\frac{1}{jkr}\right\}$$

$$H_\theta = j\frac{kI_m \Delta l \sin\theta e^{-jkr}}{4\pi r \mu_0 c}\left\{1-\frac{1}{k^2r^2}+\frac{1}{jkr}\right\}$$

$$\eta_0 = \mu_0 c_0 = \frac{1}{\varepsilon_0 c_0}$$

Then:

$$H_\theta = j\frac{kI_m \Delta l \sin\theta e^{-jkr}}{4\pi r \eta_0}\left\{1-\frac{1}{k^2r^2}+\frac{1}{jkr}\right\}$$

Which yields the equation in Balanis [2].

$$H_\theta = j\frac{kI_m l \sin\theta}{4\pi\eta_0 r}\left[1+\frac{1}{jkr}-\frac{1}{(kr)^2}\right]e^{-jkr}$$

Similar simplification can be done for the r component:

$$H = \frac{k^2e^{-jkr}}{4\pi r}\frac{I_m \Delta l}{j\omega\mu_0}\left\{-\hat{\boldsymbol{\theta}}\sin\theta + \left(2\hat{\mathbf{r}}\cos\theta + \hat{\boldsymbol{\theta}}\sin\theta\right)\left(\frac{1}{k^2r^2}+\frac{j}{kr}\right)\right\}$$

Taking r component of the above expression:

$$H_r = \frac{k^2e^{-jkr}}{4\pi r}\frac{I_m \Delta l}{j\omega\mu_0}\left\{2\cos\theta\left(\frac{1}{k^2r^2}+\frac{j}{kr}\right)\right\}$$

$$H_r = j\frac{kI_m \Delta l \cos\theta e^{-jkr}}{2\pi r \eta_0}\left\{\frac{1}{jkr}-\frac{1}{k^2r^2}\right\}$$

$$H_r = \frac{kI_m \Delta l \cos\theta e^{-jkr}}{2\pi r^2 \eta_0}\left\{1-\frac{jkr}{k^2r^2}\right\}$$

$$H_r = \frac{kI_m \Delta l \cos\theta e^{-jkr}}{2\pi r^2 \eta_0}\left\{1+\frac{1}{jkr}\right\}$$

Again, a TLM single-node excitation of magnetic field is used to verify the above conversions:

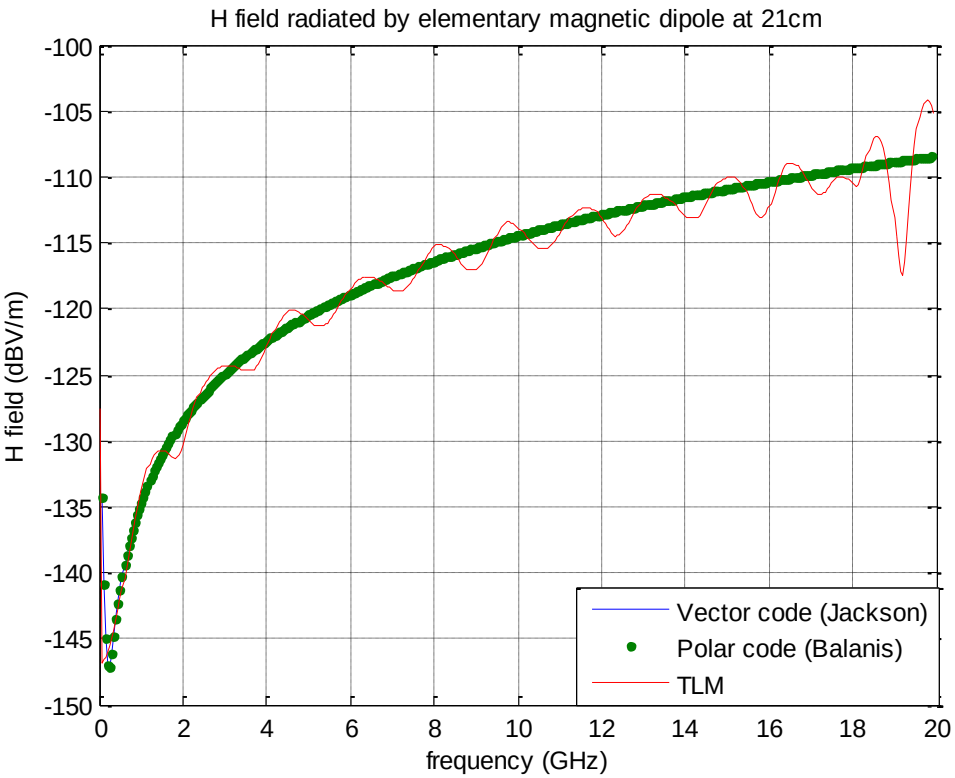

Figure II.1 Frequency response of the elementary magnetic dipole

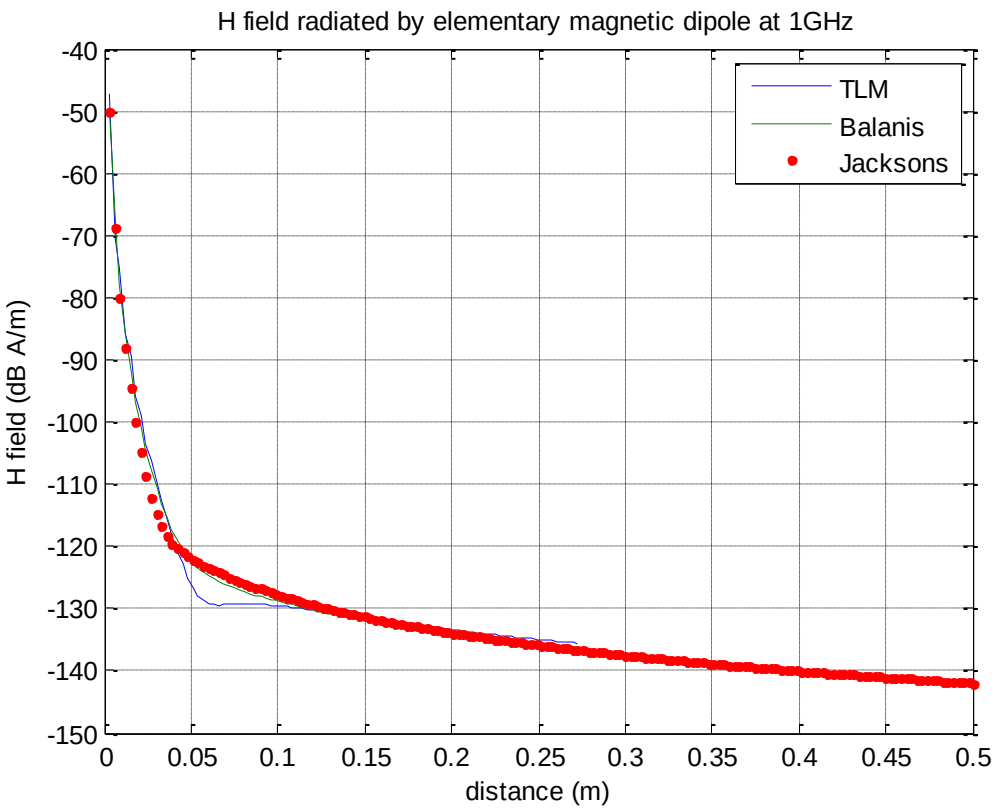

Figure II.2 Comparison of radiated field from 0 to 0.5m at 1GHz

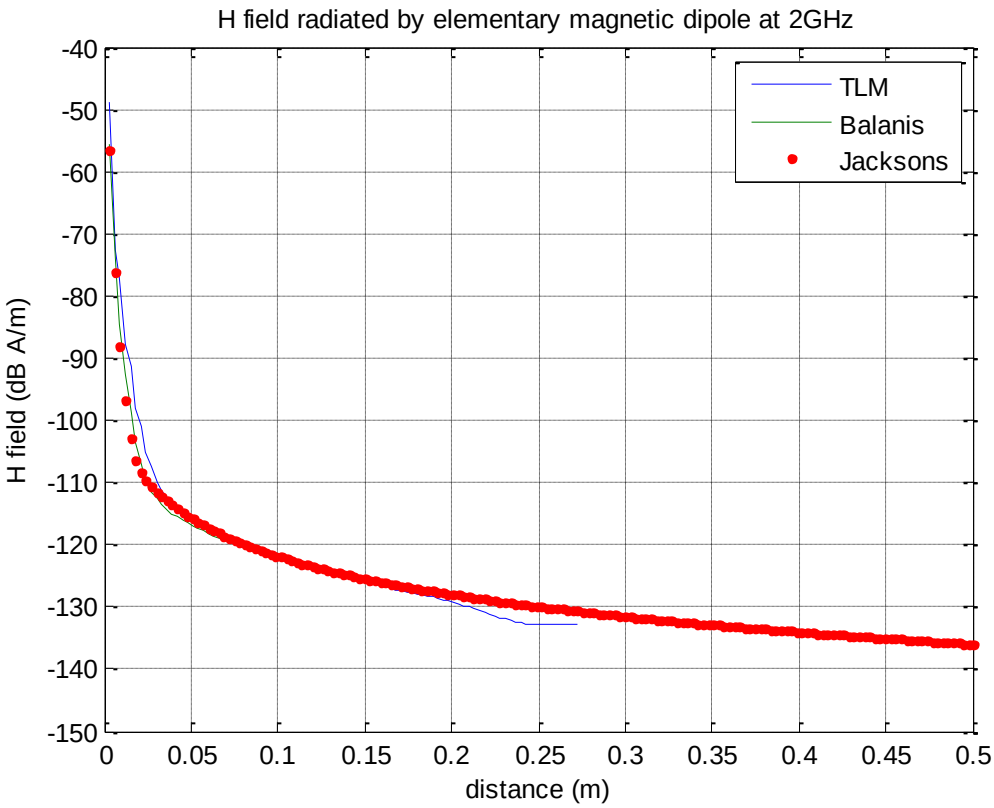

Figure II.3 Comparison of radiated field from 0 to 0.5m at 2GHz

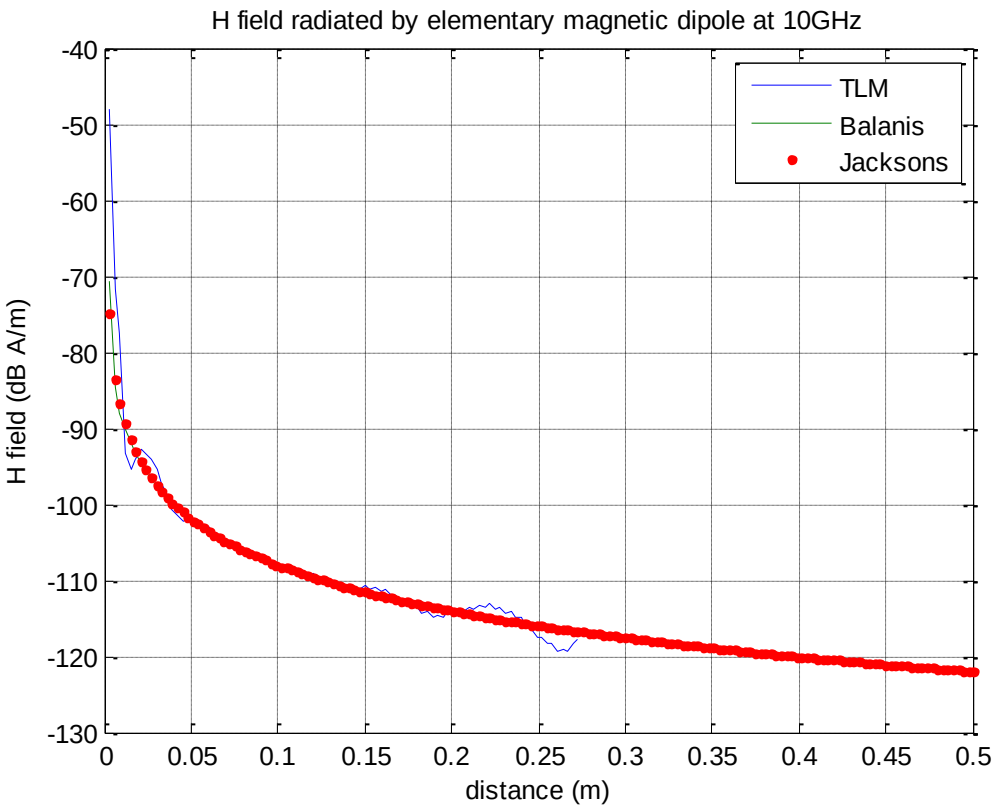

Figure II.4Comparison of radiated field from 0 to 0.5m at 10GHz

The above figures show good agreements between the results produced by the MATLAB codes based on the analytical expressions and TLM simulations. The ripples on the TLM results are induced by the truncation of wave front at the simulation boundaries, which generates secondary waves at the boundary that contribute to these ripples.

[1] J. Jackson, Classic Electromagnetics, 3rd Edition, John Wiley & Sons, Inc. pp 411-413

[2] C. A. Balanis, 'Antenna Theory, Analysis and Design 2nd Edition'. John Wiley & Sons, Inc.,1997. pp620-625.

Appendix III. Equivalent circuit of an electric dipole using frequency independent lumped elements

A dipole can be represented by the equivalent R-L-C circuit shown below [1]. An analytic calculation of the dipole input impedance involves integrating the current distribution across the dipole length which is hard to obtain. Normally the current distribution is approximated as constant for an infinitesimal dipole or sinusoidal distribution for half-wavelength dipole [2], but an analytical derivation of the current distribution is too complicated and rarely used. The equivalent circuit of a dipole offers an easier method to calculate the input impedance of the dipole compared to deriving the impedance analytically.

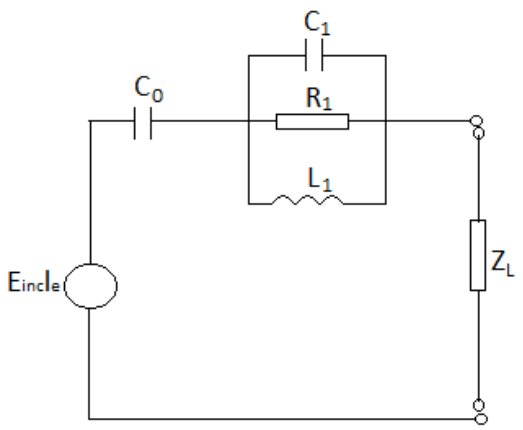

Figure III.1 Equivalent circuit of an electrically small dipole, reproduced from [2]

In the Figure III.1, E_{inc} is the incident electric field, l_e is the dipole effective length, C_0 is the electrostatic capacitance of the dipole, R_1, C_1 and L_1 are the anti-resonance components, Z_L is the load impedance, and the voltage source represents V_{OC}, which is the open-circuit voltage across the antenna terminal. The following process of calculating the dipole input impedance is based on the above equivalent circuit, with some contribution from the University of Nottingham [3]. The parameters are obtained by curve-fitting.

The anti-resonant frequency of the dipole can be calculated as:

$$f_1 = \frac{10^6}{l}\left[8.401\ln\left(\frac{l}{a}\right)+87.67\right] \text{ Hz}$$

$$\omega_1 = 2\pi f_1 \text{ rad/s}$$

The electrostatic capacitance, C_0 is calculated as:

$$C_0 = \frac{27.88 \times 10^{-12}}{\ln\left(\frac{l}{a}\right) - 1.452} \quad \text{F}$$

The impedance of the dipole at resonant is:

$$R_0 = 73\Omega$$

The characteristic impedances of a dipole are:

$$Z_0 = 70.88\left[\ln\frac{l}{a} + 0.7648\right] \quad \text{Hz}$$

$$Z_0 = 125.2\left[\ln\frac{l}{a} + 0.768\right] \quad \text{Hz}$$

Then, the anti-resonant components can be calculated:

$$R_1 = \frac{{Z_0}^2}{R_0}\Omega$$

$$L_1 = \frac{Z_1}{\omega_1} \quad \text{H}$$

$$C_1 = \frac{1}{Z_1\omega_1} \quad \text{F}$$

The dipole effective length, l_e is calculated using

$$l_e = \frac{l\omega_0^2}{s^2 + 2\partial s + \omega_0^2} \quad \text{m}$$

In which ∂ is the damping frequency

$$\partial = \frac{1}{C_0 R_1} \quad \text{rad/s}$$

And the resonant frequency ω_0 is

$$\omega_0 = \sqrt{\partial^2 + {\omega_1}^2} \text{ rad/s}$$

Finally, the input impedance of the dipole is the combination of the impedances of the elements in the equivalent circuit.

$$Z_d = \frac{sL_1R_1}{s^2C_1L_1R_1 + sL_1 + R_1} + \frac{1}{sC_0} \quad \Omega$$

[1] Balanis, C. A. ‘Antenna Theory, Analysis and Design 2nd Edition’. John Wiley & Sons, Inc.,1997. pp620-625.

[2] Tang, T. Tieng, Q. & Gunn, M. Equivalent circuit of a dipole antenna using frequency-dependent lumped elements Antennas and Propagation, IEEE Transactions on, 1993, 41, 100-103

[3] Tong, X. & Thomas, D. W. P . Notes of dipole antenna parameters obtained by curve-fitting, Department of Electrical and Electronic Engineering, the University of Nottingham, 2009.

Appendix IV. MATLAB GA Settings

This appendix describes the MATLAB GA Settings used throughout this research program [1].

The Cost function and search boundary are defined or calculated for each problem given to the GA. The default values of the following parameters of the GA operation are used:

Mutation function: Gaussian function, The Gaussian mutation function adds a random number taken from a Gaussian distribution with mean 0 to each entry of the parent vector. The standard deviation of the Gaussian distribution is determined by the parameters *Scale* and *Shrink*.

Scale is used to determine the initial standard deviation of the Gaussian distribution. If v_{hi} is defined as the upper search bound and v_{lo} is the lower search bound, the initial standard deviation of the Gaussian distribution σ is calculated as:

$$\sigma = scale * (v_{hi} - v_{lo})$$

Shrink is used to control the speed at which the standard diviation decreases as the generations go by. The standard deviation at *k*th generation, σ_k, is given as:

$$\sigma_k = \sigma_{k-1}\left(1 - shrink\frac{1}{generations}\right)$$

The default values for *scale* and *shrink* are 1.

Cross-over fraction: The fraction that the individuals in a generation on which the cross-over operation is performed, it defaults to 0.8.

Cross-over function: The default cross-over function is *Scattered*. In the *Scattered* cross-over function, a random binary string the same length as an individual is generated. Then a new individual is created by selecting genes from the first parent when the binary string is a 1, and from the second parent when the binary string is a 0.

Selection function: The default selection function, *Stochastic Uniform*, lays out a line where each parent corresponds to a section of the line of length proportional to its scaled value. The algorithm moves along the line in steps of equal size. At each step, the algorithm allocates a parent from the section it lands on. The first step is a uniform random number less than the step size.

[1] Gaoptimset options, MATLAB R2010a user manual, Mathworks, 2010

Appendix V. Image theory and approximation of a single source equivalent to the sum of actual and virtual sources

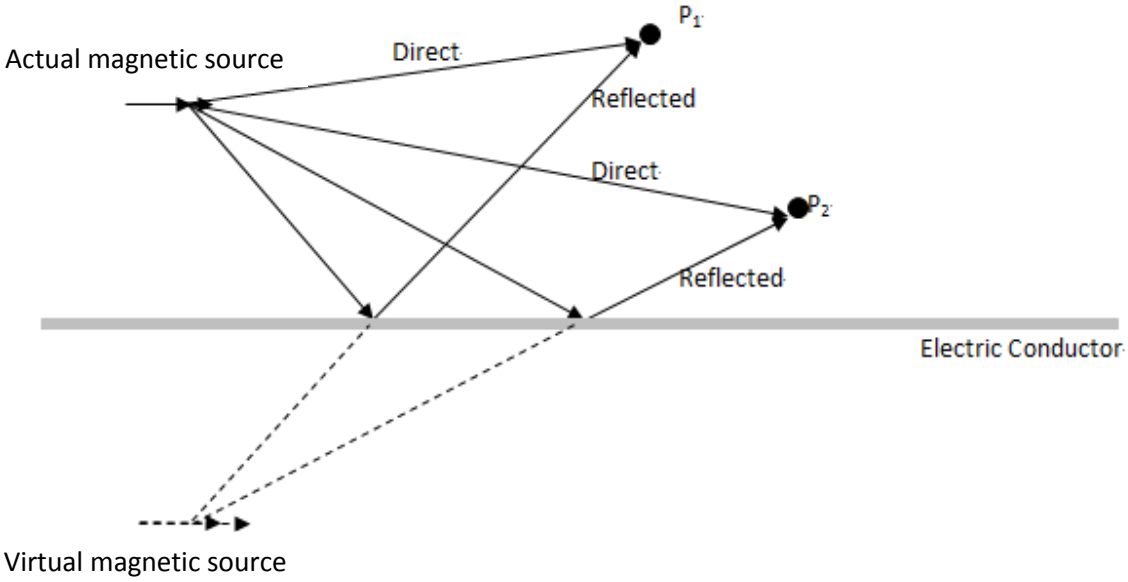

Figure V.1 Image theory, the reflected wave at the observation points can be treated as coming from a virtual source which is an image of the actual source

Figure V.1 illustrates the image theory of a magnetic source placed above a perfect electric conductor sheet, where P_1 and P_2 are the observation points. It can be seen that when a radiating source is placed above a conductor, the observation points receive waves from both the direct path and as reflected by the conductor. The reflected field can be treated as that radiated from a virtual source, which is an image of the actual source on the other side of the conductor. The virtual source has the same intensity as the actual source and is the same distance to the conductor. The radiated field at the observation point can then be calculated as the summation of the field from the actual source and the virtual source without the presence of the conductor. The orientation of the virtual source depends on the nature of the actual source and the conducting plane. The calculation is simplified from that with only the actual source since the calculation of the reflection path can then be avoided.

In our modelling work, a PEC sheet was placed behind the magnetic dipole moment, which creates an image on the other side of the PEC sheet. The field extracted by the observation point thus became summation of the field radiated by the magnetic dipole moment and its image. Our theory is that at low frequencies, providing the distance between the actual and virtual source is small compared to the wavelength,

where the phase difference between them is small. The radiated field can be approximated as that radiated from one single dipole moment radiating in free space, placed in the middle between the actual and virtual sources, but twice the intensity of the actual source. This approximation can be verified by a simple test that compares the radiated field of a dipole moment and that radiated by two dipole moments placed on each side of the original, but with half the intensity.

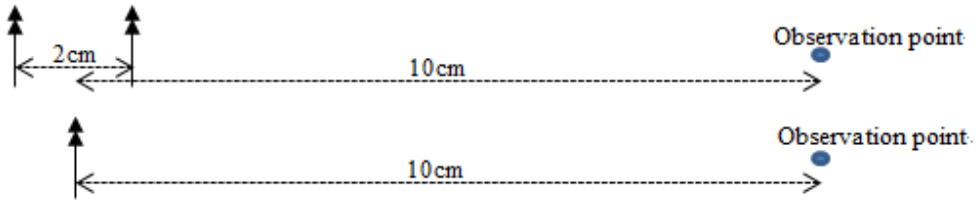

Figure V.2 Positions of dipoles in the Image Theory verification test

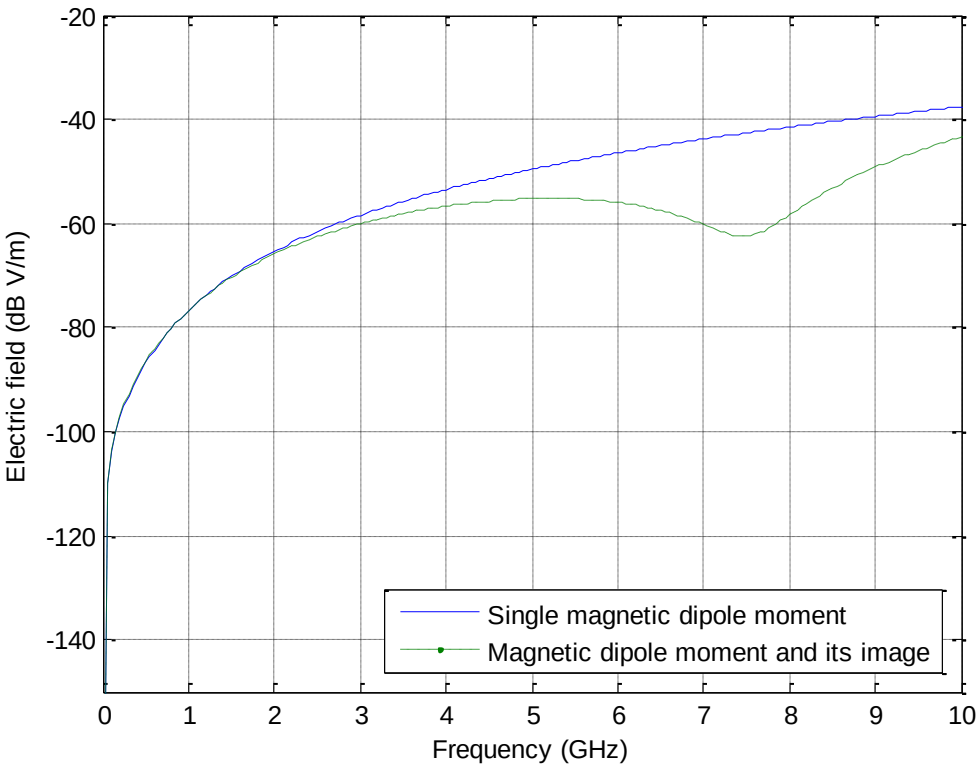

Figure V.3 Frequency domain results of the verification test of Image Theory approximation

It can be seen as the frequency increases, that the phase difference between the two dipoles starts to affect the result from about 2GHz. The separation between them represents an FDTD mesh size of 2cm, which works reliably up to 1.5GHz. Therefore, the approximation that the radiating field from a magnetic dipole moment in front of a PEC sheet is that radiated from one at the location of the PEC sheet radiating in free

space but twice the strength of the original source is valid within the frequency range of the FDTD simulations.

Appendix VI. List of symbols

Symbol	Unit	Meaning
η_0	Ω	Impedance of free space
μ_0	Hm^{-1}	Permeability of free space
ε_0	Fm^{-1}	Permittivity of free space
α_e	Cm^2V^{-1}	Electric polarisability
α_m	m^3	Magnetic polarisability
λ	m	Wavelength
ω	$Rads^{-1}$	Angular frequency
$\boldsymbol{m}$	Am^2	Magnetic dipole moment vector
$\boldsymbol{p}$	Cm	Electric dipole moment vector
$\boldsymbol{E}$	Vm^{-1}	Electric field strength vector
$\boldsymbol{H}$	Am^{-1}	Magnetic field strength vector
p_k		The kth order pole of a digital filter
r_k		The kth order residual of a digital filter
Z_{ab} Z_{ba}	Ω	Transfer impedance
Z^{∞}	Ω	Impedance of high frequency asymptotic response
k	m^{-1}	Wave number

Appendix VII. List of abbreviations

Abbreviation	Meaning
EMC	Electromagnetic compatibility
PEC	Perfect electric conductor
PMC	Perfect magnetic conductor
PML	Perfectly matched layer
FDTD	Finite-difference time-domain
TLM	Transmission line matrix
TE	Transverse electric
TM	Transverse magnetic
AF	Antenna factor
MOM	Method of moment
BCI	Bulk current injection
HIRF	High-intensity radiated field
EMI	Electromagnetic interference
TFSF	Total-field scattered-field

References

[1] Carter, N. *Aircraft EMC, the past, the present and the future: an overview,*EMC (Electromagnetic Compatibility) in Aerospace (Digest No.: 1996/243), IEE Colloquium on, 1996, 3/1 -3/7

[2] Carter, N. & Willis, P. *EMC testing of high-integrity digital systems in aircraft,* EMC in High Integrity Digital Systems, IEE Colloquium on, 1991, 4/1 -4/9

[3] Introduction to Reverberation Chambers Lecture Notes, York EMC Services, Ltd, University of York, 2006.

[4] Melia, G.C.R. Robinson, M.P. Flintoft, I.D. Marvin, A.C. Dawson, J.F. "Broadband Measurement of Absorption Cross Section of the Human Body in a Reverberation Chamber," *Electromagnetic Compatibility, IEEE Transactions on* , vol.55, no.6, pp.1043,1050, Dec. 2013

[5] Powerpoint slides in *the 'Young Scientists Program'*, EMC Europe 2010 distributed CD, Wroclaw

[6] HIRF SE (High Intensity Radiated Field Synthetic Environment) project, EU contract 205294 (FP7), http://www.hirf-se.eu/

[7] Gilbert, J. & Richard Holland. *Implementation of the Thin-Slot Formalism in the Finite-Difference EMP Code THREDII*, IEEE Transactions on Nuclear Science, Vol. NS-28, No. 6, December 1981.

[8] Gkatzianas, M. A. Balanis, A. & R. R. Diaz. *The Gilbert-Holland FDTD Thin Slot Model Revisited: An Alternative Expression for the In-Cell Capacitance*, IEEE Microwave and Wireless Components Letters, Vol. 14, No. 5, May 2004.

[9] Taflove, A. Umashankar, K. Beker, B. Harfoush, F. & Yee, K. *Detailed FD-TD analysis of electromagnetic fields penetrating narrow slots and lapped joints in thick conducting screens*, IEEE Transactions on Antennas and Propagation, 1988, 36, 247-257

[10] Taflove, A. *Review of the formulation and applications of the finite-difference time-domain method for numerical modelling of electromagnetic wave interactions with arbitrary structures*, Wave motion 10 (1998) pp547-582

[11] Riley, D. J. & Turner, C. D. *Hybrid Thin-Slot Algorithm for the Analysis of Narrow Apertures in Finite-Difference Time-Domain Calculations*, IEEE Transactions on Antennas and Propagation, Vol. 38, No. 12, December 1990.

[12] Petre, P. & Sarar, T. *Planar Near-field to far-field transformation using an equivalent magnetic current approach,* Antennas and Propagation, IEEE Transactions on, 1992, 40, 1348-1356

[13] Laurin, J. Zürcher, J.-F. & Gardiol, F. *Near-field diagnostics of small printed antennas using the equivalent magnetic current approach,* Antennas and Propagation, IEEE Transactions on, 2001, 49, 814-828

[14] Tong, X. Thomas, D. W. P. Biwojno, K. Nothofer, A. Sewell, P. & Christopoulos, C. *Modeling electromagnetic emissions from PCBs in free space using equivalent dipoles*, Microwave Conference, 2009. EuMC 2009. European, 2009, 280-283

[15] Tong, X. Thomas, D. W. P. Nothofer, A. Sewell, P. & Christopoulos, C. *A genetic algorithm based method for modeling equivalent emission sources of printed circuits from near-field measurements,* Electromagnetic Compatibility (APEMC), 2010 Asia-Pacific Symposium on, 2010, 293-296

[16] Pozar, D. M. *'Microwave Engineering 2nd Edition'*. John Wiley & Sons, Inc.,1998. pp238

[17] Jackson, J. D. *'Classical Electromagnetics 3rd Edition'*. John Wiley & Sons, Inc., 1999, pp411

[18] Martin, T. Backstrom, M. & Loren, J. *Semi-empirical modeling of apertures for shielding effectiveness simulations,* Electromagnetic Compatibility, IEEE Transactions on, 2003, 45, 229 – 237

[19] Cohn, S. *Determination of Aperture Parameters by Electrolytic-Tank Measurements,* Proceedings of the IRE, 1951, 39, 1416 -1421

[20] McDonald, N. *Simple approximations for the longitudinal magnetic polarizabilities of some small apertures*, Microwave Theory and Techniques, IEEE Transactions on, 1988, 36, 1141 -1144

[21] McDonald, N. *Polynomial Approximations for the Transverse Magnetic Polarizabilities of Some Small Apertures*, Microwave Theory and Techniques, IEEE Transactions on, 1987, 35, 20 – 23

[22] McDonald, N. *Polynomial Approximations for the Electric Polarizabilities of Some Small Apertures*, Microwave Theory and Techniques, IEEE Transactions on, 1985, 33, 1146 – 1149

[23] Yee, K. *Numerical solution of initial boundary value problems involving maxwell's equations in isotropic media*, Antennas and Propagation, IEEE Transactions on, 1966, 14, 302-307

[24] Wikipedia, 'Finite-Difference Time Domain Method', http://en.wikipedia.org/wiki/Finite-difference_time-domain_method, *[accessed: 26/10/2010]*

[25] Dawson, J. F. & Marvin, A. C. Lecture notes of Computational Electromagnetics, Department of Electronics, University of York, Avaliable from 2003.

[26] Furse, C. M. Roper, D. H. Buechler, D. N. Christensen, D. A. & Durney, C.H. *The problem and treatment of DC offsets in FDTD Simulations*. IEEE Transactions on Antennas and Propagation, vol. 48, pp1198-1201, 2000

[27] Wagner, C. L. & Schneider, J. B. *Divergent Fields, Charge and Capacitance in FDTD Simulations.* IEEE Transactions on Microwave Theory and Techniques, vol.46 pp 2131-2136, 1998

[28] Taflove, A. '*Advances in computational electrodynamics, the finite-difference time-domain method*', Artech House, Inc. 1998

[29] Balanis, C .A. *'Advanced Engineering Electromagnetics'*. John Wiley & Sons, Inc. 1989. pp327-335

[30] Nagano, T. Ohno, Y. Uesugi, N. Ikeda, H. Ishiyama, A. & Kasai, N. *Multi-source localization by genetic algorithm using MEG,* Magnetics, IEEE Transactions on, 1998, 34, 2976 -2979

[31] Hussain, B.A. Al-Dabbagh, R.D. *Hybrid canonical genetic algorithm and steepest descent algorithm for optimizing likelihood estimators of ARMA (1, 1) model,*

Applications of Digital Information and Web Technologies, 2008. ICADIWT 2008. First International Conference on the , vol., no., pp.30,37, 4-6 Aug. 2008

[32] Crevecoeur, G. Sergeant, P. Dupré, L. & Van de Walle, R. *A Two-Level Genetic Algorithm for Electromagnetic Optimization,* Magnetics, IEEE Transactions on, 2010, 46, 2585 -2595

[33] Chen, X. Qian, J. Ni, G. Yang, S. & Zhang, M. *An improved genetic algorithm for global optimization of electromagnetic problems,* Magnetics, IEEE Transactions on, 2001, 37, 3579 -3583

[34] Dupré, L. & Slodička, M. *Inverse problem for magnetic sensors based on a Preisach formalism,* Magnetics, IEEE Transactions on, 2004, 40, 1120 - 1123

[35] Li, F. Morgan, R. Williams, D. & Song, Y. *Handling constrained power dispatch with genetic algorithms,* Genetic Algorithms in Engineering Systems: Innovations and Applications, 1995. GALESIA. First International Conference on (Conf. Publ. No. 414), 1995, 181 -187

[36] Bethe, H. A. *Theory of Diffraction by Small Holes* phys. Rev., American Physical Society, 1944, 66, 163-182

[37] Pekeris, C. L. *Comments on Bethe's Theory of Diffraction of Electromagnetic Waves by Small Holes,* Phys. Rev., American Physical Society, 1944, 66, 351-351

[38] Fante, R. & Mayhan, J. *Complete electric field of the infinite slot antenna,* Antennas and Propagation, IEEE Transactions on, 1969, 17, 97 – 98

[39] Miller, D. A. B. *Huygens's wave principle corrected,* Optics Letters (ISSN 0146-9592), vol. 16, Sept. 15, 1991, p. 1370-1372.

[40] Rao, S. Wilton, D. & Glisson, A. *Electromagnetic scattering by surfaces of arbitrary shape,* Antennas and Propagation, IEEE Transactions on, 1982, 30, 409 – 418

[41] MATLAB, 'Genetic algorithm options'. http://www.mathworks.co.uk/help/gads/genetic-algorithm-options.html *[accessed: 24/09/2013]*

[42] Balanis, C. A. *'Antenna Theory, Analysis and Design 2nd Edition'*. John Wiley & Sons, Inc.,1997. pp135.

[43] Marvin, A. Dawson, L. Flintoft, I. & Dawson, J. *A Method for the Measurement of Shielding Effectiveness of Planar Samples Requiring No Sample Edge Preparation or Contact*, Electromagnetic Compatibility, IEEE Transactions on, 2009, 51, 255 -262

[44] Flintoft, I. D. *Technical notes of Vulture*, Department of Electronics, University of York, 2013.

[45] Martin, T. & Backstrom, M. *Semi-empirical modeling of apertures by use of FDTD*, Electromagnetic Compatibility, 1999 IEEE International Symposium on, 1999, 2, 832-837 vol.2

[46] Taflove, A & Hagness, S.C. *'Computation electrodynamics, the finite-difference time-domain method, second edition'*, Artech House, Boston. London, 2000. Pp 194-197

[47] Junqua, I. Parmantier, J-P. & Bertuol, S. *Fundamentals of the PWB Approach*, Technical notes for HIRF-SE WP3, ONERA, September 2010.

[48] Xia, R. Dawson, J. F. Flintoft, I. D. Marvin, A. C. Porter, S. J. & Marschke, I. *Building Electromagnetic Macro Models for Small Structures on Aircraft*, EMC Europe 2011

[49] Tang, T. Tieng, Q. & Gunn, M. *Equivalent circuit of a dipole antenna using frequency-independent lumped elements Antennas and Propagation*, IEEE Transactions on, 1993, 41, 100-103

[50] ADL5562 Data Sheet, Analogue Devices, 2010